

Syracuse University

SURFACE at Syracuse University

Dissertations - ALL

SURFACE at Syracuse University

5-14-2023

CsPbX₃ Nanoparticle Synthesis Via Nonpolar Solvent Choice and Microwave Heating, Growth Mechanism and CsPb(Br/I)₃ Stabilization by Halide Exchange

Hediyeh Zamani
Syracuse University

Follow this and additional works at: <https://surface.syr.edu/etd>

Recommended Citation

Zamani, Hediyeh, "CsPbX₃ Nanoparticle Synthesis Via Nonpolar Solvent Choice and Microwave Heating, Growth Mechanism and CsPb(Br/I)₃ Stabilization by Halide Exchange" (2023). *Dissertations - ALL*. 1702.
<https://surface.syr.edu/etd/1702>

This Dissertation is brought to you for free and open access by the SURFACE at Syracuse University at SURFACE at Syracuse University. It has been accepted for inclusion in Dissertations - ALL by an authorized administrator of SURFACE at Syracuse University. For more information, please contact surface@syr.edu.

Abstract

Perovskites are a group of crystalline chemicals with ABX_3 formula where cations are surrounded by corner-sharing octahedra. Their crystal structure was described by Victor Goldschmidt in 1926, almost a century after the first discovery of the mineral perovskite, $CaTiO_3$, by Gustav Rose in 1839. Organic-inorganic (hybrid) lead halide perovskites became a point of interest when their potential as a visible-light adsorber in solar cells was demonstrated by Kojima et. al. in 2009. All-inorganic perovskites gain traction after their synthesis as colloidal quantum dots in 2014. While there have been numerous studies on the application of perovskite nanoparticles (NP) in optoelectronic devices, lasers and sensors, there is a lot of chemistry to explore to reach their full potential. The focus of this dissertation is on all-inorganic $CsPbX_3$ nanoparticles. In chapter two, a novel microwave assisted method is described to synthesize 2-dimensional (2D) $CsPbX_3$ NPs in benzyl ether. We demonstrated that microwave irradiation provides a feasible and reproducible path to tailor the morphology of these NPs. Then, the NP's structural features and subsequent optoelectronic properties are explained. To fully understand the effect of the structure and composition on the band gap of these NPs, a comprehensive description of the intrinsic optoelectronic properties of $CsPbX_3$ NPs is reported in chapter one. To elucidate their synthesis path further, we compared them with NPs prepared with a established synthesis technique, hot-injection method in 1-octadecene, in chapter three. This comparison shed light on the preference of the NPs to grow in 2D directions in benzyl ether under microwave irradiation. This study was expanded, by monitoring the growth of $CsPbBr_3$ NPs over time at ambient condition as well, which confirmed the role of benzyl ether in the morphology. Other perovskite synthetic methods are also reviewed in chapter one, along with the various mechanisms of orientational growth in $CsPbX_3$ NPs. In addition, we explored the effect of

benzyl ether on ionic interactions in the lead halide precursor, in particular, the formation of halo plumbate complexes and their contribution in the 2D growth of the perovskite colloidal seeds were evaluated. In chapter four, the goal was to use a halide exchange technique to stabilize CsPbI₃ NPs in colloidal form and in thin film format. In this chapter, the electronic band gap of the CsPbBr₃ and I-rich CsPbX₃ NPs was measured using cyclic voltammetry. We calculated the energy gap between HOMO and LUMO of the NPs and explain the contribution of atomic orbitals, as well.

During this dissertation research, we sought to learn the chemistry of all-inorganic perovskites and became fascinated with their adaptability to the synthesis environment and their dynamic response to the post-synthesis challenges. This ability provides tremendous opportunity for researchers to tailor perovskite NPs for applications that require a semiconductor with any desired band gap that can be formed into nano-, micro- or macro-scale with flexibility.

Title:

**CsPbX₃ Nanoparticle Synthesis Via Nonpolar Solvent
Choice and Microwave Heating, Growth Mechanism and
CsPb(Br/I)₃ Stabilization by Halide Exchange**

By

Hediyeh Zamani

M.Phil., Syracuse University, 2020

B.S., Sharif University of Technology, 2013

Dissertation

Submitted in partial fulfillment of the requirements for the degree of
Doctor of Philosophy in Chemistry

Syracuse University

May 2023

Copyright © Hediye Zamani 2023

All Rights Reserved

Acknowledgment:

First and foremost, I am extremely grateful to my supervisor, Prof. Mathew M. Maye for his invaluable advice and continuous support during brainstorm meetings, research and experiments. With extensive knowledge and patience, he guided me in every step of the way and I'm thankful for that. I wish to express my deepest gratitude to the dissertation committee for insightful feedbacks on this dissertation. I would like to recognize the invaluable assistance that you provided during my PhD journey.

I also want to thank former and current members of the Maye lab, for their help during data collection, group meetings and many formal and informal discussions. So many thanks to Kaylie for all her hard work and camaraderie through this research. Special thanks to my friend and accomplice, Buddhini, your calls during the dissertation writing kept me connected and motivated. I'll always cherish the memory of us having coffee with a view of Syracuse sunset from the lab window. I must also thank Andrew for his friendship and all the collaborations.

Getting through my PhD required more than academic support, and I have many people to thank for their personal and professional support. I'd like to express my gratitude and appreciation for my friends, Sommy, Sam, Farnaz, Saleh, Tina and Ala for being my family far from home and for many memorable evenings during this time. I would also like to thank all of my non-Iranian friends specially Linda who opened both her home and heart to us during the holidays.

To my family and specially, my sisters, it would be an understatement to say that we have experienced some ups and downs in the past few years that I've been far from you. You were in my thoughts every day and I'm thoroughly grateful for all the encouragement through phone calls and WhatsApp messages. I hope I made you proud. I hope maman, agha and baba are proud of me too. And I wish for a free Iran, for Woman, Life, Freedom.

To Meraj, words are not enough in expressing my love and appreciation for you, my amaaazing, supportive and smart partner. It has been wonderful to have you by my side in the past thirteen years and knowing that you will always have my back. It is no coincident that the next to last figure of this dissertation was developed with your magic Python skills. Thank you for all the love and care, for lighting up my path and for figure 4.13!

Table of Contents

List of Figures	viii
List of Abbreviations	xv
Chapter 1 – Introduction.	1
1.1 Advancement of Perovskite Nanoparticles and Nanotechnology.	1
1.2 Chemistry of 2-dimentional (2D) Perovskite Nanoparticles	2
1.2.1 Composition Tunability.	4
1.2.2 Tunning the Band Gap by Nanoparticle’s Composition	5
1.2.3 Tunning the Band Gap by Nanoparticle’s Dimension	6
1.2.4 Photoluminescence Tunability.	9
1.2.5 Quantum Efficiency	10
1.3 Synthesis of 2D CsPbX ₃ Perovskite nanoplatelets	11
1.3.1 Orientational Growth in Perovskite 2D Nanoparticles	13
1.3.2 Solvent Effect on the Morphology of All-inorganic Perovskite Nanoparticles. ...	17
1.3.3 2-D Perovskite Synthesis Methods	19
1.3.2.1 Ligand-assisted Precipitation.	19
1.3.2.2 Hot Injection	20
1.3.2.3 Solvothermal Synthesis	22
1.3.2.4 Microwave-assisted Synthesis.	23
1.3.2.5 Heating Mechanisms in Microwave-assisted Synthesis	24
1.4 Halide Exchange of CsPbX ₃ via Post-Synthesis Reactions	26
1.4.1 Halide Exchange of CsPbX ₃ Deposited on a Substrate.	28
1.5 Applications	30
1.6 Research Summary.	31
Chapter 2 – Microwave-Assisted Synthesis of 2D CsPbBr₃ Nanoplatelets.	33
2.1 Introduction.	34
2.2 Experimental.	36
2.2.1 Materials	36

2.2.2 Methods	36
2.2.2.1 Precursor Preparation.	36
2.2.2.2 One-Pot MWI Heating and Synthesis of CsPbX ₃	36
2.2.2.3 Hot Injection and Conventional Heating Based Synthesis of CsPbX ₃	37
2.2.2.4 BE-CsPbI ₃ synthesis via Halide Exchange of BE-CsPbBr ₃	37
2.2.2.5 Benesi-Hildebrand Analysis	38
2.2.3 Instrumentation	38
2.3 Results and Discussion.	41
2.4 Conclusion	58
Chapter 3 – Mechanism of formation in 2D CsPbBr₃ perovskite nanoparticles	59
3.1 Introduction.	60
3.2 Experimental.	63
3.2.1 Materials	63
3.2.2 Methods	63
3.2.2.1 Synthesis of CsPbBr ₃ Perovskite Nanoplatelets.	63
3.2.2.2 Benzyl Ether Coordination - Benesi-Hildebrand Analysis	64
3.2.3 Instrumentation	64
3.3 Results and Discussion.	66
3.4 Conclusion	87
Chapter 4 – 2D CsPbI₃ Nanoparticles Synthesis via Halide Exchange Reaction of CsPbBr₃ Nanoplatelets and PbI₂	88
4.1 Introduction.	89
4.2 Experimental.	91
4.2.1 Materials	91
4.2.2 Methods.	91
4.2.2.1 Synthesis of CsPbBr ₃ Perovskite Nanoplatelets	91
4.2.2.2 Halide Exchange of CsPbBr ₃ Nanoplatelets with PbI ₂	92
4.2.2.3 In-situ Halide Exchange of CsPbBr ₃ Nanoplatelets with PbI ₂	92
4.2.2.4 Preparation of CsPbBr ₃ Film on Borosilicate Glass Slides	92

4.2.2.5 Halide Exchange on CsPbBr ₃ Film	93
4.2.3 Instrumentation	93
4.3 Results and Discussion.	96
4.4 Conclusion	120
Chapter 5 – Conclusion and Outlook	121
Chapter 6 – References.	125
Chapter 7 – Curriculum Vitae.	139

List of Figures

Figure 1.1. Cubic (a) and Orthorhombic (b) crystal structure of CsPbX_3 perovskite, unit cells are outlined by black lines	3
Figure 1.2. Schematic diagram of bonding/antibonding orbitals (a) forming VBM and CBM in CsPbX_3 NPs and band gap energy of CsPbX_3 NPs (b) measured using cyclic voltammetry.	6
Figure 1.3. Schematic wavefunctions and energy levels of electron in a one-dimensional box for first two energy levels.	8
Figure 1.4. Schematic illustration of PL emission and band gap dependency on size and composition of perovskite nanoparticles	9
Figure 1.5. Schematic Jablonski diagram showing radiative and non-radiative recombination of excitons for CsPbBr_3 perovskite.	11
Figure 1.6. Schematic representation of anisotropic growth from perovskite seeds to 0D, 1D, and 2D nanoparticles.	14
Figure 1.7. PL emission (a), schematic illustration and SEM micrographs (b) showing transition of CsPbBr_3 nanoparticles into bulk films by Ostwald ripening over 60 min at 125 °C	16
Figure 1.8. Schematic illustration (a), PL emission (b) and TEM micrographs (c) showing CsPbX_3 nanosheets prepared by self-assembly of first nanorods and second nanoplatelets under solvothermal conditions at 160 °C over 5 h	17
Figure 1.9. Schematic representation of 2D CsPbX_3 syntheses. Microwave-assisted (a), Hot-injection (b), Ligand-assisted precipitation (c), and Solvothermal (d) techniques.	22
Figure 1.10. Schematic illustration of conventional and microwave heating mechanisms.	25

Figure 1.11. Schematic representation of a perovskite cubic crystal structure and its halide exchange (a). Normalized PL emission (b) of CsPbX ₃ nanoparticles formed via halide exchange between CsPbBr ₃ nanoparticles and either CsPbCl ₃ or CsPbI ₃	27
Figure 1.12. Spectral (a) and visual (b,c) PL emission over the course of the halide exchange reaction between CsPbI ₃ and 2-bromododecanoic acid under UV light. Images of the Finkelstein reaction next to CsPbI ₃ (left) as control (b). Visual PL emission (c) of the reaction controlled by the 2-bromododecanoic acid concentration and time.	28
Figure 1.13. Schematic representation (a) of halide exchange in a CsPbBr ₃ film. Gradient halide exchange (b) in thin (50 nm) vs thick (350 nm) films	30
 Figure 2.1. (a) Schematic overview of the reaction systems used in this study. UV-vis (a) and PL emission (b) spectra of the BE- (i), and ODE-CsPbBr ₃ products prepared via MWI heating to 160 °C.	41
Figure 2.2. Representative TEM micrographs of ODE-CsPbBr ₃ (a) and BE-CsPbBr ₃ products (b-e) Size analysis histogram of BE-CsPbBr ₃ showing platelet 2D dimensions (f)	42
Figure 2.3. Representative tapping mode AFM image (a) and corresponding cross-section analysis (b-c) of two regions (arrows) of BE-CsPbBr ₃ nanoplatelet domains drop cast onto HOPG.	43
Figure 2.4. Representative powder XRD of BE-CsPbBr ₃ (i) and ODE-CsPbBr ₃ products (ii), as compared to an orthorhombic CsPbBr ₃ standard (97851-ICSD)	44
Figure 2.5. Representative SEM micrographs of purified BE-CsPbBr ₃ dropcast onto HOPG and imaged at increasing magnifications (a-c).	46

Figure 2.6. Control experiment XRD results comparing the purified BE-CsPbBr ₃ nanoplatelets prepared (top) and same nanoplatelets with 50 µL of 3 g/L carbon black added and sonicated before drop casting (bottom), testing whether or not the nanoplatelets stacked on the XRD holder, which was found to not be the case, due the similarity of the two results. Orthorhombic reference planes shown for illustration only.	47
Figure 2.7. PL emission results of BE-CsPbBr _{3-x} I _x formed via the one-pot MWI heating (160 °C) synthesis using increasing concentrations of [PbI _n] ²⁻ⁿ (i-v) complexed with BE and OAm. . . .	48
Figure 2.8. XRD results of BE-CsPbBr _{3-x} I _x formed via the one-pot MWI heating (160 °C) synthesis using increasing concentrations of [PbI _n] ²⁻ⁿ (i-v) complexed with BE and OAm. . . .	49
Figure 2.9. PL emission (a) and XRD (b) of BE-CsPbBr ₃ nanoplatelets before (i), and after halide exchange with two consecutive washing steps with OAm-PbI ₂ (ii-iii) following our recent work.	50
Figure 2.10. (a-d) Representative TEM micrographs of BE-CsPbBr ₃ products via hot-injection in BE. Samples collected from soluble (a, l = 6.8 ± 1.1 nm) and non-soluble fractions (b-c, l = 11.1 ± 3.5 nm) of the synthesis solution after centrifugation. Early reaction times show a high concentration of small clusters (arrow, d ~ 3.5 nm). The sole non-soluble product after 30 min annealing (d, l1 = 17.4 ± 2.6 nm, l2 = 10.4 ± 1.6 nm).	51
Figure 2.11. Representative powder XRD of BE-CsPbBr ₃ hot-injection products for soluble (i), and insoluble (ii) fractions and ODE-CsPbBr ₃ (iii) after ~1 min annealing. Reference patterns for cubic (1533063-COD, red) and orthorhombic CsPbBr ₃ (97851-ICSD, blue).	52
Figure 2.12. The UV-vis of [PbBr _n] ²⁻ⁿ formed via PbBr ₂ dissolved in BE (i), BE+OAc+OAm (ii), ODE+OAc+Oam (iii), and ODE (iv) at 140 °C under vacuum for 1h and then cooled to room	

temperature. Approximate absorption regions for different $[\text{PbBr}_n]^{2-n}$ complexes are shown. Spectral ranges used vary due to solvent absorption. 53

Figure 2.13. FTIR of purified BE- CsPbBr_3 product (a), BE, (b), OAc (c), and OAm (d), and highlighted regions of interest, C-H benzyl rings (i), aliphatic C-H (ii), C=O (iii), and C=C (iv). 55

Figure 2.14. XRD results of the BE- CsPbBr_3 nanoplatelet products produced at $[\text{OAc}]:[\text{Cs}^+] = 5$, demonstrating that platelet formation was still observed with more soluble precursors. 56

Figure 2.15. An idealized mechanism schematic for the growth of CsPbBr_3 using BE or ODE solvents. 56

Figure 3.1. Photoluminescence (PL) emission spectrum and structural characterization of CsPbBr_3 NPs prepared in ODE via MWI heating at 160 °C. ODE- CsPbBr_3 absorbance (i) and PL emission (ii) spectra (a), XRD pattern (b) of the ODE- CsPbBr_3 NPs and the orthorhombic perovskite reference (97851-ICSD), TEM micrograph and the corresponding histogram (c), and AFM image and height profile of the ODE- CsPbBr_3 NPs (d) 66

Figure 3.2. Representative UV-Vis and PL spectra of the CsPbBr_3 solution pre-treatment at room temperature collected over one month. Absorption and PL spectra in BE (a, c) and ODE (b, d). 68

Figure 3.3. Representative TEM micrographs of ODE- (a) and BE- CsPbBr_3 (b) products formed at room temperature after 24 h reaction. Inserts: Enlarged areas within micrographs. 70

Figure 3.4. XRD of ODE-CsPbBr ₃ (i) and BE-CsPbBr ₃ (ii) products formed at room temperature over 1.5 months, a cubic CsPbBr ₃ reference (1530681-COD) and an orthorhombic CsPbBr ₃ reference (97851-ICSD) are shown for comparison.	71
Figure 3.5. UV-Vis absorption (i) and PL emission (ii) spectra (a) of CsPbI ₃ synthesized at room temperature in BE. XRD results (b) characterizing the crystal structure of CsPbI ₃ nanostructures prepared in BE at room temperature after 24 h with matching standard orthorhombic XRD pattern (4127358-COD)	71
Figure 3.6. Benesi-Hildebrand analysis, UV-Vis absorption (a) of iodoplumbate complexes and absorption at 490 nm (b) as a function of [MAI]:[PbI ₂] ratios in a reaction mixture of PbI ₂ -BE precursor and MAI-BE in toluene.	73
Figure 3.7. Benesi-Hildebrand analysis of iodoplumbate complexes in 0.2 mM PbI ₂ with increasing [MAI] in DMF. In (a) absorption of PbI ₂ was monitored with increasing [MAI], (b) shows absorbance at 420 nm vs [MAI]:[PbI ₂] ratio, (c) shows Benesi-Hildebrand plot based on the absorption profile at 420 nm.	74
Figure 3.8. Benesi-Hildebrand analysis of iodoplumbate complexes in 0.2 mM PbI ₂ with increasing [MAI] in a 50:50 (v/v) BE:DMF solvent mixture. In (a) and (d) absorption of PbI ₂ was monitored with increasing [MAI]. (b) and (e) show absorbance at 550 nm versus [MAI]:[PbI ₂] ratio. (c) and (f) show Benesi-Hildebrand plot based on the absorption profile at 550nm. For (d), (e) and (f) OAc was added to PbI ₂ mixture prior to Benesi-Hildebrand analysis.	76
Figure 3.9. Benesi-Hildebrand analysis of iodoplumbate complexes in 0.2 mM PbI ₂ with increasing [MAI] in BE shown in (a), (b), and (c) and a 50:50 (v/v) BE:ODE solvent mixture shown in (d), (e), and (f). In (a) and (d) absorption of PbI ₂ was monitored with increasing [MAI],	

(b) and (e) shows absorbance at 490 nm versus [MAI]:[PbI₂] ratio, (c) and (f) shows Benesi-Hildebrand plot based on the absorption profile at 490 nm 78

Figure 3.10. Schematic illustration of CsPbBr₃ nanoplatelets synthesis via MWI at 160 °C. First, a Cs-oleate and a PbBr₂-OAm precursor are prepared, then a mixture of them is heated in a microwave synthesizer. A temperature profile of the reaction mixture in BE and ODE is shown. An image of the final BE-CsPbBr₃ products under both ambient and UV light is displayed with inset showing a schematic representation of a nanoplatelet with an orthorhombic unit cell (unit cell is drawn by Mercury software from a standard perovskite orthorhombic, 97851-ICSD). . . 79

Figure 3.11. Representative photoluminescence emission (i) and absorption (ii) spectra (a) and XRD (b) of BE-CsPbBr₃ nanoparticles prepared via hot-injection synthesis at 160 °C. 80

Figure 3.12. Schematic representation of the MWI based synthesis of ODE-CsPbBr₃ nanocubes and BE-CsPbBr₃ nanoplatelets 81

Figure 3.13. Representative UV-Vis absorption (a), PL emission (b) and XRD (c) of the CsPbBr₃ nanoplatelets post-treatment with Cs⁺, PbBr₂ and a mixture of both at room temperature. 83

Figure 3.14. PL emission (a, c) and XRD (b, d) spectra of the CsPbBr₃ nanoplatelets post-treatment with Cs⁺, PbBr₂ and a mixture of both at room temperature (a, b) and 50 °C (c, d). NPs and precursors were combined with a 1:1 ratio of moles of that precursor in the NP solution . . 85

Figure 4.1. UV-Vis absorption (a) and photoluminescence emission (b) of CsPbX₃ during the halide exchange reaction of CsPbBr₃ and PbI₂. Pictures (c) taken during the halide exchange reaction under a UV lamp. XRD pattern (d) of CsPbBr₃ (blue), the post-reaction I-rich CsPbX₃ (red), and an orthorhombic CsPbBr₃ reference (black) 97851- ICSD 97

Figure 4.2. PL emission of 2D BE-CsPbX ₃ (a) and 0D ODE-CsPbBr ₃ (b) during the halide exchange reaction of CsPbBr ₃ and PbI ₂ . PbI ₂ was added in three steps of 50 μL	99
Figure 4.3. PL emission of 2D BE-CsPbX ₃ (a) and 1D ODE-CsPbBr ₃ (b) during the halide exchange reaction of CsPbBr ₃ and PbI ₂ . (c) shows the trend of maximum emission wavelength over the course of the reaction. PL was recorded after addition of 10 μL PbI ₂ until the emission was stable	100
Figure 4.4. UV-Vis absorption and PL emission spectra of 2D BE-CsPbX ₃ (a-b) and 1D ODE-CsPbBr ₃ (d-e) during the halide exchange reaction of CsPbBr ₃ nanoplatelets and PbI ₂ . (c) shows the trend of maximum emission wavelength versus PbI ₂ concentration over the course of the reaction and (f) shows the difference of emission wavelength between CsPbX ₃ at each step and the initial CsPbBr ₃ . 10 μL PbI ₂ was added every minute for 12 minutes and absorption and PL were recorded after each addition.	102
Figure 4.5. Calibration curve (a) and TGA (b) of CsPbBr ₃ nanoplatelets.	104
Figure 4.6. PL emission spectra of 2D BE-CsPbX ₃ (a) during the halide exchange reaction of CsPbBr ₃ nanoplatelets and PbI ₂ . (c) shows the trend of maximum emission wavelength versus [I ⁻]:[Br ⁻] ratio over the course of the reaction	105
Figure 4.7. PL emission spectra of CsPbBr ₃ nanoplatelets diluted in toluene by a factor of 5, 10 and 25 (a). Trend of PL intensity at maximum quenching over time (b) for 5x, 10x and 25x diluted CsPbBr ₃ nanoplatelets vs the 10x solution modified by PbBr ₂ and a 50:50 (v/v) PbBr ₂ :PbI ₂	106
Figure 4.8. PL emission (a) and XRD pattern (b) of 2D BE-CsPbX ₃ during the halide exchange reaction of CsPbBr ₃ and PbI ₂ . The CsPbX ₃ NPs were purified and reacted with an [I ⁻]:[Br ⁻] ratio of 1:1 four times and PL was measured in 2 and 30 minutes after each addition	108

Figure 4.9. Schematic overview of CsPbBr ₃ film preparation and halide exchange created with BioRender.com.	110
Figure 4.10. Schematic illustration of MAPbBr ₃ QDs@SiO ₂ core/shell LARP synthesis using (3-aminopropyl)trimethoxy silane (APTMS) and 3-aminopropyl(diethoxy)methyl silane (APDEMS)	112
Figure 4.11. PL spectra (a) and optical images (b) during the halide exchange reaction between CsPbBr ₃ film and PbI ₂ . PL emission from the middle section of the films is reported. PL emission and images of the film 4 days and 7 days after the halide exchange are marked	114
Figure 4.12. PL emission (a) and UV-Vis absorption (b) spectra and optical images (b) during the halide exchange reaction between CsPbBr ₃ film and PbI ₂ . PL emission and images of the film 4 days after the halide exchange are marked	114
Figure 4.13. Cyclic voltammogram (a) and UV-Vis absorption spectrum (b) of CsPbBr ₃ nanoplatelets. Cyclic voltammetry was recorded using a 0.1 M Bu ₄ NBF ₄ (in DCM) with the scan rate of 0.1 V/s	116
Figure 4.14. Cyclic voltammogram of CsPb(Br/I) ₃ nanoplatelets in a 0.1 M Bu ₄ NBF ₄ (in DCM) with the scan rate of 0.1 V/s over six cycles	118
Figure 4.15. UV-Vis absorption (a) and PL emission (b) spectra during the halide exchange reaction of CsPbX ₃ and HAuCl ₄	119
 Figure 5.1. Photoluminescence spectra of CsPbBr ₃ solution pre-treatment at room temperature in (a) tetraglyme (TG) and (b) toluene (Tl) collected on the first and fourth day of the preparation	123

List of abbreviations

2D	Two Dimensional
AFM	Atomic Force Microscopy
BE	Benzyl Ether
BH	Benesi-Hildebrand
CBM	Conduction Band Minimum
CE	Counter Electrode
CV	Cyclic Voltammetry
DCM	Dichloromethane
DMF	N,N-dimethylformamide
DN	Donor Number
FTIR	Fourier Transform Infrared Spectroscopy
FWHM	Full Width at Half Maximum
HOMO	Highest Occupied Molecular Orbital
ICSD	Inorganic Crystal Structure Database
LARP	Ligand-Assisted Reprecipitation
LCD	Liquid Crystal Displays
LED	Light Emitting Diode
LUMO	Lowest Unoccupied Molecular Orbital
MAI	Methyl Ammonium Iodide
MWI	Microwave Irradiation
NMR	Nuclear Magnetic Resonance
NP	Nanoparticle
OAc	Oleic Acid
OAm	Oleyl Amine
ODE	1-Octadecene
PL	Photoluminescence

QD	Quantum Dot
QY	Quantum Yield
TEM	Transmission Electron Microscopy
TGA	Thermogravimetric Analysis
TOPO	Trioctyl Phosphine Oxide
UV-Vis	UV-Visible
VBM	Valence Band Maximum
WE	Working Electrode
XRD	X-Ray Diffraction

Chapter 1 – Introduction

1.1 Advancement of Perovskite Nanoparticles and Nanotechnology

From the first computers that occupied a whole room for calculating mathematics questions to smart watches with multitask capabilities, one main ambition that drove the scientists and engineers was to produce smaller semiconductors with enhanced capacities. In 1970, the smallest of the semiconductors, nanocrystals of cadmium selenide in a molten glass matrix, were synthesized by Alexei Ekimov.¹ In 1982, Louis Brus produced the first colloidal nanocrystals, cadmium sulfide, in AT&T Bell Laboratories.² These nanocrystals were later coined as “Quantum Dots” (QD) in 1988 in making the first QD device by Mark Reed who received his Ph.D. from Syracuse University in 1983. Reed et. al. showed spatial quantization using GaAs-AlGaAs QDs and its photoluminescence (PL) emission spectra.³ This same desire sent researchers to a new quest when in 2004 Andre Geim and Konstantin Novoselov discovered 2D graphene, a single layer of carbon atoms in a honeycomb structure.⁴ Thereafter, scientists were able to explore and study the 2D structure in other materials such as, boron nitride, molybdenum disulfide, carbon nanotubes and perovskites.⁵

Producing nanoscale semiconductors did not only bring the technology closer to the nanoscale electronic and optoelectronic devices, but also had other advantages to traditional silicon semiconductors, including wide spectral absorption and tunability of PL emission. Controlling the energy that QDs could emit within a few eV units opened new avenues of applications in the optoelectronic field. For example, Protesescu et. al. showed CsPbBr₃ nanocrystals can produce a wide range of pure colors surpassing the conventional LCD TVs.⁶ Recently, Naresh et. al.

fabricated red-green-blue (RGB) emitting CsPbX_3 nanocrystals for light emitting diodes (LED) with superior performance due to their narrow emission, high stability and color tunability.⁷

Among all structures, 2D nanocrystals have been of a particular interest to the scientists and manufacturers because of its compatibility to the semiconductor industry. To tune the optoelectronic properties of the perovskite nanoparticles, at least one of the dimensions has to be in the quantum confinement regime. Fabricating QDs with such small dimension is at best challenging, hence, the answer is in 2D nanoplatelets with one confined dimension. Producing a single crystal with large lateral dimensions but nanometer thickness can transform the modern technology. The advantage of 2D nano-perovskites is outperforming the common semiconductor films in optoelectronic devices with photoluminescence tunability of perovskite nanoparticle colloids. Several studies have shown the potential of 2D perovskite nanostructures in printable semiconductors, flexible memory devices, LEDs and solar cells.^{8–13}

1.2 Chemistry of 2-D Perovskite Nanoparticles

CsPbX_3 nanoparticles belong to a large class of compounds called perovskite with an ABX_3 crystal structure. CsPbX_3 nanomaterial can crystalize in cubic, orthorhombic and tetragonal structures where Cs cations are occupying the 12-coordinate cavity between corner-sharing PbX_6 octahedra complexes, as shown in figure 1.1. CsPbX_3 perovskites with the band gap range of 2.82-1.73 eV fall in the semiconductor category.¹⁴

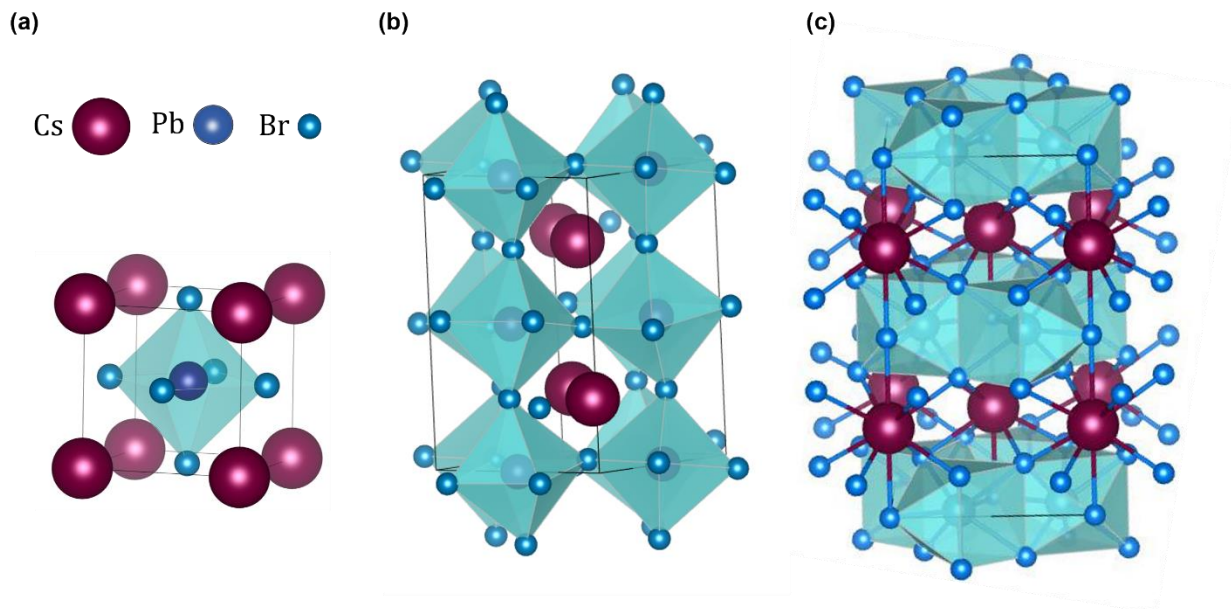


Figure 2.1. Cubic (a), orthorhombic (b), and tetragonal (c) crystal structure of CsPbX₃ perovskite, unit cells are outlined by black lines.¹⁵

In this section a summary of optoelectronic properties of CsPbX₃ perovskite nanoparticles will be described. The advantage of these nanoparticles to their bulk counterparts is the ability to modulate the physical properties of the materials such as band gap (E_g) by controlling dimensional parameters. Band gap for CsPbX₃ semiconductors is defined as the minimum energy to excite an electron and form the exciton. Bombarding a bulk semiconductor with a photon, results in the formation of a free electron-hole pair, i.e., exciton, that can move in the structure until it emits its energy by radiative recombination of the electron and hole or loses its energy by nonradiative recombination when it falls into “traps”.¹⁶ However, an exciton in a CsPbX₃ semiconductor nanoparticle is bound to the nanoparticle’s dimensions. As a result of this quantum confinement, exciton formation requires higher energy and band gap increases.¹⁷ Therefore, for nanoparticles, minor changes in size and morphology affects the band gap and other optoelectronic properties.¹⁸ This effect will be discussed in detail in section 1.2.2-5.

1.2.1 Composition Tunability

Composition tunability originates in the flexible ionic structure and octahedra tilting of perovskites.¹⁹ In fact, various transition metals can form oxide compounds with perovskite structure. As a general rule, any perovskite composition that satisfies the Goldschmidt tolerance factor (t) condition, $0.89 < t < 1$, can exist in an ideal cubic structure and deviation from the tolerance factor by larger ions results in tilting of the octahedra and crystallization in other forms, such as, orthorhombic or tetragonal structure.²⁰ Goldschmidt tolerance factor is calculated using the equation 1 and the effective ionic radii of the constituent ions.

$$t = \frac{(r_A + r_X)}{\sqrt{2}(r_B + r_X)} \quad \text{Equation 1}$$

where r_A , r_B and r_X denote effective ionic radii for A, B cations and X anion of ABX_3 perovskite, respectively. Such structural dynamics allows room for controlling composition, doping of the crystal and exchanging ions with other materials for sensing or catalysis applications. It should be noted that $CsPbX_3$ normally form orthorhombic crystal structures at room temperature, whilst, $CsPbCl_3$, $CsPbBr_3$, and $CsPbI_3$ hold the tolerance factor of 0.870, 0.862, and 0.851, respectively.²¹ However, stability and structure of perovskites in the nano-scale could change under the influence of other factors, namely, surface energy, surface to volume ratio, and surface passivation.²² In fact, $CsPbCl_3$ and $CsPbBr_3$ nanoparticles with cubic structures have been reported in several studies despite having a low tolerance factor. Linaburg et. al. demonstrated that a modified tolerance factor using bond valence parameters can elucidate the cubic structure of $CsPbCl_3$ with the t value of 0.953.²³

The unexpected stability of CsPbX₃ nanoparticles extends to mixed halide perovskites, like, CsPbCl_xBr_{3-x} and CsPbBr_xI_{3-x} (0<x<3). This characteristic not only provides an easy route to extend the band gap possibilities over the white gamut by post-synthesis processes, but also repurposes the lead halide perovskites as halide reservoir for other reactions.²⁴ In addition, several studies have shown benefits of doping mainly the lead center of CsPbX₃ with Mn²⁺, Zn²⁺, Cu²⁺, Ni²⁺, and Sn²⁺ for applications in optoelectronic devices.²⁵⁻³⁰

1.2.2 Tuning the Band Gap by Nanoparticle's Composition

Many researchers have investigated the band gap and the nature of the valence band and conduction band in either all-inorganic or hybrid perovskite nanoparticles. Experimental measurements using ultraviolet photoemission spectroscopy (UPS), photoemission spectroscopy (PES), and cyclic voltammetry (CV) along with computational calculation such as VASP code, and core-level alignment has confirmed that the conduction band minimum (LUMO) is mostly comprised of p-orbitals of Pb (6p) and the valence band maximum (HOMO) is mostly made of the overlap of p-orbitals (np) of the halides with some contribution from Pb 6s, demonstrated in figure 1.2.a.³¹⁻³⁴ Therefore, band gap energy is dictated by the perovskite composition. In particular, changing the halide composition in perovskites changes the valence band maximum and consequently, the band gap, as shown in figure 1.2.b. This dependency is also illustrated in figure 1.4 by showing how a different halide composition leads to a unique band gap and PL emission. In chapter 4, we show a comparison of the optical and electrochemical band gap in our study.

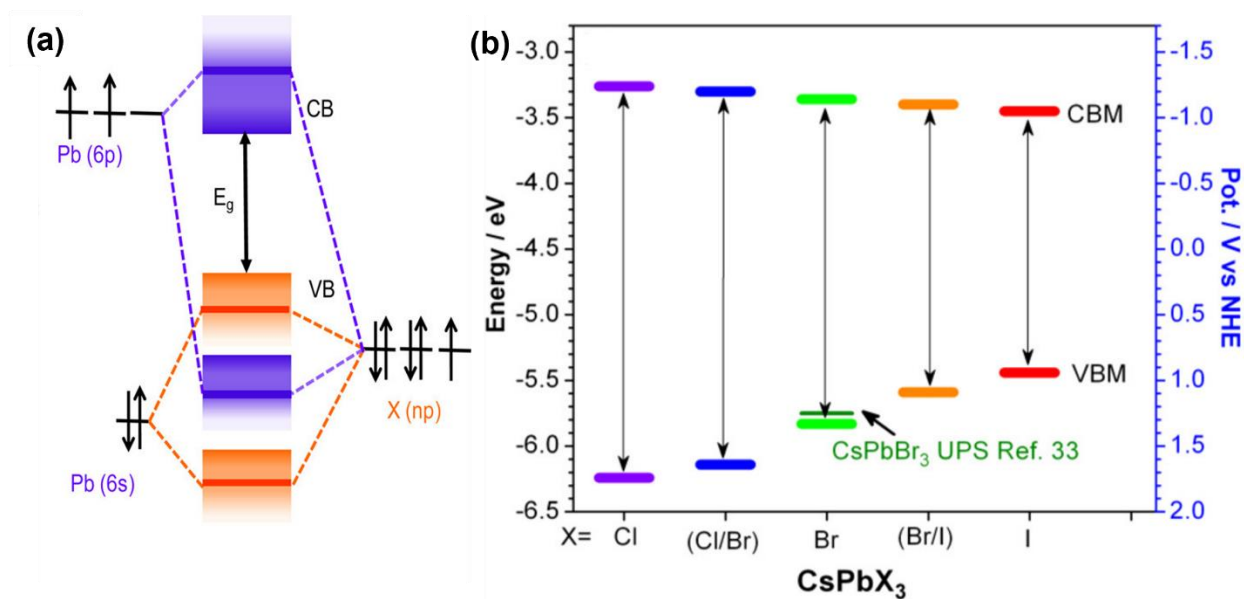
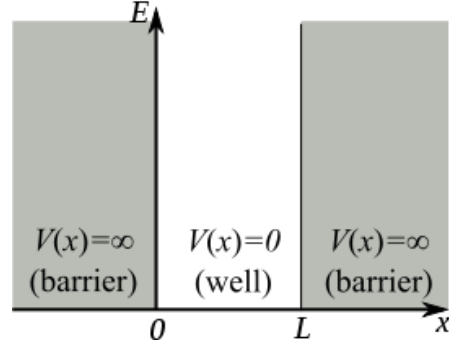


Figure 1.2. Schematic diagram of bonding/antibonding orbitals (a) forming VBM and CBM in CsPbX₃ NPs and band gap energy of CsPbX₃ NPs (b) measured using cyclic voltammetry.³¹

1.2.3 Tuning the Band Gap by Nanoparticle's Dimension

In a perovskite bulk material, e^- and h^+ are located in valence and conduction bands with a defined band gap. However, when the radius of quantum dots is smaller than the Bohr radius (the distance between the e^- and h^+ in an exciton), the energy levels become quantized. In such small dimensions, the exciton in a quantum dot behave similarly to the “particle in a box” in quantum mechanics which means changing the radius of a quantum dot affects the energy levels same as changing the box dimension affects the energy of the particle in a box.³⁵ According to the energy equation for a particle in a box in a one-dimensional system (equation 2), decreasing the length of the box (L) results in an increase in E_n , energy.

$$E_n = \frac{n^2 \pi^2 \hbar^2}{2mL^2} = \frac{n^2 h^2}{8mL^2} \quad \text{Equation 2}$$



Where E_n is the energy of the particle in a box, L is the length of the box, n is the quantum number (a positive integer), \hbar is the reduced Planck constant and m is the mass of the particle.

Likewise, as QDs become smaller, the charge carriers experience the quantum confinement and changing the dimensions of the nano-semiconductors alters the band gap. From molecular orbital theory perspective, less number of atoms in a smaller nanoparticle construct less number of molecular orbitals which in turn, widens the band gap. The energy for electrons in a QD is expressed as:

$$\Delta E = E_{gap} + \frac{\hbar^2}{8r^2} \left(\frac{1}{m_e^*} + \frac{1}{m_h^*} \right) \quad \text{Equation 3}$$

Where m_e^* and m_h^* are the effective masses of electron and hole, respectively.³⁶ As radius of the QD decreases, energy of the electron (or exciton) increases exponentially. The energy of electron is derived from applying the Hamiltonian operator on the wavefunction of the electron. In quantum mechanics, the wavefunction describes the state of the electron such as position, momentum, and energy which for a particle in a box follows a sin function as in equation 4.

Figure 1.3 shows how shorter length (L) of a box affects the shape of the wavefunction as well.

$$\Psi_n(x) = \sqrt{\frac{2}{L}} \sin\left(\frac{n\pi x}{L}\right) \quad \text{Equation 4}$$

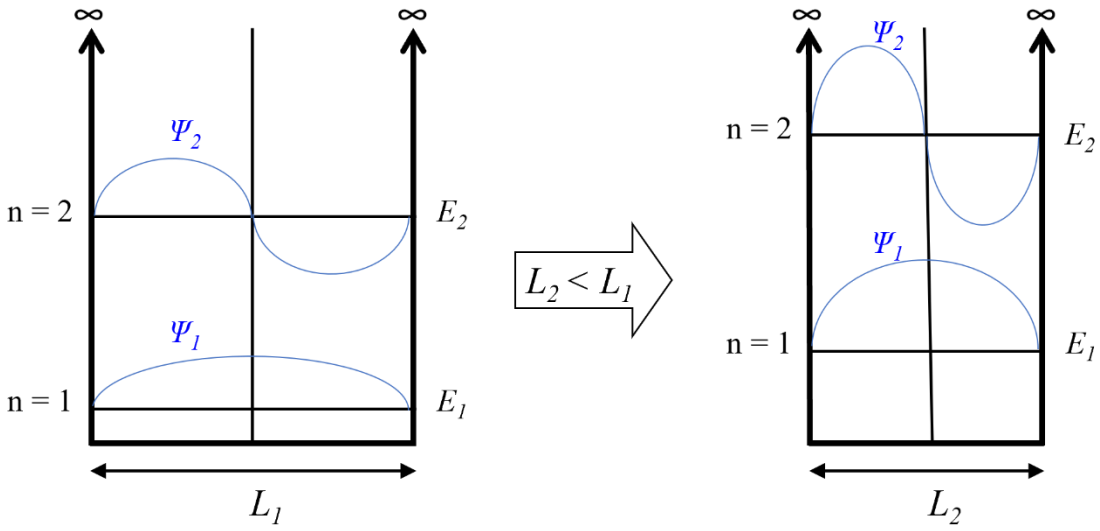


Figure 1.3. Schematic wavefunctions and energy levels of electron in a one-dimensional box for first two energy levels.

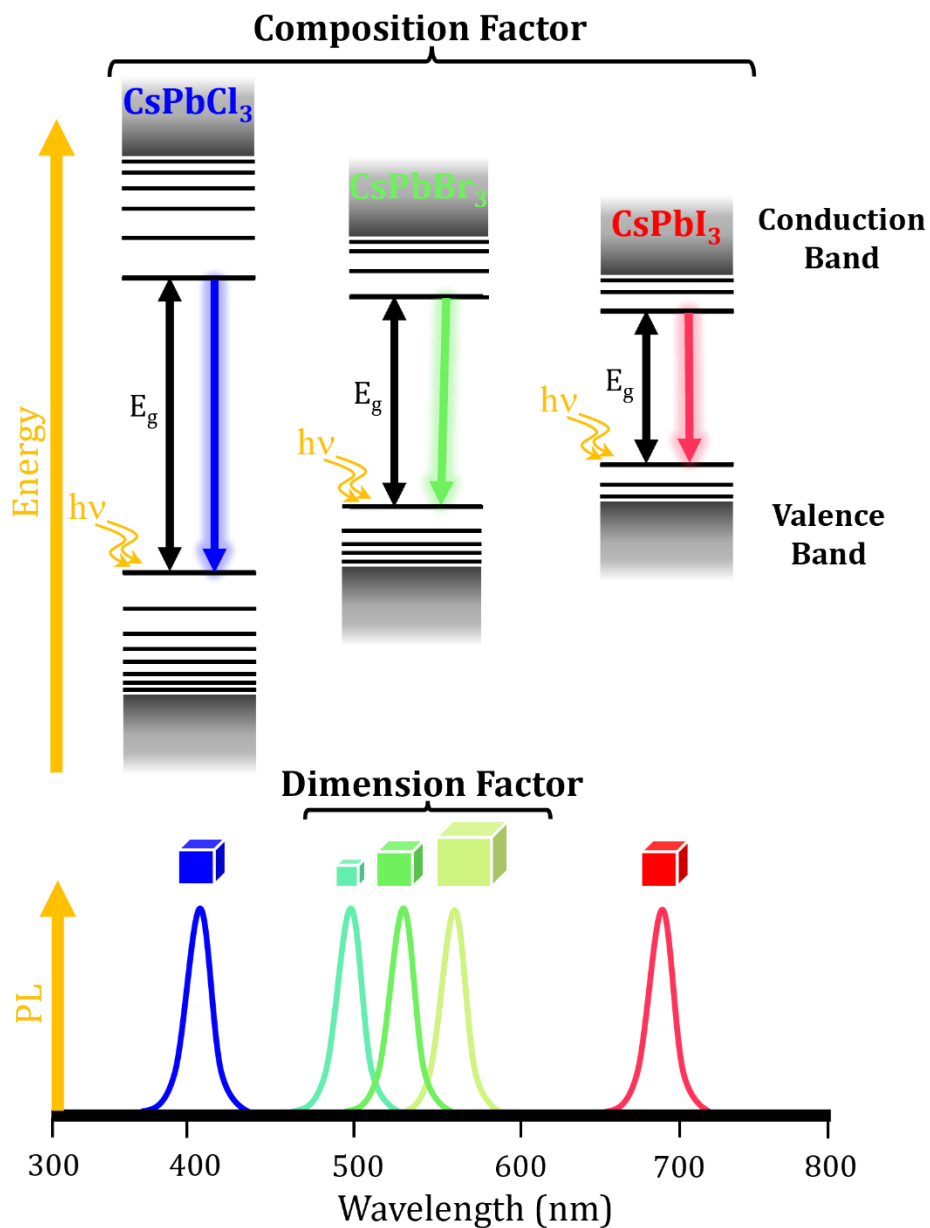


Figure 1.4. Schematic illustration of PL emission and band gap dependency on size and halide composition of perovskite nanoparticles.

1.2.4 Photoluminescence Tunability

Another attraction of perovskite nanoparticles is their tunable photoluminescence in the visible spectrum, outcome of the radiative recombination of excitons. Perovskite nanomaterials can have

a narrow emission with full-width half maximum of 15-25 nm upon absorbing light with higher or equal energy than the band gap. This emission often has slightly lower energy than the band gap and is similarly controlled by the nanoparticle's distinct sizes and composition, represented in figure 1.4. Some studies have shown that the difference between the excitation and emission wavelength, which is called Stokes shift, could also increase by decreasing the nanoparticle's size.^{37,38} This tunable narrow emission has made perovskite nanomaterial an appealing candidate for various light emitting applications. Having a high quantum yield (QY) and a large Stokes shift are some of the other desirable PL properties for devices like LED.

With such tunability in band gap, an all-inorganic CsPbX_3 perovskite nanoparticle could exhibit any band gap value in the near-UV and visible region of the electromagnetic spectrum.

Typically, CsPbCl_3 nanoparticles absorb light with wavelength in the near-UV and blue region, CsPbBr_3 absorbs light in the green, and CsPbI_3 absorbs red light. Moreover, a mixed halide composition during the synthesis of the nanoparticles renders quaternary alloyed perovskites with various band gaps with the span of all the visible region. Producing a quaternary CsPbX_3 is also achievable through post synthesis manipulation of the structure. In chapter 4, we expand on the capabilities of the CsPbBr_3 undergoing halide exchange to produce $\text{CsPb}(\text{Br/I})_3$ nanoplatelets.

1.2.5 Quantum Efficiency

Quantum efficiency or quantum yield (QY) is the efficiency of the semiconductor to convert the absorbed energy to light, hence, it's calculated using the ratio of the number of the emitted photons (PL emission) to the number of the absorbed photons (UV-Vis absorption). Both all-

inorganic and hybrid perovskites have been proven over and over to have a high quantum efficiency which can be even improved till near unity. High QY of the perovskites is particularly superior to the other semiconductor nanoparticles such as CdSe which often has less than %50 QY if the nanoparticles are not protected with a shell.³⁹ This property is the result of a higher radiative recombination in perovskites rather than the nonradiative loss of energy due to the trap states as shown in figure 1.5.⁴⁰

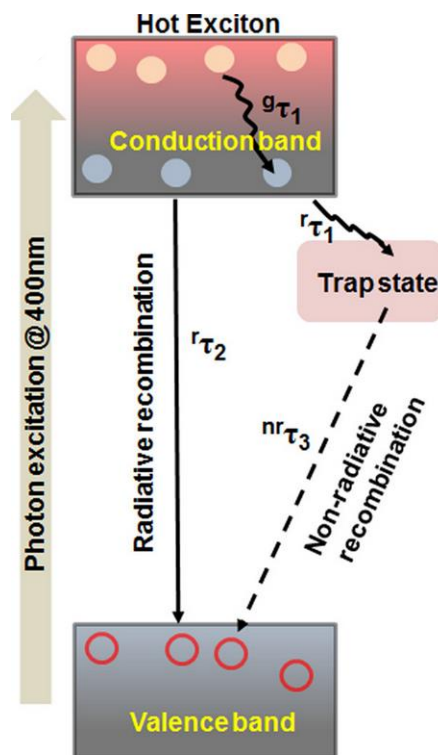


Figure 1.5. Schematic Jablonski diagram showing radiative and non-radiative recombination of excitons for CsPbBr₃ perovskite.⁴⁰

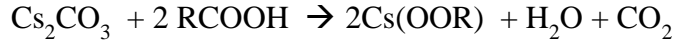
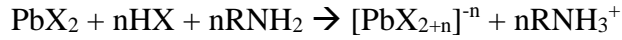
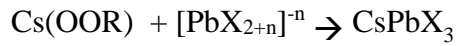
1.3 Synthesis of 2D CsPbX₃ perovskite nanoplatelets

There are various synthetic methods to produce perovskite nanoparticles either at room temperature or in heated conditions which are mainly divided into two categories: bottom-up and top-down synthesis processes. As the name suggests, in top-down synthesis, nanoparticles are

produced from breaking down the bulk material by means of etching, exfoliating or milling.⁴¹

Top-down processes often require a large amount of energy and result in high degree of surface defects.⁴² Bottom-up processes describe several synthesis techniques that start from the ions in a precursor solution. Some of these techniques require a heat treatment such as, hot-injection, solvothermal synthesis, and microwave-assisted synthesis, while others are performed at room temperature, like, template-assisted synthesis, ligand-assisted reprecipitation (LARP) technique and microemulsion. Synthesis methods that have been used to produce perovskite 2D nanoplatelets will be discussed further as is the interest of this dissertation.

In a colloidal CsPbX_3 synthesis, two or three precursors of the constituents are prepared in an organic solvent. Typically, organic ligands with either long carbon chains like, oleic acid, oleyl amine, undecanoic acid, trioctylphosphine oxide, and dodecylamine, or short carbon chains like, acetic acid, hexyl amine, octyl amine and octanoic acid are reacted with cesium, lead and halides at high temperatures to dissolve them in the organic solvent.^{43,44} Researchers have used several compounds to make the cesium precursor, including, cesium carbonate, cesium acetate and cesium halide.^{45–48} While in most studies a PbX_2 solution is used as both lead and halide source of the synthesis, examples of separate precursors of lead and halide using lead acetate and benzoyl halide have been reported as well.⁴⁹ For the first step of the CsPbX_3 synthesis in this dissertation, we adapted the method in our previous study, by combining Cs_2CO_3 and oleic acid in benzyl ether and heating the mixture in 120 °C under an Ar gas flow (step 1).²⁴ During the reaction, H_2O , CO_2 and solvent impurities are vacuumed out of the reaction flask. Similarly in step 2, a PbX_2 solution was dissolved in benzyl ether using oleic acid and oleyl amine as ligands. A controlled reaction between these precursors results in CsPbX_3 nanoparticle formation with desired shape and composition (step 3).

Step 1. Cs(OOR) in ODE/BE**Step 2. Pb(OAc)₂ + (OAm)X⁵⁰ in ODE/BE****Step 3. CsPbX₃ in ODE/BE****1.3.1 Orientational Growth in Perovskite 2D Nanoparticles**

In general, nanoparticles are categorized into three types based on their structure: QDs (0D) or nanocubes, quantum rods (1D) or nanorods and 2D nanoparticles or nanoplatelets. A schematic illustration of these three types is shown in figure 1.6. Many studies have revealed that right selection of synthetic route, ligand type, ligand or precursor stoichiometry, reaction time and temperature of the synthesis can dictate the structure and morphology of the NPs.^{51–55} The effect of these parameters on the orientational growth of the perovskite nanoparticles will be discussed in this section.

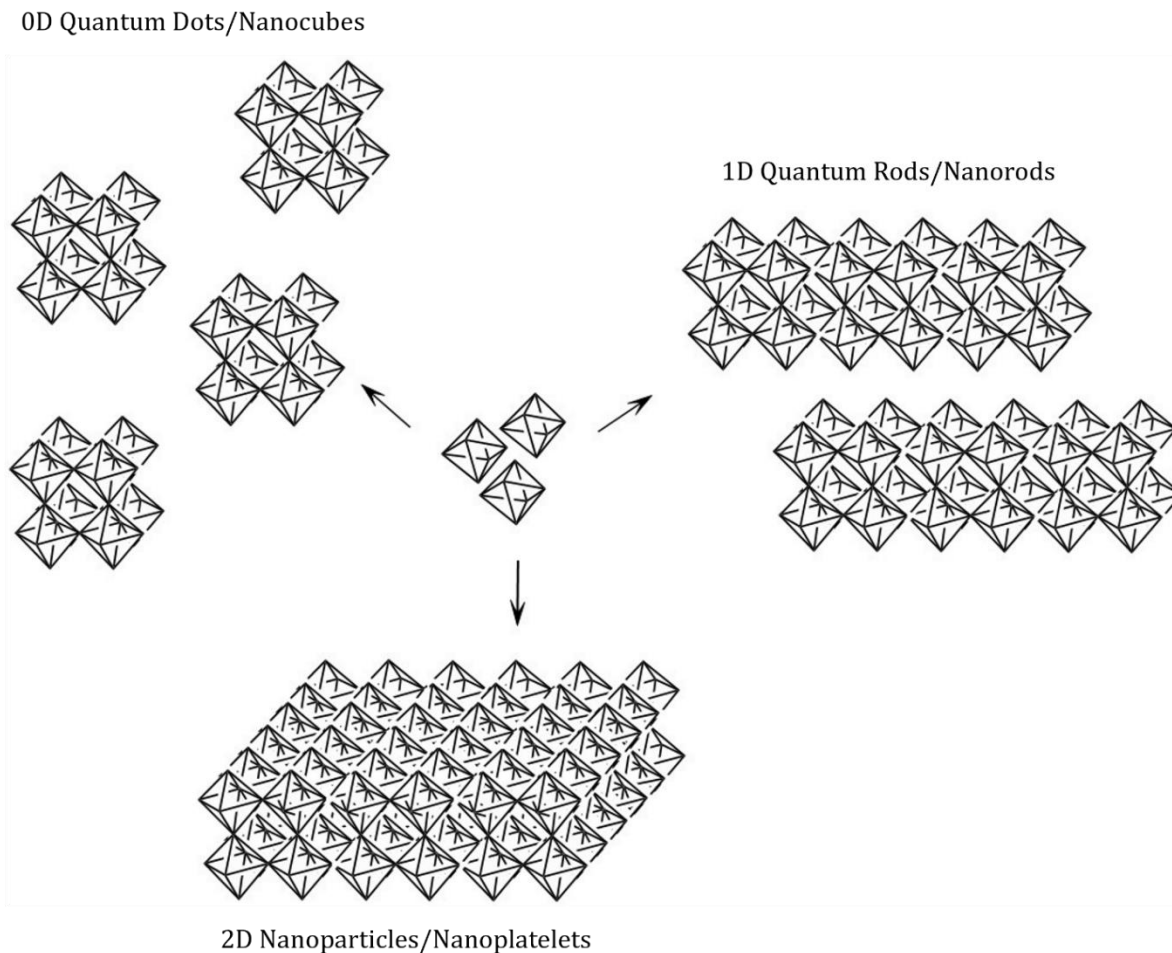


Figure 1.6. Schematic representation of anisotropic growth from perovskite seeds to 0D, 1D, and 2D nanoparticles.

Studies show that anisotropic growth of perovskite nanoparticles is significantly influenced by the type of the ligands and length of their aliphatic chain. However, predicting the precise morphology of the nanoparticles is a complex task and depends on various synthetic parameters. For example, Sun et. al. illustrated that longer chain carboxylic acids facilitated the 2D growth of CsPbBr_3 nanoplatelets in a reprecipitation process.⁵² In the same year, Pan et. al. employed several binary mixtures of several amine and carboxylic acid ligands with different chain lengths

to synthesize CsPbBr₃ via a hot-injection method and concluded that using short chain amines renders thin nanoplatelets.⁴³

In addition, controlling the kinetics of the reaction can yield 2D structures. For instance, it's been shown that temperature of the synthesis can be decreased to slow down the crystallization of perovskite and facilitate the 2D growth.⁴³ In that case, nanoparticles' facets with higher surface energy would grow faster than the other sides. In another study, Burlakov et. al. reported a temperature-controlled synthesis of CsPbBr₃ nanoplatelets in which the wider nanoparticle's facets can be passivated by ligands, while narrower facets will be free to grow.⁵⁶

Another method is to prolong the heating treatment to promote the re-structuring of the nanoparticles to form 2D nanoplatelets. Two mechanisms have been proposed to explain the tendency of nanoparticles to assemble in larger structures over time: (i) Ostwald ripening, (ii) self-assembly (coalescence).

- (i) Ostwald Ripening describes a phenomenon in colloidal solutions where smaller nanoparticles dissolve and deposit on larger particles (figure 1.7).⁵⁷ The reason for smaller nanoparticles to undergo self-destruction is to stabilize the system by minimizing the surface energy. Contrary to the more stable atoms inside the particle, atoms on the surface have less bonds attached to them (more dangling bonds). As smaller particles have a higher surface to volume ratio, they also have a greater number of dangling bonds on the surface and a higher surface energy. Therefore, surface ions dissociate from the small nanoparticles and deposit on the larger ones to reduce the energy.⁵⁸ Ostwald ripening commonly happens over time at ambient conditions.

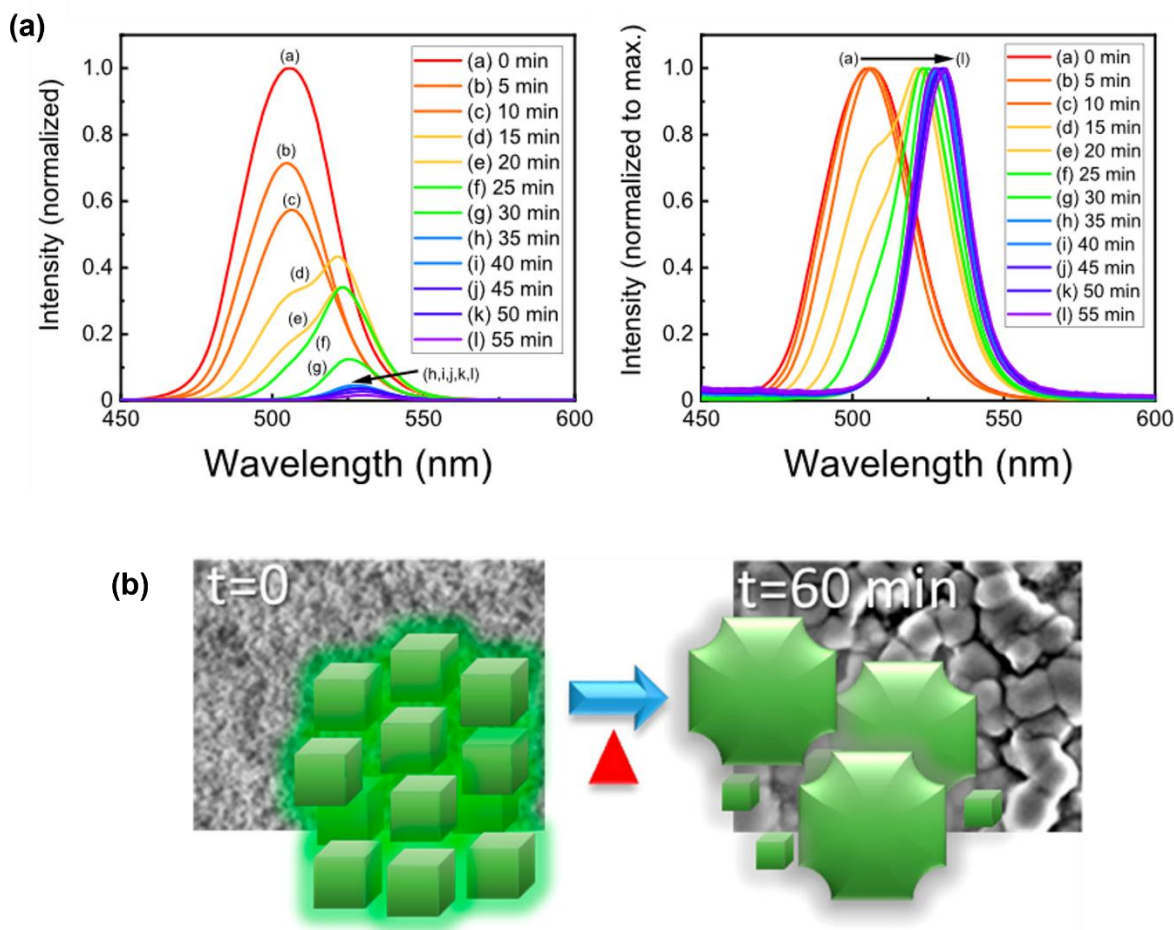


Figure 1.7. PL emission (a), schematic illustration and SEM micrographs (b) showing transition of CsPbBr₃ nanoparticles into bulk films by Ostwald ripening over 60 min at 125 °C.⁵⁸

- (ii) Self-assembly is a process in which smaller nanoparticles connect with each other to construct larger structures (figure 1.8). In this case, smaller nanoparticles like nanocubes come together to make nanorods and nanorods assemble to create nanoplatelets and so on.^{59–62} Driving force of this oriented growth originates in different approaches.⁶³ In one study, it was also shown to be the result of minimizing the surface energy by prolong heating under pressure.⁶⁰ Another study reported that Coulombic forces attract the nanoparticles to each other, which requires a polar solvent to remove the ligands.⁶¹ Others suggested that oriented attachment of the

nanoparticles is an attempt to lessen the Gibbs free energy by Van der Waals interaction between surface ligands.⁵⁹

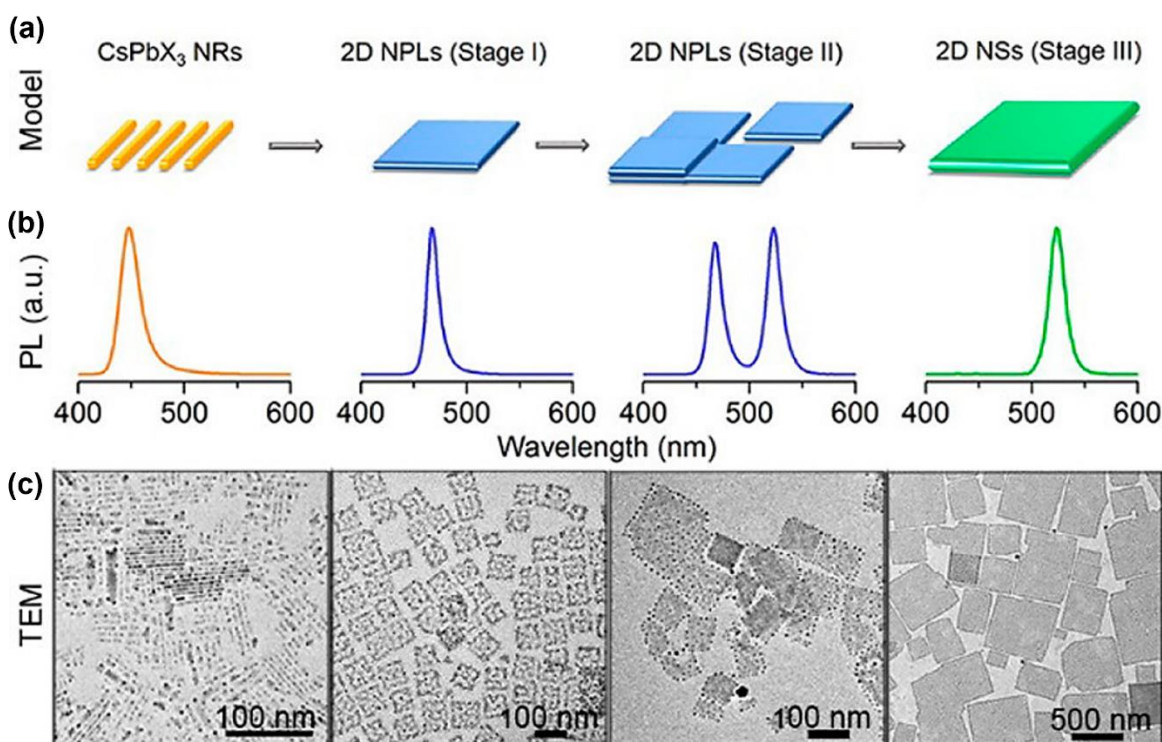


Figure 1.8. Schematic illustration (a), PL emission (b) and TEM micrographs (c) showing CsPbX₃ nanosheets prepared by self-assembly of first nanorods and second nanoplatelets under solvothermal conditions at 160 °C over 5 h.⁶⁰

1.3.2 Solvent Effect on the Morphology of All-inorganic Perovskite Nanoparticles

One of the areas that has not been explored widely is the effect of various solvents in the synthesis on the characteristics of CsPbX₃ nanoparticles. In general, non-coordinating solvents with high boiling points have been recognized as good candidate for CsPbX₃ synthesis. Such solvents like, 1-octadecene (ODE) do not deteriorate the ionic structure of the CsPbX₃ and can be heated to elevated temperatures to enable a fast and uniform seeding and growth of the

nanoparticles. Other nonpolar organic solvents have also shown promising results in CsPbX₃ synthesis. For example, Guo et. al. used octane in a one-pot synthesis of CsPbBr₃ nanocubes.⁶⁴ Their result showed that octane dispersed the nanoparticles and inhibited their self-assembly in contrary to ODE. It is worth noting octane is a volatile solvent that boils at 125 °C. In another study, Kang et. al. compared CsPbBr₃ nanocubes made in ODE, 1-tetradecene and paraffin liquid and discovered that paraffin liquid forms nanoparticles with better size distribution and higher %QY of ~%70.⁶⁵

On the other hand, in methods like LARP and spin coating, precursors are prepared in “good” solvents like DMF and DMSO to enable a complete dissolution of ions, however, stability of the CsPbX₃ nanoparticles depends on the removal of such polar solvents.⁶⁶ Efforts to replace the common solvents in LARP to increase yield and stability have also been successful.^{67,68} Several studies have focused on the interaction of polar solvents with the lead center, specifically, in organic-inorganic lead iodide perovskites. These studies confirmed that the polar solvent is playing a role in the formation of lead halide perovskites by influencing the formation of iodoplumbate complexes.⁶⁹⁻⁷¹

Effect of polar solvents on the properties of CsPbX₃ perovskite nanoparticles has been a point of interest as these solvents are commonly used in the purification procedures. Sun et. al. investigated the post-synthesis addition of polar solvents such as methyl acetate, methanol, ethanol, acetone, and isopropanol to CsPbI₃ nanoparticles.⁷² Among them, methyl acetate preserved the pristine properties of the nanoparticles and thus, it’s a good candidate for purification purposes.^{72,73} However, such solvent interactions could also be manipulated to transform the morphology, post-synthesis. For instance, Jeon et. al. studied the effect of five hydroxyl bearing solvents on the properties of CsPbBr₃ nanoparticles dispersed in hexane.⁶¹ They

discovered that immiscible solvents, like, methanol, ethylene glycol, diethylene glycol and glycerol promoted their growth, while miscible solvents, like, isopropanol and ethanol led to agglomeration or disintegrated the nanoparticles. By precise deduction of these results, 1D and 2D structures were formed using ethylene glycol.

1.3.3 2-D Perovskite Synthesis Methods

As discussed earlier in section 1.2.1, stability of perovskites and simplicity of their synthesis have enabled the scientists to explore a number of various approaches to form CsPbX_3 nanoparticles. Dey et. al. have discussed these methods extensively in their ginormous review on halide perovskite nanocrystals.⁶⁶ In this section, four techniques that have been exploited widely in 2D perovskite synthesis will be discussed further.

1.3.3.1 Ligand-Assisted Precipitation

Ligand-Assisted Precipitation was first applied in perovskite synthesis by Schimdt et. al. to make $\text{CH}_3\text{NH}_3\text{PbX}_3$ (MAPbX_3) nanocrystals in 2014.⁷⁴ Later Zhang et. al. introduced a modified Ligand-Assisted Re-Precipitation (LARP) technique for MAPbX_3 synthesis at room temperature.⁷⁵ In this method, they combined PbBr_2 and MABr with n-octylamine and oleic acid as ligands in N,N-dimethylformamide (DMF) solvent and gradually added the precursor solution into nonpolar solvents like toluene (figure 1.9c). Perovskites crystallize immediately due to supersaturation in toluene and can be tailored to nanoscale dimensions by incorporating long chain ligands. 2D hybrid perovskite structures were soon produced by using octylammonium as a large organic cation which controlled the nanocrystal growth as it could not fit in the 12-

coordination holes between the PbX_6 octahedra.^{76,77} Next year, various precipitation strategies were adapted to produce CsPbX_3 nanoplatelets. Akkerman et. al. synthesized CsPbBr_3 nanoplatelets with 3-5 monolayer thickness by adding acetone to a mixture of precursors in 1-octadecene.⁷⁸ Around the same time, Sun et. al. adapted the Zhang's work in fabricating 2D CsPbBr_3 and showed how different combination of ligands can control the morphology.⁵²

Since then, tremendous work has been done to control and improve the morphology and optoelectronic properties of CsPbX_3 nanoplatelets which has shown size and polarity of the ligands and reprecipitation solvents dictate the lateral dimensions and thickness of the platelets. The ability to fine-tune perovskite nanoplatelets in a facile synthesis in ambient conditions have attracted many researchers to the LARP technique, however, more research is required to improve the QY of the LARP made nanoplatelets.⁷⁹

1.3.3.2 Hot Injection

In 1993, Murray, Norris and Bawendi introduced a new technique called “Hot Injection” to produce highly uniform QDs with tunable optoelectronic properties.⁸⁰ Since then, there were many studies on hot-injection nanocrystal synthesis,^{81–83} but it wasn't until 2014 that Protesescu et. al. adapted the hot-injection method to make all-inorganic CsPbX_3 perovskites.⁶ In this method, organic ligands and non-polar solvents, mainly 1-octadecene, are used to obtain the precursors. To synthesize CsPbX_3 nanoparticles, typically cesium precursor is injected into a hot PbX_2 solution under an inert gas, followed by quenching the reaction by dipping the reaction flask in an iced water (figure 1.9b). Hot-injection has been used widely to obtain monodisperse perovskite nanoparticles. The novelty is in the rapid nucleation upon reacting the precursors at a

high temperature ($\sim 120\text{-}200\text{ }^{\circ}\text{C}$) and halting the nanoparticles' growth with a sudden quench of the temperature.

Several studies showed CsPbX_3 nanoparticles with 0D, 1D, and 2D geometries are achievable via hot-injection synthesis. In one study, lowering the hot-injection temperature to $90\text{ }^{\circ}\text{C}$ resulted in CsPbBr_3 nanoplatelets with up to 300 nm length.⁶² In another study, Shamsi et. al. displayed 200 nm nanoplatelets which were synthesized by prolonging the reaction, on top of that, 2D CsPbBr_3 nanoparticles were grown up to $5\text{ }\mu\text{m}$ by incorporating octanoic acid and octylamine as short ligands in addition to oleic acid and oleyl amine as long ligands.⁸⁴ Although highly luminescent and monodisperse nanoparticles can be produced by the hot-injection route, it requires a great amount of time and energy and ironically, the nucleation and quenching of the reaction is too fast to be carried on in a large scale.

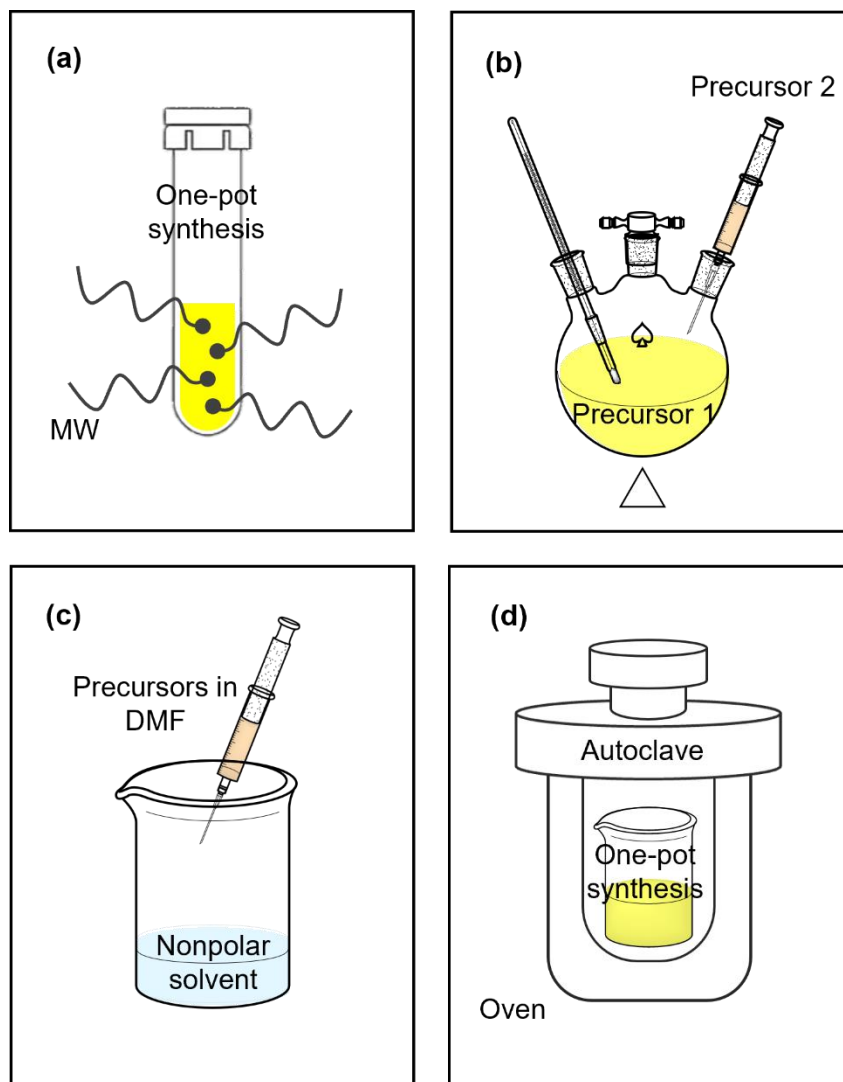


Figure 1.9. Schematic representation of 2D CsPbX₃ syntheses. Microwave-assisted (a), Hot-injection (b), Ligand-assisted precipitation (c), and Solvothermal (d) techniques.

1.3.3.3 Solvothermal Synthesis

Solvothermal synthesis refers to a method in which precursors are heated in temperatures higher than the solvent's boiling point in a sealed autoclave (figure 1.9d). However, the term is interchangeably used for the prolonged nanoparticle syntheses in temperatures lower than the solvent's boiling point, as well. Several studies have used solvothermal method to synthesize CsPbX₃ perovskite nanoparticles in 1-octadecene. Chen et. al. reported the first use of a

solvothermal synthesis to produce CsPbX_3 nanoparticles in 160 °C where undissolved precursors yielded nanocubes and pre-dissolved precursors formed nanowires.⁸⁵ Li et. al. and Zhai et. al. published their results on solvothermal synthesis of CsPbX_3 nanoplatelet around the same time in 2018.^{60,86} These studies showed perovskite nanoplatelets are formed in an extended heat treatment ranging from 30 min to 24 h. Although solvothermal synthesis is an easy one-pot reaction, it is not a cost-effective strategy due to high consumption of energy that is required for the high temperature and pressure over several hours.

1.3.2.4 Microwave-assisted synthesis

Microwave-assisted synthesis is a high through-put, energy efficient method that has been previously shown to be effective in producing chalcogenide QD and noble metal core-shell nanoparticles.⁸⁷⁻⁹⁰ Microwave irradiation (MWI) via a synthetic microwave offers an accelerated synthesis route, homogeneous heating and cooling processes, precise control over reaction and quenching temperatures and a simple set-up. A typical perovskite nanoparticle synthesis can be completed in less than five minutes applying MWI. In general, precursors are combined in the MW vessel prior to heating and reach the elevated synthesis temperature precisely (figure 1.9a). This process eliminates the hot-injection difficulties, however, mixing the precursors at room temperature sets an early stage of nanoparticle seeding and can lead to polydispersity of nanoparticles.^{91,92} Nonetheless, there are several reports of monodisperse nanoparticle synthesis via MWI that show shape and size of the nanoparticles can be tailored by changing the temperature, heating time and power of the microwave.⁹³⁻⁹⁶ Among these studies, some successfully produced 2D CsPbX_3 perovskite nanoplatelets, while most of the syntheses were performed in a household microwave. In a study by Long et. al. a low MW power resulted in 2D

CsPbBr₃ nanoparticles.⁹⁶ Shamsi et. al. utilized the large-scale MW synthesis of CsPbBr₃ nanoplatelets in fabricating an LED with the perovskite film.⁹⁷ Liu et. al. investigated the effects of MW power, heating time and stoichiometry of materials on the morphology of the nanoparticles and showed a higher concentration of oleyl amine can facilitate the anisotropic growth of CsPbBr₃ nanocubes to 1D and 2D structures.⁹³ Pan et. al. demonstrated the first report of 2D CsPbBr₃ synthesis by a synthetic microwave instrument. These nanoplatelets were formed in a one-pot reaction at 80 °C due to the slow kinetics at lower temperature.⁹⁵

1.3.2.5 Heating Mechanisms in Microwave-assisted Synthesis

Microwave-assisted nanoparticle synthesis grants a rapid and uniform heating of the reaction over the conventional heating routes such as heating mantels, oil/water bath or hot plates. In the latter methods, energy is absorbed on the surface and is distributed in the solution through convection or conduction, however, microwaves can pass the reaction vessel and warm up the solution homogeneously. A schematic comparison of the two methods is shown in figure 1.10. A nanoparticle reaction solution usually contains two components, one is the organic parts, including, solvent and ligands and the other is the inorganic elements, for example, cesium, lead and halides or the CsPbX₃ seeds. Once the microwaves enter the media, irradiated organic molecules align their dipole physically with the oscillating electric field of the microwave giving rise to molecular collision and heating of the mixture (dielectric heating).^{98,99} Similarly, ions can move with the oscillating field and generate heat in the solution.¹⁰⁰ It is important that the frequency of irradiation stays within the timespan of the molecule's relaxation time to keep them moving (relaxation time refers to the time required for the molecule to be free of the electric field's effect when irradiation is turned off).⁹² Conventionally, frequency of the microwave

magnetrons is set at 2.45 GHz which corresponds to a relaxation time of 65 ps. While there are several complex factors affecting the absorption of microwaves and relaxation of molecules, when comparing long-chain hydrocarbons versus polar solvents, it is safe to say that polar materials have shorter relaxation times that favors the dielectric heating process. For example, alcohols with shorter aliphatic chains have been shown to have shorter relaxation time and better MW absorbance with relaxation time range of ~ 51 ps for methanol increasing to 976 ps for 1-hexanol.⁹⁸ Therefore, solvents with higher dielectric constants can heat up the system faster and more effectively. The conducting and semiconducting materials could also increase the temperature by conduction which is induced by the electric field (resistance heating).⁹⁸

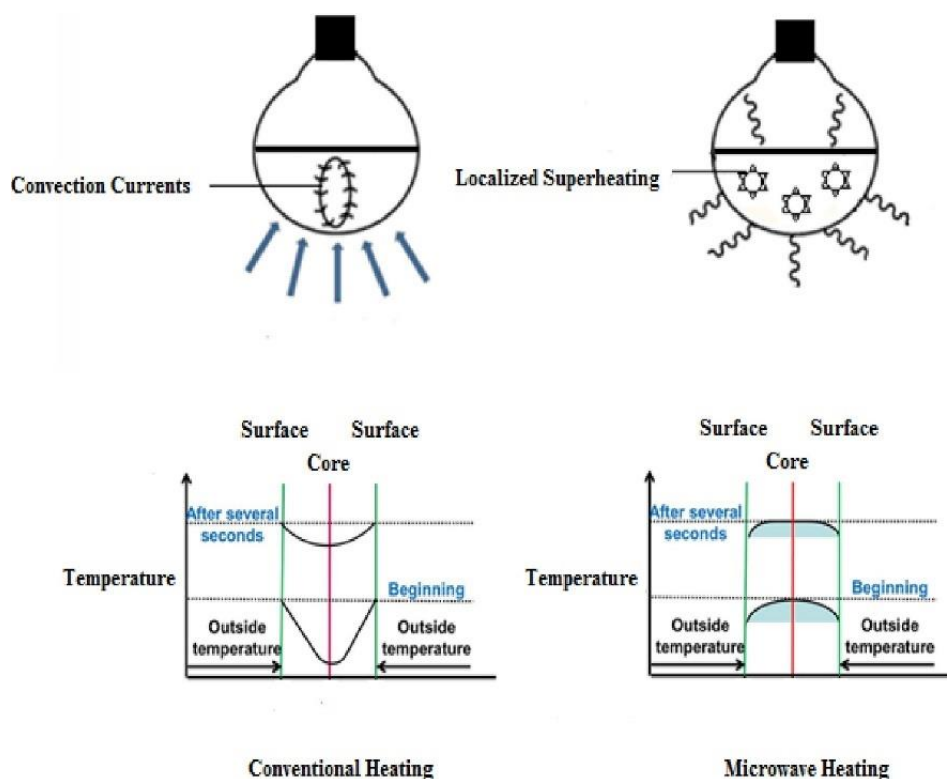


Figure 1.10. Schematic illustration of conventional and microwave heating mechanisms.⁹⁹

Other innovative methods have also been proposed to synthesize 2D CsPbX_3 perovskites. Rao et. al. synthesized 2D CsPbBr_3 nanoplatelets via a one-pot reaction using 80 minutes of ultrasonication.¹⁰¹ Although there are numerous reports on 2D hybrid perovskites fabrication by chemical vapor deposition, 2D all-inorganic perovskite nanoplatelets with a quantum confined facet have been fabricated only recently by Hossain et. al..¹⁰²

1.4 Halide Exchange of CsPbX_3 via Post-Synthesis reactions

As discussed in the section 1.2, CsPbX_3 have a dynamic crystal structure with many possibilities of halide composition. Perovskite halide exchanges are fast, high-yielding reactions with a visual color response. Additionally, they are often performed in ambient condition using a simple one-step reaction. Halide exchange methods have been widely utilized by researchers for various purposes. This feature is mostly advantageous in finetuning the optoelectronic properties of CsPbX_3 nanoparticles where different halide compositions yield nanoparticles with a unique band gap energy. Right after the first report of CsPbX_3 hot-injection synthesis, halide exchange was demonstrated to be an effective approach in achieving perovskite nanoparticles with mixed halide compositions. Nedelcu et. al. followed two methods to obtain $\text{CsPb}(\text{Br/I})_3$ and $\text{CsPb}(\text{Cl/Br})_3$ nanoparticles, first they reacted the CsPbBr_3 with either PbI_2 or PbCl_2 precursor solutions, second, they combined CsPbBr_3 with either CsPbCl_3 or CsPbI_3 nanoparticles (figure 1.11).¹⁰³ Other forms of halide salts, such as, alkylammonium halides, cesium halides, hydrohalic acids, and alkyl halide silanes could also be reacted with CsPbX_3 for halide exchange purposes.^{24,104–107}

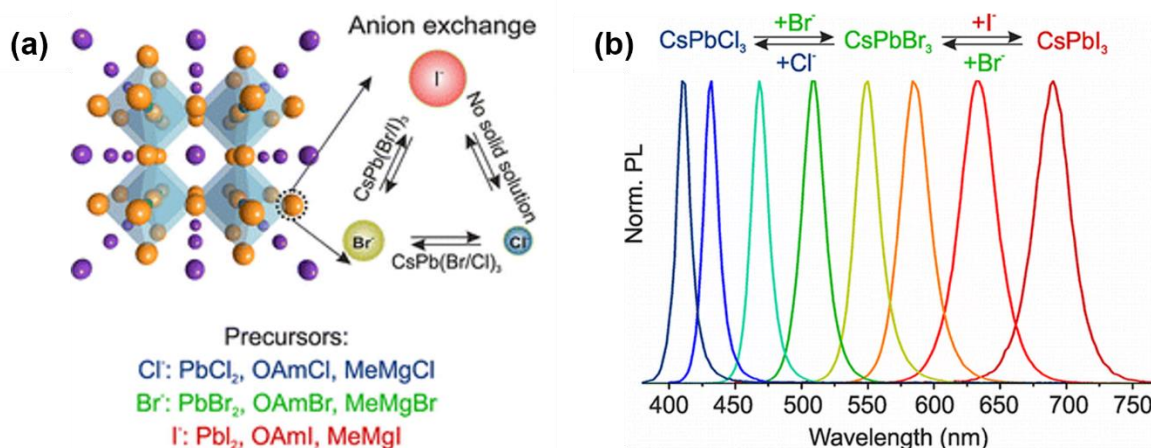


Figure 1.11. Schematic representation of a perovskite cubic crystal structure and its halide exchange (a). Normalized PL emission (b) of CsPbX₃ nanoparticles formed via halide exchange between CsPbBr₃ nanoparticles and either CsPbCl₃ or CsPbI₃.¹⁰³

Halide exchange is particularly desired when nanoparticles with different composition synthesized via mixed precursor routes, do not match in their size and morphology or develop unexpected properties. For example, several studies have confirmed that I-rich CsPbX₃ formed with halide exchange are more stable and retain the initial properties of CsPbBr₃ nanoparticles, as opposed to the synthetic CsPbI₃.^{106–108}

Moreover, halide exchange extends the application of perovskites as an active reactant of halide involving reactions. Doane et. al. introduced the halide exchange reaction of perovskites as a way to tailor organohalide molecules (figure 1.12). They showed that CsPbI₃ nanoparticles exchange I⁻ with Br⁻ of 2-bromododecanoic acid with a quantitative PL emission and a visual color response.²⁴ Halide exchange can also be implemented in sensing applications through reaction with halide bearing organic molecules. Recently, Yin et. al. utilized CsPbBr₃ to detect 10²-10⁴ ppbv traces of methyl iodide which is a toxic chemical used in pesticide.¹⁰⁹

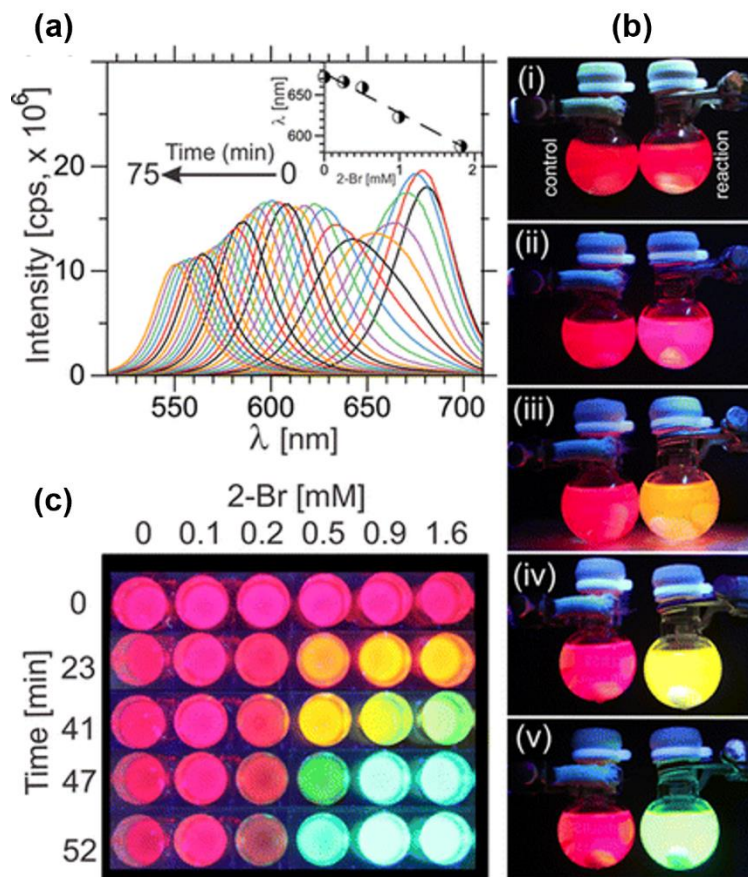


Figure 1.12. Spectral (a) and visual (b,c) PL emission over the course of the halide exchange reaction between CsPbI_3 and 2-bromododecanoic acid under UV light. Images of the Finkelstein reaction next to CsPbI_3 (left) as control (b). Visual PL emission (c) of the reaction controlled by the 2-bromododecanoic acid concentration and time.²⁴

1.4.1 Halide Exchange of CsPbX_3 deposited on a Substrate

One of the most promising applications of CsPbX_3 perovskites is in the photovoltaic devices, notably due to their higher stability in heat and moisture compared to the organic-inorganic lead halides. In particular, CsPbI_3 thin films are great candidates for solar cell materials due to their smaller band gap (1.73 eV) and wide light absorption in the UV and visible region.¹¹⁰ However, synthesized CsPbI_3 NPs often differ from the desired properties in shape, QY and crystal structure, plus they tend to transform to a photoinactive yellow phase at room temperature.

Several reasons have been suggested to explain this anomaly. For instance, it has been demonstrated that I-rich CsPbX_3 perovskites have low surface ligand density.¹⁰⁸ Also, CsPbI_3 with a Goldschmidt tolerance factor of 0.85 deviates from a cubic perovskite structure more than CsPbBr_3 which triggers its transformation to the yellow phase (orthorhombic).¹¹¹ Hence, a high number of publications have focused on producing CsPbI_3 from CsPbBr_3 perovskites by means of halide exchange in order to tailor the proper structural and optoelectronic properties. For CsPbI_3 to be applicable in optoelectronic devices, it is generally deposited on a substrate and assembled within a multi-layer device.

Chemical vapor deposition and spin-coating are the most common methods to deposit CsPbX_3 nanoparticles on a substrate or fabricate a perovskite film.^{97,102,112–114} CsPbX_3 nanoparticles could also be coated on a surface by crystallization or other chemical processes.¹¹⁵ Then halide exchange can be performed on a perovskite film by a second vapor deposition of I or an *in-situ* reaction with I in a solution.^{116,117} Although these techniques employ perovskite films with thicknesses much higher than the quantum confinement limits, they facilitate the study on the industrial applications of CsPbX_3 . Zhang et. al. investigated the mechanism of halide exchange on a single CsPbBr_3 nanoplatelet by vapor phase anion exchange and suggested a two-step process containing an initial surface reaction followed by solid-state diffusion.¹¹⁸ This results in a vertical halide gradient in the film which have been previously suggested to be of use in directing charge carriers in photovoltaic devices (figure 1.13).¹¹⁶ More research is required to understand the effect of the heterogeneous structure in an optoelectronic device or establish a halide exchange route that would result in a stable homogeneous $\text{CsPb}(\text{Br/I})_3$ film.

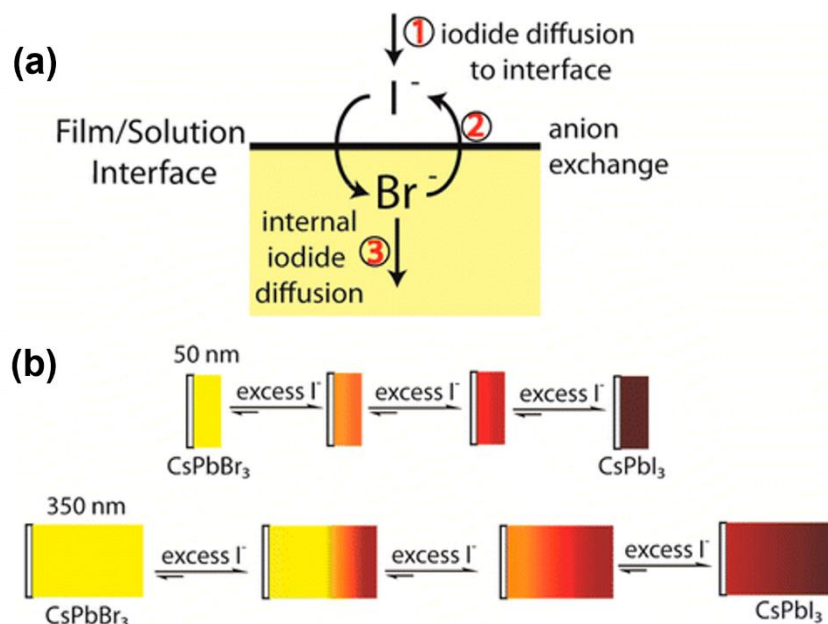


Figure 1.13. Schematic representation (a) of halide exchange in a CsPbBr₃ film. Gradient halide exchange (b) in thin (50 nm) vs thick (350 nm) films.¹¹⁶

1.5 Applications

Perovskite industry has entered a new era of practicality by the launch of the first perovskite photovoltaic cells in Poland in June 2021. Perovskites have had the sharpest increase in the power conversion efficiency than any other rival solar cell materials with a jump from 3.8% in 2009 to 25.2% in 2021.^{119,120} However, the most promising solar cells are believed to be made of a perovskite/silicon tandem which can absorb a wider range of the solar spectrum.¹²¹

Properties that have been discussed so far, like, absorption and emission tunability, and high QY in addition to large absorption coefficient, high charge mobility, direct band gap, low non-radiative recombination rates and long carrier lifetime have made 2D all-inorganic perovskites a suitable material not only for photovoltaic cells but various optoelectronic devices such as LEDs, lasers, and photodetectors.^{7,122–128} TV manufacturers have also successfully incorporated perovskite nanocrystals in TV displays. Previously, CdSe and InP QDs were applied in liquid

crystal displays (LCD), though Chen et. al. showed the superiority of a perovskite QD/polymer film driven by its high brightness and PL QY along with a thin structure.¹²⁹

Moreover, their dynamic crystal structure and high reactivity have given the scientists the opportunity to explore perovskites' application in sensing and catalysis. On top of that, visual and spectral sensitivity can provide a great route to monitor the efficiency and progress during these reactions as discussed in section 1.2.4. Not only CsPbX_3 could be used in sensing halides via halide exchange, but also many reports of doping the A-site and B-site of the nanocrystals have been published in recent years. Such reactions can easily be monitored by changes in PL emission wavelength. In addition, other ions or organic molecules were successfully detected from PL quenching of the CsPbX_3 originated in disruptions on the surface or dissociation of the particles.⁶⁴

1.6 Research Summary

The main goal of this dissertation is to explore a novel technique to synthesize 2D all-inorganic perovskite nanoplatelets and to explain the necessary conditions and underlying causes of their 2-dimensional growth. Chapter 1 is an introduction to this topic in order to provide an understanding of the properties of 2D perovskite NPs, their common synthesis methods, and growth mechanisms. Post-synthesis halide exchange reaction of these NPs is also expanded on to lay down a background regarding synthesis of I-rich nanoplatelets reported in chapter 4. In chapter 2, we describe the synthesis of CsPbBr_3 nanoplatelets using MWI-based heating and BE as the solvent. Their optical and structural properties are compared with the nanocubes prepared with the same method in ODE. TEM and SEM micrographs along with AFM images successfully presented a 2D nanostructure. Interestingly, the intensity of the XRD peaks deviated

from the standard perovskite crystal which proved reproducible for each batch. Therefore, the XRD pattern and intensity was used as an indicator of the perovskite 2D growth in this research. The aim of the chapter 3 is to elucidate the mechanism of the nuclei formation and 2D growth in CsPbBr₃ nanoplatelets. Synthetic conditions are examined in this section via several control experiments and a hypothesis regarding the growth mechanism is suggested. While Br-rich nanoplatelets can be synthesized with this method reproducibly, I-rich nanoplatelets did not present the same 2D signatures of the CsPbBr₃ nanoplatelets in the XRD. To confront this problem, the I-rich nanoplatelets were fabricated by halide exchange reaction of CsPbBr₃ with PbI₂. In chapter 4, we reported the properties of the I-rich nanoplatelets and the methods that were employed in this study. The halide exchange mechanism is also investigated using various reactions and comparison with nanocubes. In addition, a modified method is used to accomplish a total conversion of halides in the CsPbBr₃ nanostructures illustrated by *in-situ* PL emission spectra and XRD analyses. An overview picture of this study and the findings are reported in chapter 5 and future directions are suggested as well.

Chapter 2 – Microwave-Assisted Synthesis of 2D CsPbBr₃ Nanoplatelets

Abstract

This study describes an investigation of the role of non-polar solvents on the growth of cesium lead halide (CsPbX₃ X = Br, I) nanoplatelets. We employed two solvents, benzyl ether (BE), and 1-octadecene (ODE), as well as two nucleation and growth mechanisms, one-pot, facilitated by microwave irradiation (MWI) based heating, and hot-injection, using conventional heating. Using BE and MWI, large mesoscale CsPbBr₃ nanoplatelets were produced, whereas use of ODE produced thin small crystallites. Differences between the products were observed by optical spectroscopies, which showed first band edge absorptions consistent with thicknesses of ~ 9 nm (~15 monolayer (ML)) for the BE-CsPbBr₃, and ~5 nm (~9 ML) for ODE-CsPbBr₃. Both products had orthorhombic crystal structure, with the BE-CsPbBr₃ revealing significant preferred orientation diffraction signals consistent with the asymmetric and two-dimensional (2D) platelet morphology. The differences in final morphology were also observed for products formed via hot-injection, with BE-CsPbBr₃ showing thinner square platelets with thicknesses of ~2 ML, and ODE-CsPbBr₃ showing similar morphologies and small crystallite sizes. To understand the role solvent plays in crystal growth, we studied lead plumbate precursor (PbBr_n²⁻ⁿ) formation in both solvents, as well as solvent plus ligand solutions. The findings suggest that BE dissolves PbBr₂ salts to a higher degree than ODE, and that this BE to precursor affinity persists during growth.

2.1 Introduction

All inorganic cesium lead halides (CsPbX_3 , $\text{X} = \text{Cl, Br, I}$) and hybrid methylammonium lead halides (MAPbX_3) are important functional materials^{43,130–133} that can be synthesized as crystals, thin-films, and nanomaterials with varied morphologies.^{133,8–13,127,128,134} Two dimensional (2D) plates and platelets are common, with thicknesses of only a few monolayers (ML) often observed, and lengths varied from nanometers to microns, which are formed during nucleation and growth, or self-assembled via solvent and or ligand mediated interactions.^{54,78,84,86,132,135,136} Studies have revealed that control over ligand types and stoichiometry,⁸⁴ as well as time and temperature of the synthesis can render various morphologies.^{43,53,54,56,62,84,86,93,115,137–142} Sonication,¹⁴³ solvothermal,^{86,60,61} mechanochemical,¹⁴⁴ and microwave irradiation (MWI)⁹³ have also been employed to control CsPbBr_3 growth. Studies have shown that Ostwald ripening,^{57,58} and long-ranged growth that includes oriented attachment of smaller building blocks (cubes, rods, *etc.*) renders 2D growth into nanoplatelets.^{60–62,145}

The role that solvent plays in CsPbBr_3 growth has been explored,^{60,69,146–148} and the role it plays in the dissolution and solvation of PbX_2 salt into PbX_n^{2-n} plumbate complexes. This is particularly interesting as the varied lead centered polyhedra formed will have different charges, molecular weights, solubility, as well as concentration and reactivity. The dynamic equilibrium between plumbates is sensitive to the Lewis basicity of the solvents and ligands involved, as well as temperature. To date, studies have focused primarily on polar solvents and their role in plumbate formation, with nitrogen or sulfur bearing solvents (*e.g.*, DMF, DMSO) acting as stabilizers of PbX_n^{2-n} .¹⁴⁹

In this report, we study whether non-polar, high boiling point solvents can tune CsPbBr_3 growth at both low and high temperatures, with the latter being used to compare a one-pot growth

mechanism, facilitated by microwave irradiation (MWI), and a hot-injection mechanism, via convection. The findings indicate that these solvents do tune PbX_n^{2-n} formation, leading to controlled CsPbBr_3 growth and properties.

2.2 Experimental

2.2.1 Materials

Lead iodide (PbI_2 , 99%), lead bromide (PbBr_2 , 99.99%), cesium carbonate (Cs_2CO_3 , 97%), methyl ammonium iodide (MAI, 98%), oleyl amine (OAm, 70%, technical grade), oleic acid (OAc, 90%), 1-octadecene (ODE, 90%), benzyl ether (BE, 98%), N,N-Dimethylformamide (DMF, anhydrous, 99.8%) were purchased from Sigma Aldrich and used as received unless otherwise noted.

2.2.2 Methods

2.2.2.1 Precursor Preparation

In a typical one-pot reaction, precursors were first prepared by adding 0.80 g of Cs_2CO_3 to 30 mL of solvent (ODE or BE), along with 2.4 mL of OAc and the mixture was heated at 120°C under vacuum until all was dissolved (0.15 M Cs-OAc). Likewise, 0.28 g of PbBr_2 or 0.34 g of PbI_2 in 20 mL solvent was heated at 120°C for 1 h under vacuum. Next, 2 mL of OAc and 2 mL OAm was added to the mixture under Ar and the mixture was heated at 120°C for another hour for a complete dispersion of a 0.03 M PbX_2 stock solution. Trials were also run using purified OAm,¹⁵⁰ as were reactions where Cs_2CO_3 was reacted with OAc at higher ratios.¹⁵¹

2.2.2.2 One-Pot MWI Heating and Synthesis of CsPbX_3

In a typical one-pot MWI heated reaction, 3 mL of the as-prepared PbX_2 precursor was purged with Ar gas for 5 min at room temperature. Next, 200 μL of the cesium oleate precursor solution was heated to 85°C and injected to PbX_2 solution followed immediately by MWI heating to 160°C

°C where the trajectory of the heat transfer was different between BE and ODE, and depends on the dielectric constant (ϵ) of the non-polar solvents.⁹² The BE reaction ($\epsilon = 3.82$) reached 160 °C within 100 seconds, while the ODE reaction ($\epsilon = 2.25$) reached after 240 s. Upon reaching this set point, there was a rapid quenching of temperature by the active cooling of the MWI reactor. These prepared nanoplatelets were purified by centrifuging 1 ml aliquots at 10,000 rpm for 3 min, followed by the discarding of the supernatant and redispersion in toluene aided by sonication. This procedure was repeated at least two times, except in the case of FTIR sample preparation, in which additional purification steps were used.

2.2.2.3 Hot Injection and Conventional Heating Based Synthesis of CsPbX₃

First, a 0.15 M Cs-OAc precursor was prepared as described in the precursor preparation section and was stored at 85 °C prior to injection. To prepare the PbBr₂ precursor, a mixture of 0.14 g PbBr₂ powder and 10 mL BE was heated under vacuum at 120 °C for 1h. Then, the mixture was placed under Ar and 1 mL OAm and 1 mL OAc were injected to dissolve the powder. After 1 h, temperature was raised to 140 °C. Next, 0.8 mL Cs-OAc was injected to the solution, and the reactions were let to anneal for 1, 30, and 60 min before removing the heating mantle to quench the reaction. The products were purified as described above. This method was also used for the room temperature syntheses described, except that all reactants were cooled to room temperature before initiation.

2.2.2.4 BE-CsPbI₃ synthesis via Halide Exchange of BE-CsPbBr₃

Prior to the halide exchange (HE), BE-CsPbBr₃ were purified and redispersed in toluene to the approximated concentrations.¹⁵² This solution was then combined with an aliquot from a 0.20M

PbI₂ stock solution so that the combined $[I^-]:[Br^-] = 1$, following a method recently developed in our lab.¹⁰⁸ The mixture was allowed to react for 30 min, then PL emission was measured. For XRD measurement, a portion of the mixture was separated, purified and drop-casted on a zero-diffraction quartz substrate. The rest of the mixture was centrifuged and redispersed in toluene to the initial volume to remove the free Br⁻ in the solution. In the second step, PbI₂ with the same ratio of 1:1 was added to the remaining solution, followed by XRD and PL measurements.

2.2.2.5 Benesi-Hildebrand Analysis

The competitive assay analysis was performed by first preparing a 0.1 M MAI in BE. Next, MAI aliquots were added to a diluted BE-PbI₂ at a ratio of $[MAI]:[PbI_2] = 1-35$. The resulting Iodoplumbate complex formation was monitored by UV-vis spectroscopy.

2.2.3 Instrumentation

Microwave Irradiation (MWI) Heating

A Discover-SP (CEM Inc.) microwave synthesizer with magnetron frequency of 2450 MHz was employed for the MWI, while temperature, power and time of the process were controlled by Synergy software. Each reaction was stirred in a 10 mL glass vial during which temperature was monitored by a volume-independent IR temperature sensor. To stop the reaction, samples were cooled down by compressed N₂ circulating inside the microwave chamber.

UV-Visible Absorption Spectrophotometry (UV-Vis)

The UV-Vis measurements were collected on a Cary 50 Bio UV-Vis spectrophotometer (VARIAN Inc.) between 300-700 nm. Absorbance of each sample was less than 0.1 to reduce reabsorption effects in photoluminescence measurements.

Photoluminescence Spectroscopy (PL)

PL emission spectra were collected on a Cary Eclipse fluorescence spectrophotometer (VARIAN Inc.). The excitation wavelength was set at 400 nm and excitation and emission slit widths were set at 5 nm.

Powder X-ray Diffraction (XRD)

XRD spectra were produced using D2 PHASER (Bruker) instrument with a Cu-K α radiation source (1.5406 Å). Samples were prepared by drop-casting purified NPs on a zero-diffraction quartz holder, followed by drying in a Savant Speed Vac Sc110 vacuum. XRD results were measured with the 2 θ ranging from 10 to 50 ° and the increment of 0.05°.

Transmission Electron Microscopy (TEM)

Prior to TEM measurement, samples were diluted several times and then drop-casted on a carbon coated grid. TEM images of the samples were developed using JEM 2100F field emission TEM (JEOL), operated at 200 kV at the Analytical and Diagnostics Laboratory (ADL) at the State University of New York at Binghamton. Particle size distribution was analyzed manually using ImageJ software on populations of at least 100 counts.

Atomic Force Microscopy (AFM)

AFM imaging was performed on a Digital Instrument Nanoscope IIIa in tapping mode using an E-scanner. Silicon AFM tips (μ Masch, HG:NSC14 / AIBs) were used which had a typical resonance frequency of ~160 Hz. Samples were prepared by drop-casting purified NPs on a HOPG substrate, followed by drying in a Savant Speed Vac Sc110 vacuum.

Fourier Transform Infrared Spectroscopy (FTIR)

FTIR spectra was collected using a Thermo Nicolet 6700 FTIR equipped with a diamond smart iTR attenuated internal reflectance accessory, and a liquid N₂ cooled MCT-A detector. Samples were prepared by three rounds of purification in toluene with centrifugation at 4k rpm for 10 minutes in a glass tube. Samples were then drop-casted on the iTR diamond and air-dried prior to the measurement.

2.3 Results and Discussion

Figure 2.1a shows a schematic illustration of the synthetic conditions tailored to understand CsPbBr₃ growth using either benzyl ether (BE) or 1-octadecene (ODE) as non-polar high boiling point solvents, cesium carbonate dissolved and complexed with oleic acid (OAc) and lead plumbate (PbBr_n²⁻ⁿ)^{69,153–155} formed via dissolving in solvent (S) and ligands (L), as described in the experimental section. The products of these reactions are denoted as BE-CsPbBr₃ or ODE-CsPbBr₃. Two nucleation and growth mechanisms were studied, so-called one-pot and hot-injection, at either high temperature or low temperature.

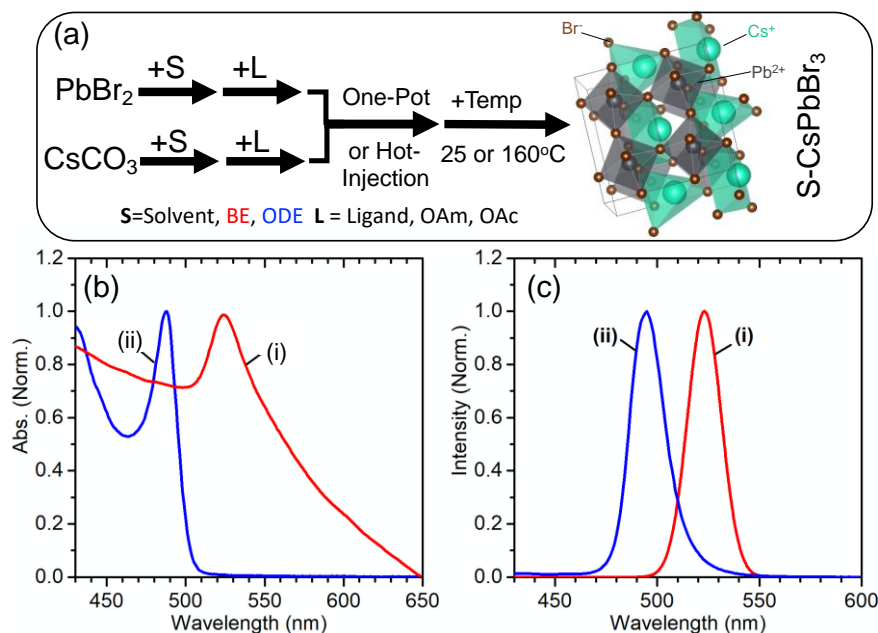


Figure 2.1. (a) Schematic overview of the reaction systems used in this study. UV-vis (a) and PL emission (b) spectra of the BE- (i), and ODE-CsPbBr₃ products prepared via MWI heating to 160 °C.

A one-pot mechanism using microwave irradiation (MWI) as the heating source was first employed, and the synthesis mixtures were heated to 160 °C. Upon cooling, the reaction solution had changed color from a light translucent yellow to a turbid orange, which if left overnight, would settle for the BE-CsPbBr₃ products, but not for the ODE-CsPbBr₃. After collection and

purification, the resulting optoelectronic properties were measured. Figure 2.1b shows the UV-visible absorption (UV-vis) results. The BE-CsPbBr₃ had a first excitonic absorption peak at 523 nm (i), while the ODE-CsPbBr₃ absorbed at 488 nm. Both products exhibited photoluminescence (PL), as shown in Figure 2.1c, with BE-CsPbBr₃ emitting at 527 nm (i), and ODE-CsPbBr₃ at 495 nm (ii). The red-shift indicates either larger sizes or thicker platelets for BE-CsPbBr₃. The band edge absorption is quantized by the minimum CsPbBr₃ dimension, especially when sizes are comparable to the exciton Bohr radius (a_B), which for CsPbBr₃ is ~ 7 nm. Using the studies reported by others,^{62,78,137,156} we estimate a thickness of >15 monolayers (ML), where ML is defined a linear chain of corner sharing PbBr₆⁴⁻ octahedra with thickness of 0.59 nm, for the BE-CsPbBr₃, corresponding to approximate thickness of 8 \sim 9 nm. We note that the absorption is broad, indicating a polydisperse sample and distribution in thicknesses. Using the same approach, the ODE-CsPbBr₃ would have a minimum feature size of ~ 9 ML, or ~ 5.3 nm.

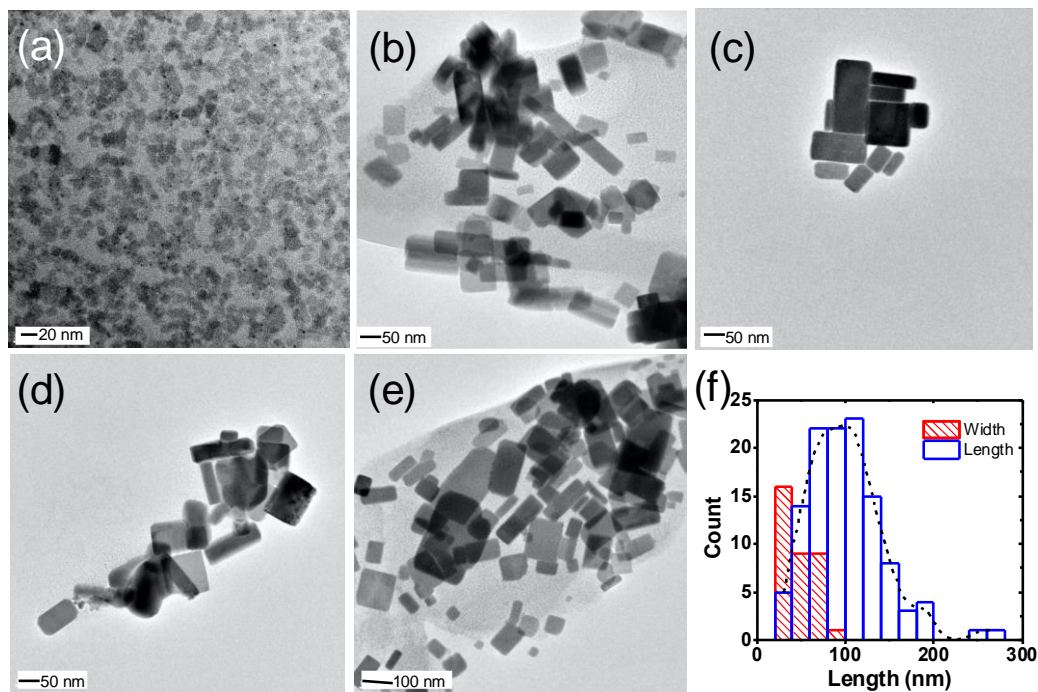


Figure 2.2. Representative TEM micrographs of ODE-CsPbBr₃ (a) and BE-CsPbBr₃ products (b-e) Size analysis histogram of BE-CsPbBr₃ showing platelet 2D dimensions (f).

The dimensions and morphology of the two products were characterized using transmission electron microscopy (TEM). Figure 2.2a shows a micrograph for the ODE-CsPbBr₃ products, which has small square like lateral morphology with an length of $\sim 9.7 \pm 0.8$ nm, which combined with the optical data above is ~ 5 nm thick, and is consistent with other ODE based CsPbBr₃ platelets. In contrast, the BE-CsPbBr₃ products had larger 2D platelet like morphology, as shown in Figure 2.2b-e. The large platelet morphology of the products was highly reproducible; however, the lateral dimensions were polydisperse. For example, the platelets largest length varies from 20 - 500 nm. The platelets were indeed thin, as suggested by the UV-vis, as illustrated in the TEM micrographs where the platelets orient on top of another.

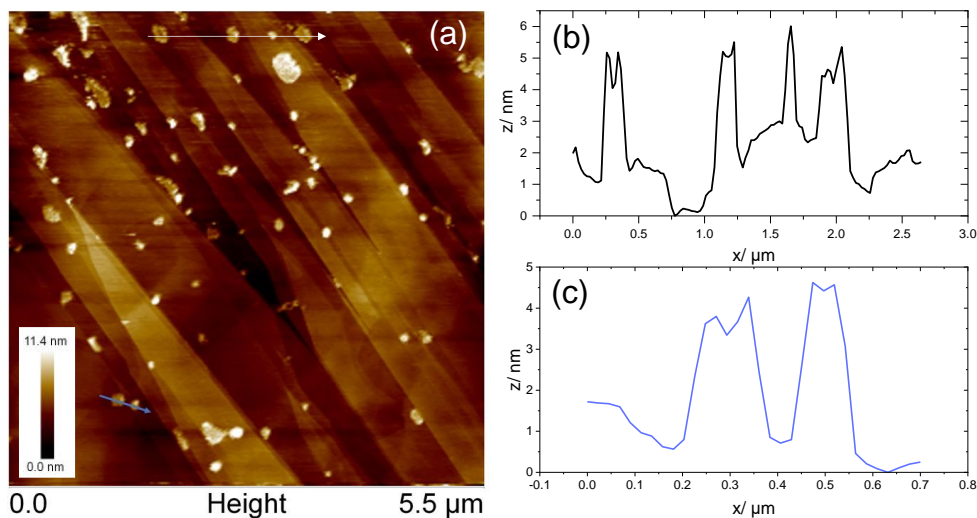


Figure 2.3. Representative tapping mode AFM image (a) and corresponding cross-section analysis (b-c) of two regions (arrows) of BE-CsPbBr₃ nanoplatelet domains drop cast onto HOPG.

The thickness was also probed by atomic force microscopy (AFM). Figure 2.3 shows a typical AFM image of BE-CsPbBr₃ platelets dropcast from a toluene dispersion onto a HOPG grid. At

the resolution shown, domains consisting of many platelets are imaged. Importantly, sharp edges can be observed, and cross-section analysis reveals overall thickness profiles of the domains (Fig. 2.3). The heights measured vary slightly, from 3-5 nm, which are thinner than the ML estimate from the main absorption band above, suggesting that thinner platelets were sampled. We note that some products dispersions showed significant aggregation, and after drop casting, domains revealed stacks or clusters of platelets that revealed larger heights. To understand this, scanning electron microscopy (SEM) was used to image those dropcast substrates. Figure 2.5 shows the platelets and the 2D morphology, as well as grouped discrete aggregates, which were difficult to separate, and was attributed to either residue BE in the purified product, or the result of excess purification steps, as described below.

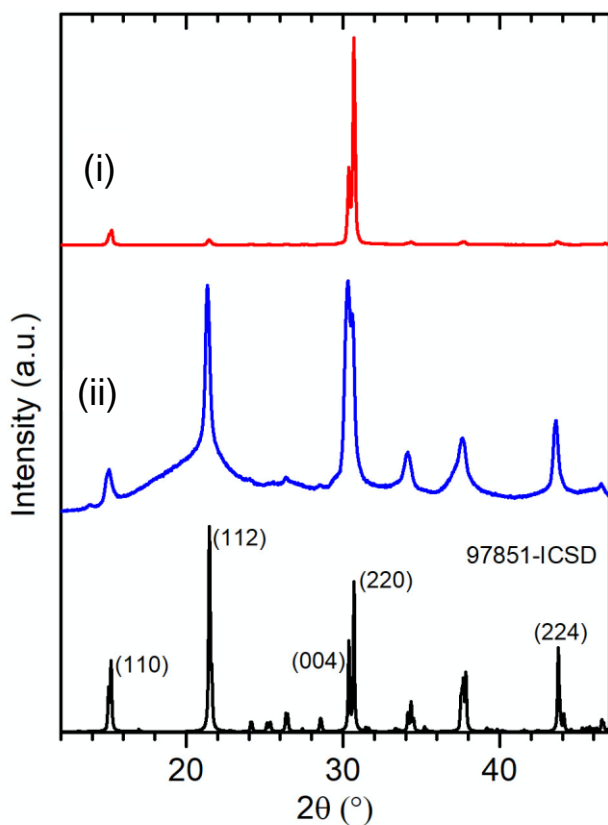


Figure 2.4. Representative powder XRD of BE-CsPbBr₃ (i) and ODE-CsPbBr₃ products (ii), as compared to an orthorhombic CsPbBr₃ standard (97851-ICSD).

The crystalline nature of the CsPbBr₃ products were studied by powder X-ray diffraction (XRD). Figure 2.4 shows the XRD analysis of the BE- (i) and ODE-CsPbBr₃ (ii), as compared to an orthorhombic CsPbBr₃ bulk standard. Both products index with the orthorhombic standard with minimal variation to Bragg angles, but intensity ratios differed, as did the extent of Scherrer broadening. For example, the BE-CsPbBr₃ (i) showed pronounced preferred orientation of the planes diffracting at $2\theta = 30.4$ and 30.7° , which correspond to (004) and (220) of the crystal. Clearly, the intensities do not match the standard, and suggest not only that each platelet grows in the same orientation, but that each platelet is highly crystalline. It's important to note that preferred orientation in XRD can be a result of crystal growth, as well as an artifact produced by the way a sample self-assembles during drying, as well as by substrate type and sample-to-substrate interactions.¹⁵⁷ We suspect that each of these factors influence the XRD shown here. The samples were prepared via drop-casting from a concentrated solution, and we assume they form into the irregular clusters shown by SEM (Fig. 2.5). Nonetheless, a number of control experiments were performed to better understand the peak intensities and the origin of the preferred orientation. To test whether the intensity ratios could be an artifact of platelet drying on the XRD substrate, samples that were both drop cast from solution, and from dried powders, each of which showed similar intensities.

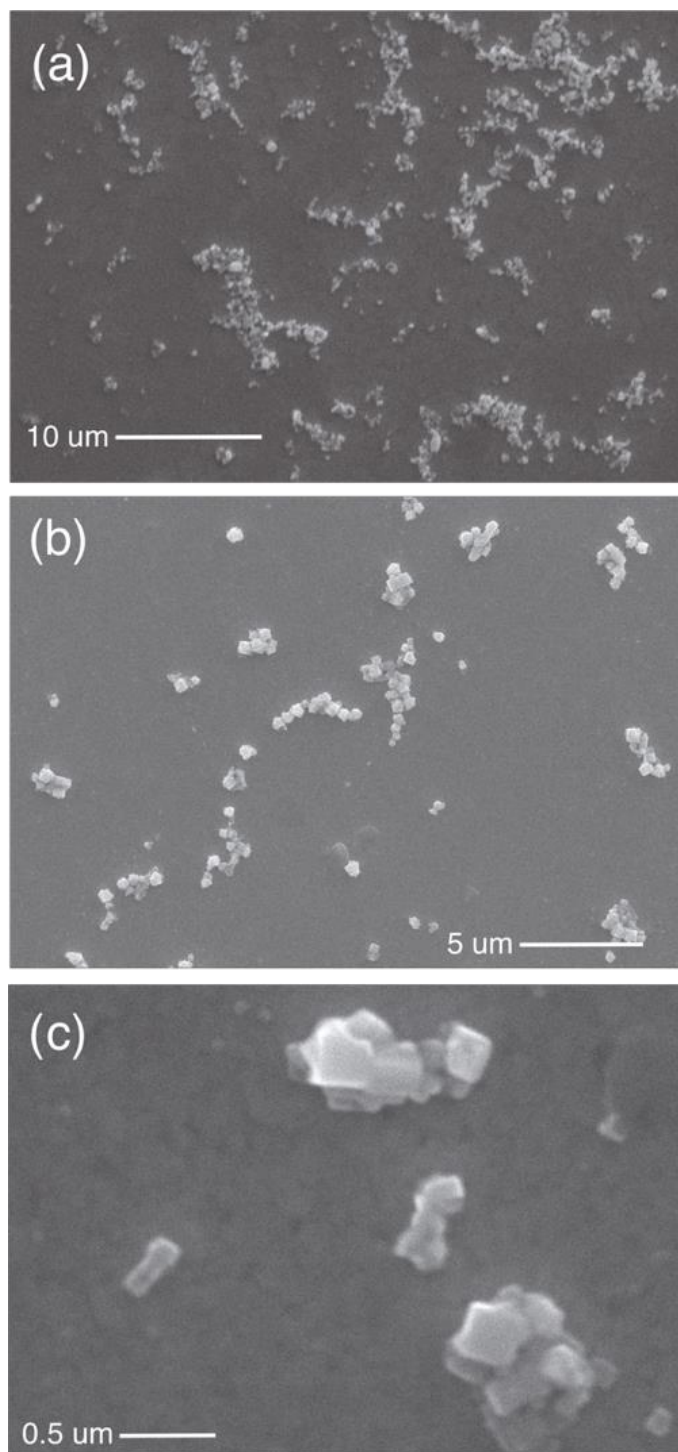


Figure 2.5. Representative SEM micrographs of purified BE-CsPbBr₃ dropcast onto HOPG and imaged at increasing magnifications (a-c).

In another control, a concentrated carbon black slurry with colloidal carbon (~20 nm) was added to a toluene solution of purified BE-CsPbBr₃, sonicated, and dropcast, with the aim of using the carbon to inhibit platelet stacking during drying. This however resulted in similar XRD signatures (Fig. 2.6), suggesting that crystal orientation plays at least some role, and that growth occurs in the (004) and (220) directions of the platelets, of which (220) can be indexed to the longer dimension of the platelet. The thickness of the platelets, and thus the planes of atoms in that direction, are outweighed in terms of number, and have lower Bragg intensities. The ODE-CsPbBr₃ on the other hand (ii), had intensity ratios consistent with that of bulk, as well as broadening consistent with the smaller dimensions.

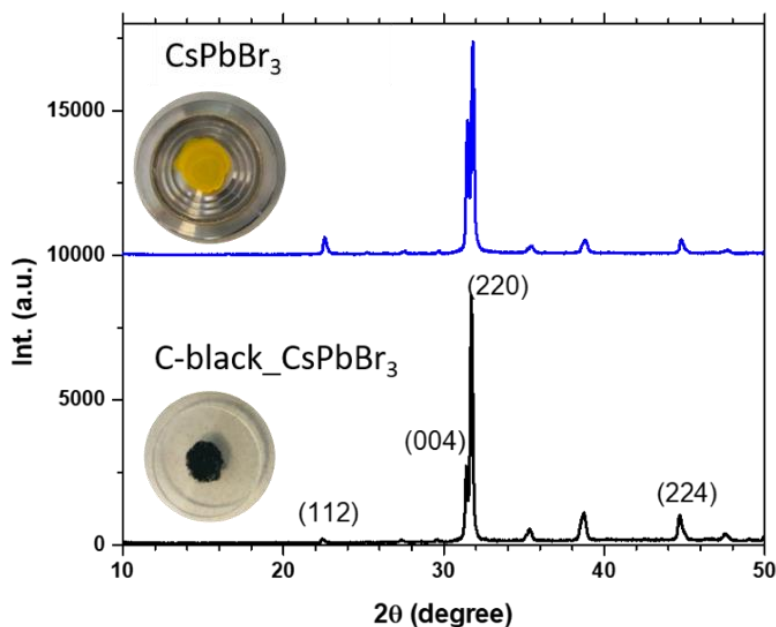


Figure 2.6. Control experiment XRD results comparing the purified BE-CsPbBr₃ nanoplatelets prepared (top) and same nanoplatelets with 50 μ L of 3 g/L carbon black added and sonicated before drop casting (bottom), testing whether or not the nanoplatelets stacked on the XRD holder, which was found to not be the case, due the similarity of the two results. Orthorhombic reference planes shown for illustration only.

The halide concentration of the platelets could also be fine-tuned, either by introducing iodide (I) into the synthetic solutions, or via halide exchange (HE), resulting in BE-CsPbBr_{3-x}I_x. Here, we

focused on only the BE solvent, since there are numerous examples of halide control in ODE-based products.¹⁰³ Figure 2.7 shows the PL for BE-CsPbBr_{3-x}I_x, synthesized by varying the [Br⁻]:[I⁻] feed ratio, with the corresponding XRD shown in Figure 2.8. The XRD signatures were consistent with those platelet morphologies shown above and increased I-rich content is indicated by shifts in 2 θ . Products formed at low I⁻ concentrations showed the platelet like preferred orientation, however this was lost at high I⁻ content.

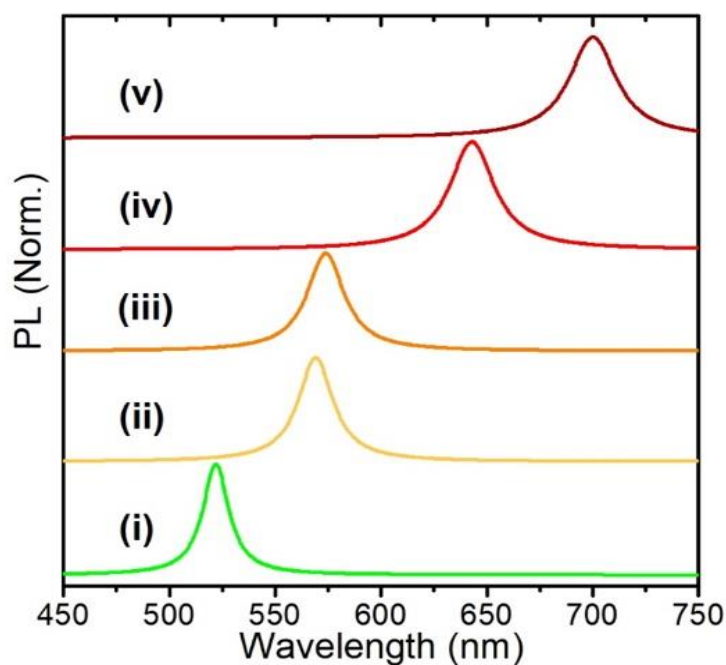


Figure 2.7. PL emission results of BE-CsPbBr_{3-x}I_x formed via the one-pot MWI heating (160 °C) synthesis using increasing concentrations of [PbI_n]²⁻ⁿ (i-v) complexed with BE and OAm.

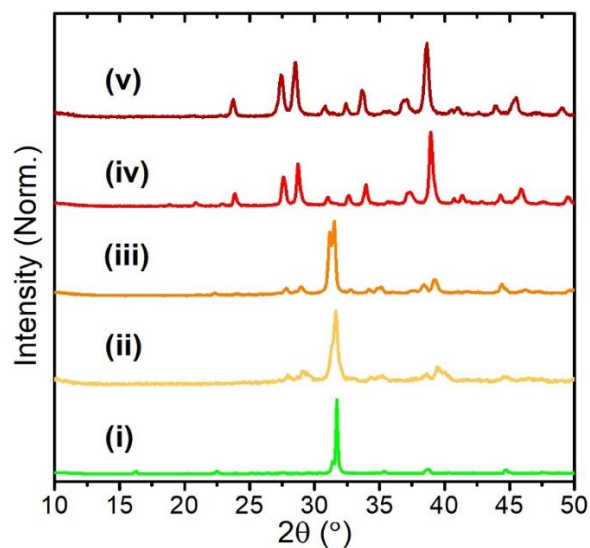


Figure 2.8. XRD results of BE-CsPbBr_{3-x}I_x formed via the one-pot MWI heating (160 °C) synthesis using increasing concentrations of [PbI_n]²⁻ⁿ (i-v) complexed with BE and OAm.

Alternatively, HE could be used to transform the BE-CsPbBr₃ via addition of I⁻ rich precursors¹⁰³ or small organohalide molecules.^{24,109} Using a protocol recently developed in our lab,¹⁰⁸ we found that the BE-CsPbBr₃ platelets could undergo HE without disrupting the crystal structure, and allowed for a broader control of composition than direct synthesis (Fig. 2.9). A more detailed study of the synthesis of mixed halides and of halide exchange in BE-CsPbBr₃ are beyond the scope of this paper and will be reported elsewhere.

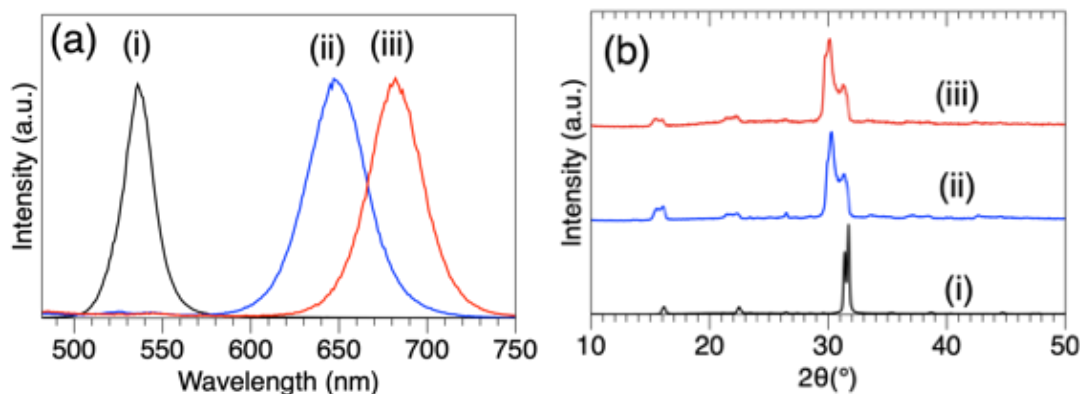


Figure 2.9. PL emission (a) and XRD (b) of BE-CsPbBr₃ nanoplatelets before (i), and after halide exchange with two consecutive washing steps with OAm-PbI₂ (ii-iii) following our recent work.¹

The novel component of this study is understanding the role of BE in the formation of CsPbBr₃, and we next prepared BE-CsPbBr₃ not with MWI heating, but and instead via hot-injection. In contrast to MWI based heating, in which all precursors are in ‘one-pot’ and growth is facilitated or activated by heating, ‘hot-injection’ introduces the final precursor at an elevated temperature, inducing burst nucleation and growth of what is typically a smaller and more monodispersed product. Figure 2.10 shows a set of TEM micrographs for BE-CsPbBr₃ products collected after hot injection and ~1 min annealing at 140 °C (a-c), and after annealing for 30 min (d). One observation made after synthesis was that the product had soluble and insoluble fractions after 1 min. A TEM of the soluble portion is shown in Figure 2.10a, with small square crystals with edge lengths of $l = 6.8 \pm 1.1$ nm visible. The insoluble portion (5b-c) shows larger square platelets with edge lengths of $l = 11.1 \pm 3.5$ nm. Both fractions showed smaller clusters or nuclei with diameters of $d \sim 3.5$ nm and very uniform inter-cluster distances, see arrow. Based on the optical signature, which showed a band edge absorption at 500 (a-c) and 510 nm (d), these had thicknesses of ~2 ML, respectively, making them much thinner than the MWI based products.

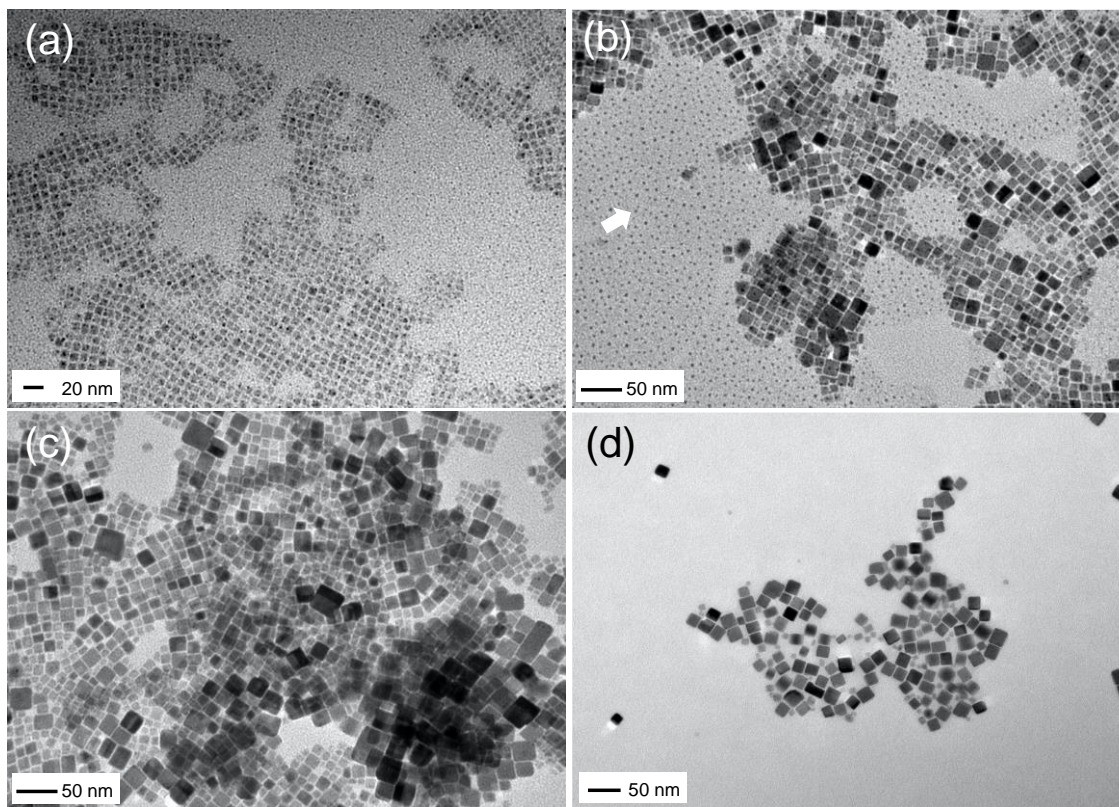


Figure 2.10. (a-d) Representative TEM micrographs of BE-CsPbBr₃ products via hot-injection in BE. Samples collected from soluble (a, $l = 6.8 \pm 1.1$ nm) and non-soluble fractions (b-c, $l = 11.1 \pm 3.5$ nm) of the synthesis solution after centrifugation. Early reaction times show a high concentration of small clusters (arrow, $d \sim 3.5$ nm). The sole non-soluble product after 30 min annealing (d, $l_1 = 17.4 \pm 2.6$ nm, $l_2 = 10.4 \pm 1.6$ nm).

Figure 2.11 shows the powder XRD for BE-CsPbBr₃ soluble (i) and insoluble (ii) products from hot-injection, as compared to ODE-CsPbBr₃ (iii). Compared to the MWI BE-CsPbBr₃ products (Fig. 2.10), these showed more cubic crystal characteristics, with the insoluble products (ii) showing some preferred orientation. The ODE-CsPbBr₃ similarly showed cubic similarities, but with slight 2θ shifts that may suggest some orthorhombic features.

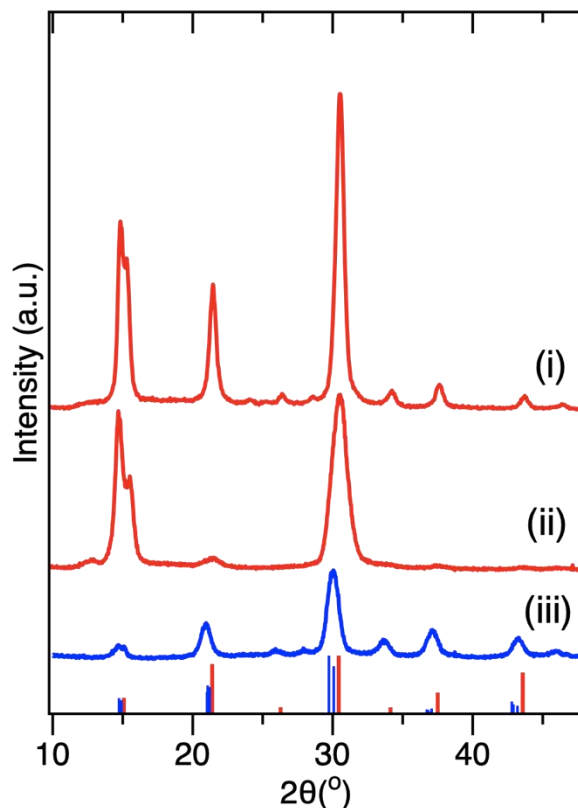


Figure 2.11. Representative powder XRD of BE-CsPbBr₃ hot-injection products for soluble (i), and insoluble (ii) fractions and ODE-CsPbBr₃ (iii) after ~1 min annealing. Reference patterns for cubic (1533063-COD, red) and orthorhombic CsPbBr₃ (97851-ICSD, blue).

We hypothesize that the reason why BE and ODE produce different morphologies is due to the different fractions of precursor types at the time of nucleation, as well the affinity of the solvent to Pb²⁺. Figure 2.12 shows the electronic absorption of PbBr₂ solid dissolved in BE (i) and ODE (iv), and mixtures of BE+OAm+OAc (ii), as well as ODE+OAm+OAc (iii). The absorptions observed are categorized broadly as exfoliated PbBr₂ solids, which may be two dimensional in nature,¹⁵⁴ and multiple PbBr_{*n*}^{2-*n*} lead plumbate complexes which are often defined as PbBr₆²⁻, PbBr₃⁻, and PbBr₄²⁻.^{153,155} Comparing (i) to (iv) reveals that BE is more effective at dissolving PbBr₂ to PbBr_{*n*}^{2-*n*} than ODE. This was also physically observed in the experiment, where BE dissolved the PbBr₂ salt with less visible solids than ODE, in which a high percentage of

insoluble salt was still observed. Secondly, the addition of OAm and OAc further dissolves the solids in the case of ODE and shifts the absorption wavelengths in BE. Both solvent plus ligand mixtures show high concentrations of PbBr_n^{2-n} , likely the result of ligand coordination to Pb^{2+} and substitution of one or more bromides (see below), with ODE+OAm+OAc still showing a considerable percentage of insoluble PbBr_2 . Whether or not this solid PbBr_2 is incorporated into forming the nano CsPbBr_3 is likely dependent on the effect of the synthetic temperature on dissolution equilibrium.

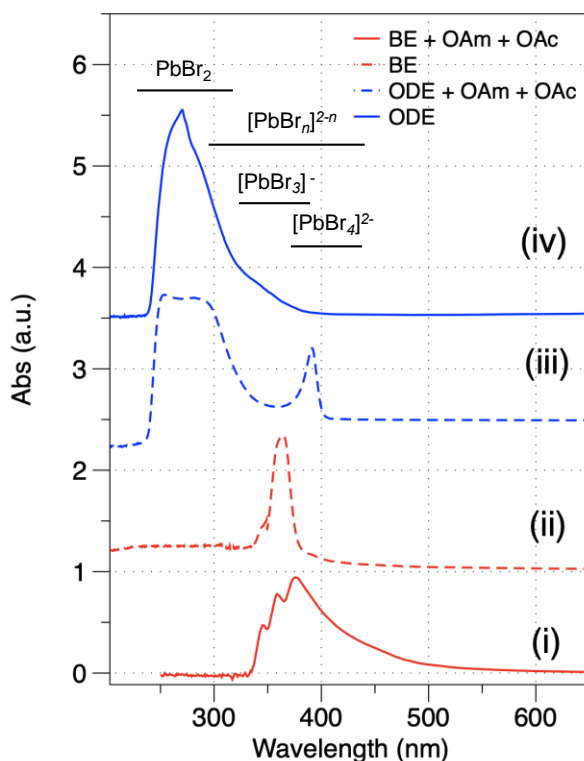


Figure 2.12. The UV-vis of $[\text{PbBr}_n]^{2-n}$ formed via PbBr_2 dissolved in BE (i), BE+OAc+OAm (ii), ODE+OAc+OAm (iii), and ODE (iv) at 140 °C under vacuum for 1h and then cooled to room temperature. Approximate absorption regions for different $[\text{PbBr}_n]^{2-n}$ complexes are shown. Spectral ranges used vary due to solvent absorption.

This insight suggests that BE coordinates and solvates PbBr_2 better than ODE, which is understandable considering its π -rich nature. Researchers have studied the solvent effect of perovskite formation previously, especially as it relates to thin film formations of methyl ammonium halides (MAPbX_3) using polar solvents.⁶⁹ And, we note that BE has been used in nanoparticle synthesis before, especially in the recent synthesis of QD heterostructured libraries.^{158,159} By using a competitive assay between solvents and halides, a Benesi-Hildebrand analysis can be used to approximate coordination strength by way of estimating equilibrium constant (K) and Guttmann donor number (DN), which measures PbBr_n^{2-n} concentration and type in the presence of excess halides by way of UV-vis.^{69,149,153,160} For instance, Loo and co-workers compared solvent dielectric constants and DN with either crystal growth or thin-film growth mechanisms, and showed that while ϵ values did not predict growth, that $\text{DN} > 15$ consistently resulted in thin film growth, whereas higher numbers consistently showed crystal growth.⁶⁹ Thus, higher DN solvents, typical polar and strong Lewis bases, coordinate favorably with Pb^{2+} , resulting in PbBr_n^{2-n} with higher n , resulting in more crystal growth (ideal building blocks), whereas $\text{DN} < 15$, coordinate weakly with Pb^{2+} , resulting in lower n , and more amorphous or thin-film growth.⁶⁹ To date, most analysis is compared to polar solvents, like DMF and DMSO, both of which bind strongly to Pb^{2+} and decrease plumbate equilibrium.^{69,149,153} Both BE and ODE are considerably less polar than many of these solvents used for perovskite growth. Figure 3.8 shows a Benesi-Hildebrand assay used to compare BE and ODE, to DMF, where PbI_2 and MAI were used in place of PbBr_2 and MABr. Both assays resulted in equilibrium (K) values comparable to other non-coordinating solvents, where $K_{\text{BE}} \sim 74 \text{ M}^{-1}$ and $K_{\text{ODE}} \sim 84 \text{ M}^{-1}$, indicating that BE binds stronger to PbBr_n^{2-n} than ODE, but much weaker than DMSO ($K_{\text{DMSO}} \sim 10$, Fig. 3.8). Details of this study are reported in chapter 3.

The composition of the final organic capping monolayer of BE-CsPbBr₃ was also studied via Fourier Transform Infrared (FTIR) spectroscopy, and shown in Figure 2.13. Vibrations attributed to BE adsorbed to the CsPbBr₃ interface were consistently observed, further suggesting coordination.

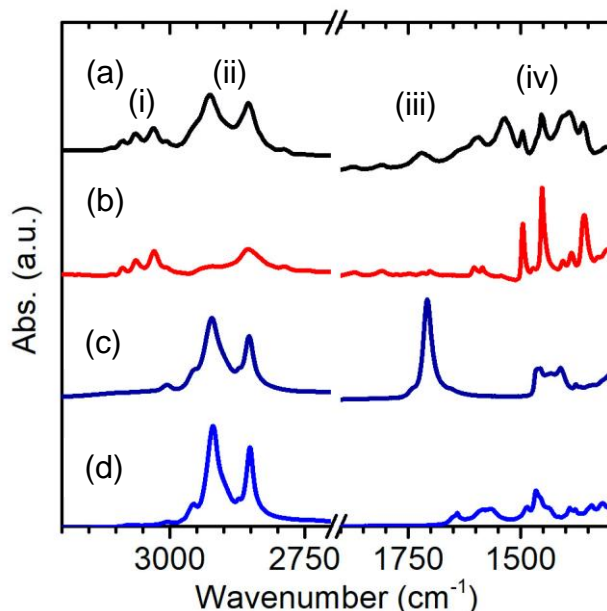


Figure 2.13. FTIR of purified BE-CsPbBr₃ product (a), BE, (b), OAc (c), and OAm (d), and highlighted regions of interest, C-H benzyl rings (i), aliphatic C-H (ii), C=O (iii), and C=C (iv).

While the DN and K values aid in understanding the PbBr₂ dissolution, the cesium oleate precursor is also important, and can have different temperature dependent and stoichiometry related solubility. Control experiments fully solubilizing cesium oleate (Cs⁺-OAc) at room temperature were performed, which used high OAc-to-Cs molar ratios, following a method recently described.¹⁵¹ The products of that control synthesis using MWI had more soluble final products, but the platelet morphology and XRD intensity ratios persisted (Fig. 2.14). This Cs precursor was also used in the hot-injection synthesis described above.

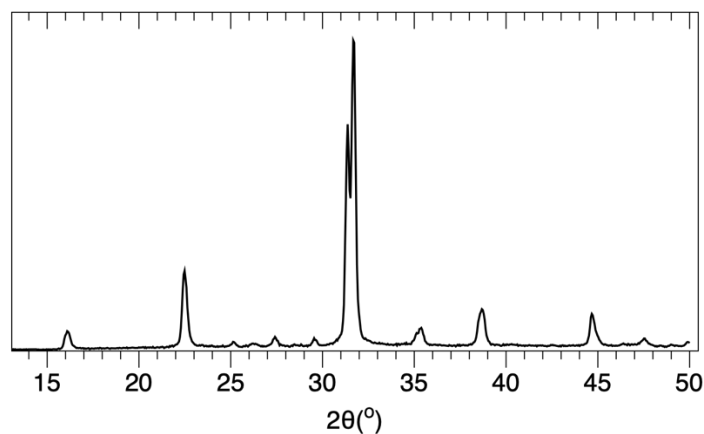


Figure 2.14. XRD results of the BE-CsPbBr₃ nanoplatelet products produced at [OAc]:[Cs⁺] = 5, demonstrating that platelet formation was still observed with more soluble precursors.

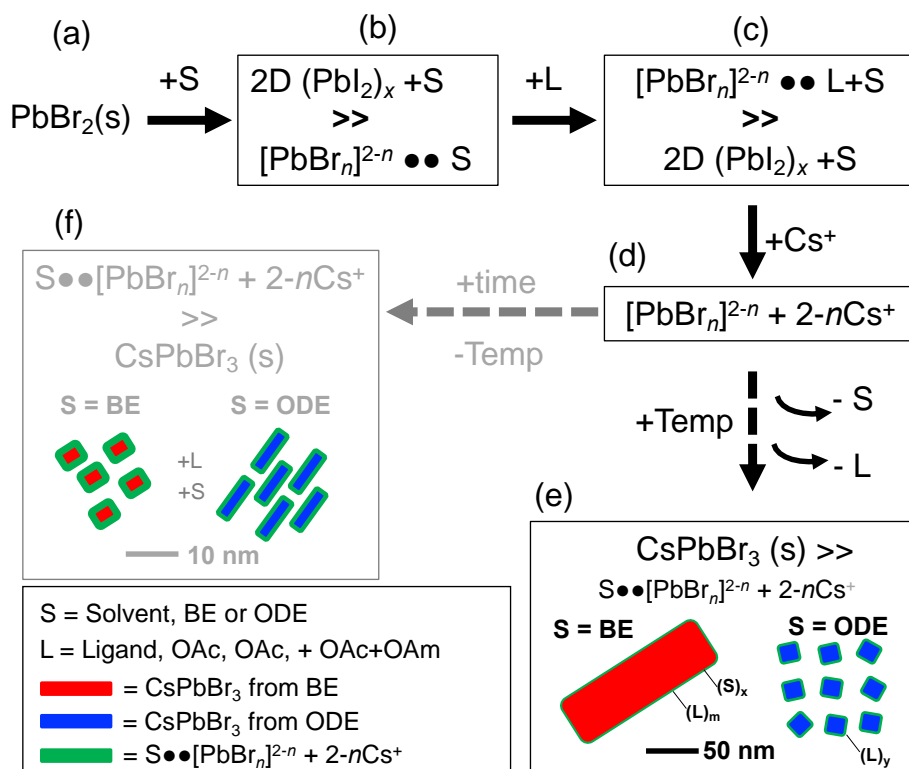


Figure 2.15. An idealized mechanism schematic for the growth of CsPbBr₃ using BE or ODE solvents.

Considering the procedural steps employed in this study, and the findings above, Figure 2.15 idealizes the mechanism for CsPbBr₃ growth. The dissolution of PbBr₂ salt (a) in a solvent (S = BE or ODE) produces two intermediates, two dimensional, exfoliated (PbBr₂)_x solid layers solvated by S, as described recently,¹⁵⁴ and the PbBr_n²⁻ⁿ plumbates of various coordination, such as PbBr₄²⁻, PbBr₃⁻, *etc.*^{155,161} Here, the PbBr_n²⁻ⁿ may have a Br⁻ substituted by S, which is not charged (b). Upon addition of ligands (L = OAm, OAc, OAm+OAc), the equilibrium shifts to forming a higher percentage of PbBr_n²⁻ⁿ afforded by strong L-to-Pb²⁺ coordination (c), which breaks the PbBr₂ into smaller fragments or lower molecular weight polyhedra. Upon the addition of Cs⁺ (d), the PbBr_n²⁻ⁿ polyhedra are electrostatically attracted to one another, forming 2-*n*Cs⁺PbBr_n²⁻ⁿ complexes, but still under the coordination of excess L and S. In this study, steps a-c (precursor preparation) occurs over the course of an hour, whereas step (d) occurs over a few minutes before heating in the case of MWI heating, or within seconds during hot-injection. Upon heating, the 2-*n*Cs⁺PbBr_n²⁻ⁿ complexes loose coordinating S as well as L and are consumed producing CsPbBr₃ perovskite platelets (e). Loss of coordinating solvent during heating is often observed in the formation of perovskite thin films from polar solvents, however in this study, loss of solvent refers to those molecules that were either coordinating to the crystal or separating intermediate plumbates. It is possible that both BE DN numbers likely reside in the thin-film growth regime, as described above, resulting in large mesoscale platelets are observed with prolonged MWI heating and smaller square platelets are formed via quick hot-injection, while ODE produces smaller crystallites of similar sizes for both heating conditions. Also of importance is the temperature used, as it will influence the equilibrium between PbBr_n²⁻ⁿ types and CsPbBr₃ crystallization in the presence of S and L, promoting PbBr_n²⁻ⁿ at lower temperatures.

2.4 Conclusion

Taken together, a synthesis route for CsPbBr₃ nanoplatelets has been described in which choice of non-polar solvents and heating method can be used to control morphology. The findings demonstrate that combining BE, a one-pot mechanism, and MWI heating prove effective at influencing nucleation and growth to the point of forming highly crystalline platelets, with lateral dimensions of 20-500 nm, and relatively thick, ~15 ML, thicknesses. These platelets show preferred orientation in XRD signatures along the (220) and (004) planes. Synthesis via hot-injection with BE also leads to platelets, but a more uniform square shapes, ~17 nm lengths, and ~2 ML thicknesses. On the contrary, use of ODE results in small crystallites, ~10 nm, in both heating approaches. The ability of the solvent, and solvent plus ligand mixtures to dissolve PbBr₂ salt into varied PbBr_{*n*}^{2-*n*} plumbates was studied, and showed that BE is more effective, due in large part to its π -donating character and coordination to Pb²⁺. The compositions of the BE-CsPbBr₃ could be tailored by adding iodine either via synthesis upon addition of PbI_{*n*}^{2-*n*} during synthesis, or via halide exchange.

Chapter 3 – Formation Mechanism in 2D CsPbBr₃ Perovskite Nanoparticles Prepared in Benzyl Ether Using Microwave Irradiation

Abstract

Precise control in morphological design of the CsPbBr₃ nanoparticles has attracted many scientists in materials science. This is particularly important as structural properties of all-inorganic perovskite nanoparticles (NP) dictate their chemical and physical properties and therefore, their application and efficiency in optoelectronic devices. In this chapter, we study the unique approach in the 2D synthesis of CsPbBr₃ nanoplatelets described in chapter 2. In particular, factors affecting the orientational growth of the NPs include incorporation of benzyl ether (BE), microwave irradiation (MWI), and one-pot synthesis. A combination of control studies was performed while UV-Vis absorption, photoluminescence emission and X-Ray Diffraction analysis were employed to monitor optical and structural changes in this study. To understand the influence of BE on nuclei formation and growth of the 2D NPs, Benesi-Hildebrand studies were conducted comparable to the previous studies on iodoplumbate complexation in DMF. The synthesis was also monitored in absence of the MWI at room temperature and using the hot-injection method, to elucidate the one-pot synthesis and MWI effects. Lastly, post-synthesis structural modification was explored via reaction of CsPbBr₃ nanoplatelets with the precursors.

3.1 Introduction

In the last twenty years, perovskites have been the topic of more than 1000 publications per year, holding the second position in the ranking of the materials science topics with the greatest number of publications.¹⁶² In these studies, a great number of synthetic methods have been identified to successfully synthesize all-inorganic perovskite nanoparticles (NP).⁶⁶ On top of that, the effect of pre/post-synthetic parameters on the optical and structural properties of these NPs have been studied, meticulously.^{163,164} These parameters consist of synthesis materials, such as, precursors, passivating ligands, and solvent, and synthesis conditions, such as, temperature, time, and pressure.^{30,65,102,165,166} As demonstrated in several studies as well as chapter 1 of this dissertation, the major technique in changing the NPs' properties is through tuning the composition pre/post-synthesis. For example, during a CsPb(Br/I)₃ NP synthesis, slight changes in the composition ratio of halide precursors result in a different band gap energy, thus, a unique absorption and photoluminescence (PL) emission in the visible region. It is harder to deduce a general rule regarding the influence of the ligands and solvent on the properties of the NPs while a combination of solubility, surface ligand density and solution interactions can determine the fate of the NPs.^{108,167,168} Changing the synthesis condition could also result in various NP morphologies. More often, higher synthesis temperature and longer heat treatments have shown to promote nanocrystal's growth, however, several low temperature studies have also resulted in 1D or 2D nanocrystals. For example, one study showed hot-injection synthesis at a lower temperature of 140 °C favors anisotropic growth in all-inorganic perovskite NPs.⁵⁰

One of the main aspects in controlling the NPs' morphology is the choice between simultaneous nucleation and growth of the NPs, like in hot-injection synthesis or separation of these two steps by a one-pot synthesis. We studied the impact of the one-pot condition in this work by

monitoring the formation of the nuclei and NPs in absent of the heating. Then we focused on the influence of BE in formation of the nuclei and ultimately, the structure of the nanoplatelets.

Researchers have shown that the equilibrium between different iodoplumbate complexes prior to hybrid perovskite synthesis affects the perovskite structure.^{69,149,153,160} A more basic solvent moves the equilibrium by coordinating with the Lewis acid Pb^{2+} center hindering the highly coordinated iodoplumbate formation. In this case, a solvent's basicity can be quantified by the Guttmann's donor number (DN), which is the negative enthalpy value for a 1:1 adduct of Lewis acid SbCl_5 with a Lewis base in 1,2-dichloroethane solvent.¹⁶⁹ For instance, Loo et. al. showed solvents with higher DN (>18 kcal/mol) coordinate favorably with Pb^{2+} , resulting in less interaction with the halides in solution, thereby reducing iodoplumbate complex formation, requisite in MAPbI_3 perovskite synthesis.⁶⁹ These studies inspired us to investigate the iodoplumbate complexation in BE to understand the role of the BE as the solvent in our work.

Another unique factor in the synthesis of CsPbBr_3 nanoplatelets in this study, was the use of microwave irradiation (MWI) to heat up the precursor's mixture and speed up the NPs' growth. While MWI has been utilized in synthesis of various organic and inorganic chemicals, there are few studies regarding its application in perovskite synthesis.^{88,91,99,100,170} More importantly, MWI is particularly applied in synthesis due to its programmable fast and homogeneous heating conditions.^{96,171} In this work, we report on the effect of the MW-assisted synthesis versus the hot-injection technique in 2D growth of the CsPbBr_3 NPs.

We previously, showed that 2D CsPbBr_3 nanoplatelets can be produced in benzyl ether (BE) using a synthetic microwave instrument. In this chapter, we focus on the several factors affecting the synthesis of the CsPbBr_3 nanoplatelets and how each of them might be playing a role in

orientational growth of the NPs. In particular, the influence of three unique features of this method; BE, one-pot synthesis and MWI will be discussed in detail.

3.2 Experimental

3.2.1 Materials

Lead iodide (PbI_2 , 99%), lead bromide (PbBr_2 , 99.99%), cesium carbonate (Cs_2CO_3 , 97%), methyl ammonium iodide (MAI, 98%), oleyl amine (OAm, 70%, technical grade), oleic acid (OAc, 90%), N,N-Dimethylformamide (DMF, anhydrous, 99.8%), 1-octadecene (ODE, 90%), and benzyl ether (BE, 98%) were purchased from Sigma Aldrich and used as received.

3.2.2 Methods

3.2.2.1 Synthesis of CsPbBr_3 Perovskite Nanoplatelets

The CsPbBr_3 nanoplatelets was synthesized according to the method reported in chapter 2. In summary, 0.80 g of cesium carbonate, 2.4 μL OAc and 30 mL BE were stirred at 120 °C under vacuum to prepare the cesium oleate precursor. 0.03 M lead bromide precursor was prepared by adding 2 mL of OAc and 2 mL of OAm to a 20 mL of PbBr_2 suspension in BE at 120 °C under Ar flow. Next, 200 μL of an 85 °C cesium oleate precursor was injected into 3 mL of lead bromide precursor, which was first purged with Ar gas for 5 min at room temperature, followed immediately by microwave irradiation (Discover-SP, CEM Inc.) at 160 °C. NPs were purified 2-3 times by centrifugation (at 10k rpm for 3 minutes, and at 4.4k rpm for 3 minutes) and redispersed in toluene. To monitor the nucleation and growth of the nanoparticles at room temperature, the precursors were prepared and mixed in the same way and stored in ambient condition.

3.2.2.2 Benzyl Ether Coordination - Benesi-Hildebrand Analysis

The Benesi-Hildebrand analysis was performed by first preparing a 0.1 M MAI in BE. Next, MAI aliquots were added to a diluted PbI_2 precursor at a ratio of $[\text{MAI}]:[\text{PbI}_2] = 1\text{-}35$. The resulting iodoplumbate complex formation was monitored by UV-Vis spectroscopy. For the measurements involving DMF solvent, 0.1 M MAI was prepared in either BE or DMF. PbI_2 powder was vigorously stirred in either BE or DMF to make a 5 mM dispersion. MAI was added to a 0.2 mM PbI_2 in aliquots while the ratio of $[\text{MAI}]:[\text{PbI}_2]$ was between 1-350 for analysis in DMF and 1-75 for other reactions. Iodoplumbate complex formation was monitored by UV-Vis absorption measurement of the mixture.

3.2.3 Instrumentation

UV-Visible Absorption Spectrophotometry (UV-Vis)

The UV-Vis absorption spectra were scanned in the range of 300 - 700 nm using a Cary 50 Bio UV-Vis spectrophotometer (Varian Inc.).

Photoluminescence Spectroscopy (PL)

PL emission spectra were recorded using a Cary Eclipse fluorescence spectrophotometer (Varian Inc.). The excitation wavelength was set at 400 nm and excitation and emission slit widths were set at 5 nm.

Powder X-ray Diffraction (XRD)

XRD spectra were produced using D2 PHASER XRD (Bruker) instrument with a Cu-K_α radiation source (1.5406 Å). Samples were prepared by drop-casting purified NPs on a zero-

diffraction quartz holder. Size of the hot-injection produced BE-CsPbBr₃ NPs was estimated using the Scherrer equation as shown in equation 5.

$$D(h,k,l) = \frac{57.3k\lambda}{\beta \cos(\theta)} \quad \text{Equation 5}$$

Where D is the size of the NPs in Å (grain size). k is a dimensionless shape factor with a typical value of 0.9 and λ is the X-ray wavelength (1.5406 Å). β is the full width at half maximum (FWHM) of the broadened peak in degree. and θ is the angle of diffraction at that peak.

Transmission Electron Microscopy (TEM)

First, NPs were diluted in toluene and drop-casted on a carbon coated grid, then solvent was evaporated thoroughly using a Savant Speed Vac Sc110 vacuum. TEM images of the samples were developed using JEM 2100F field emission TEM (JEOL), operated at 200 kV at the Analytical and Diagnostics Laboratory (ADL) at the State University of New York at Binghamton. Particle size distribution was analyzed manually using ImageJ software.

Atomic Force Microscopy (AFM)

AFM imaging was performed on a Digital Instrument Nanoscope IIIa in tapping mode using an E-scanner. Silicon AFM tips (μMasch, HG:NSC14 / AlBs) were used which had a typical resonance frequency of ~160 Hz. Samples were prepared by drop-casting purified NPs on a HOPG substrate, followed by drying in a Savant Speed Vac Sc110 vacuum.

3.3 Results and Discussion

To understand how our MWI heating and reaction conditions affect platelets growth to such large, but thin morphologies we considered three factors. First, how the unique one-pot condition and prolonged synthesis affects the structure, second, whether or not BE molecules inhibit nucleation and growth, as compared to ODE, and lastly, whether the MWI plays a role in the nanoparticles' morphology.

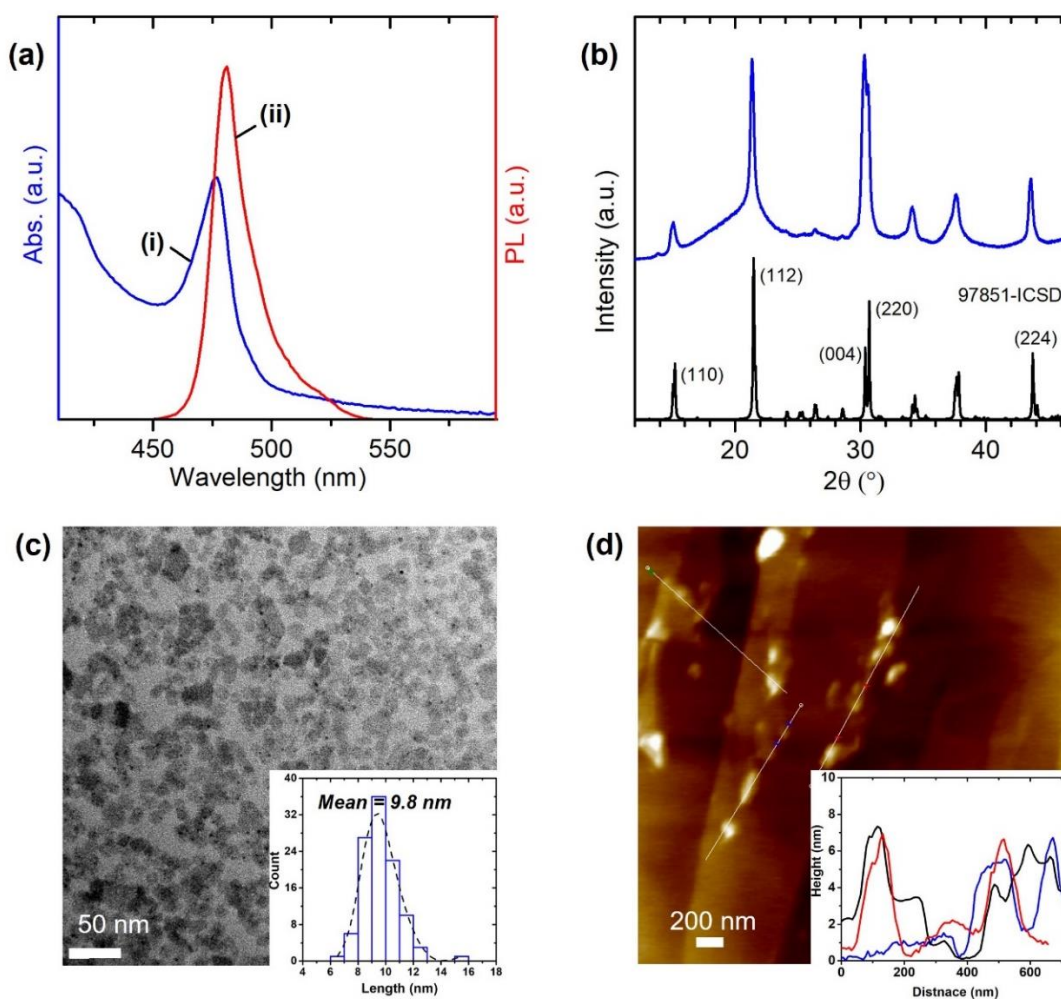


Figure 3.1. Photoluminescence (PL) emission spectrum and structural characterization of CsPbBr₃ NPs prepared in ODE via MWI heating at 160 °C. ODE-CsPbBr₃ absorbance (i) and PL emission (ii) spectra (a), XRD pattern (b) of the ODE-CsPbBr₃ NPs and the orthorhombic perovskite reference (97851-ICSD), TEM micrograph and the corresponding histogram (c), and AFM image and height profile of the ODE-CsPbBr₃ NPs (d).

To illustrate the distinctive role of BE in fabricating the nanoplatelets, CsPbBr₃ NPs were synthesized in ODE under the same condition as the nanoplatelets in BE. The CsPbBr₃ prepared in ODE via MWI at T=160 °C had the characteristics of cubic nanocrystallites typical of OAm- and OAc-derived precursors and ODE solvent. Figure 3.1 shows a set of the absorption/emission (a), XRD (b), TEM (c) and AFM (d) results of ODE-CsPbBr₃. The CsPbBr₃ synthesized in ODE displayed a blue PL emission at ~481 nm with FWHM of 17.0 nm, which is higher in energy than a hot-injection synthesis typically having emission peak at ~510 nm.²⁴ The morphology was largely cubic, with sizes observed by TEM of ~10 nm NPs correlating with our previous hot-injection synthesis.²⁴ Dark marks around the corner of the ODE-CsPbBr₃ NPs in TEM images have been previously linked to the diffusion of Pb²⁺ from the lattice and formation of Pb⁰ metals upon electron beam radiation of TEM.^{86,137,166} The XRD of ODE-CsPbBr₃ compared closely with an orthorhombic CsPbBr₃, while small size of the ODE-CsPbBr₃ NPs caused Scherrer broadening in the diffraction peaks. Contrary to the BE-CsPbBr₃ pattern in figure 2.4, ODE-CsPbBr₃ XRD did not demonstrate the preferential growth. The optical and structural analyses of the ODE-CsPbBr₃ NPs showed that microwave-assisted synthesis in ODE produced blue-emitting perovskite nanocubes which differ from nanoplatelets described in chapter 2. Therefore, the contrast between BE-CsPbBr₃ nanoplatelets and ODE-CsPbBr₃ nanocubes is used to study the mechanism of 2D growth in this chapter.

A unique aspect of the growth can be attributed to the “one-pot” nature of the synthesis, unlike “hot-injection” synthesis where a supersaturated concentration nuclei are formed upon injection of precursors, such as Cs-Oleate. Hot-injection introduces all reactants at once, and under most conditions, nucleation and growth is temperature induced at a later stage. However, owing to the

highly favorable nature of the formation of perovskite crystals, due in large part to a high crystal lattice energy, perovskites can form at room temperature.

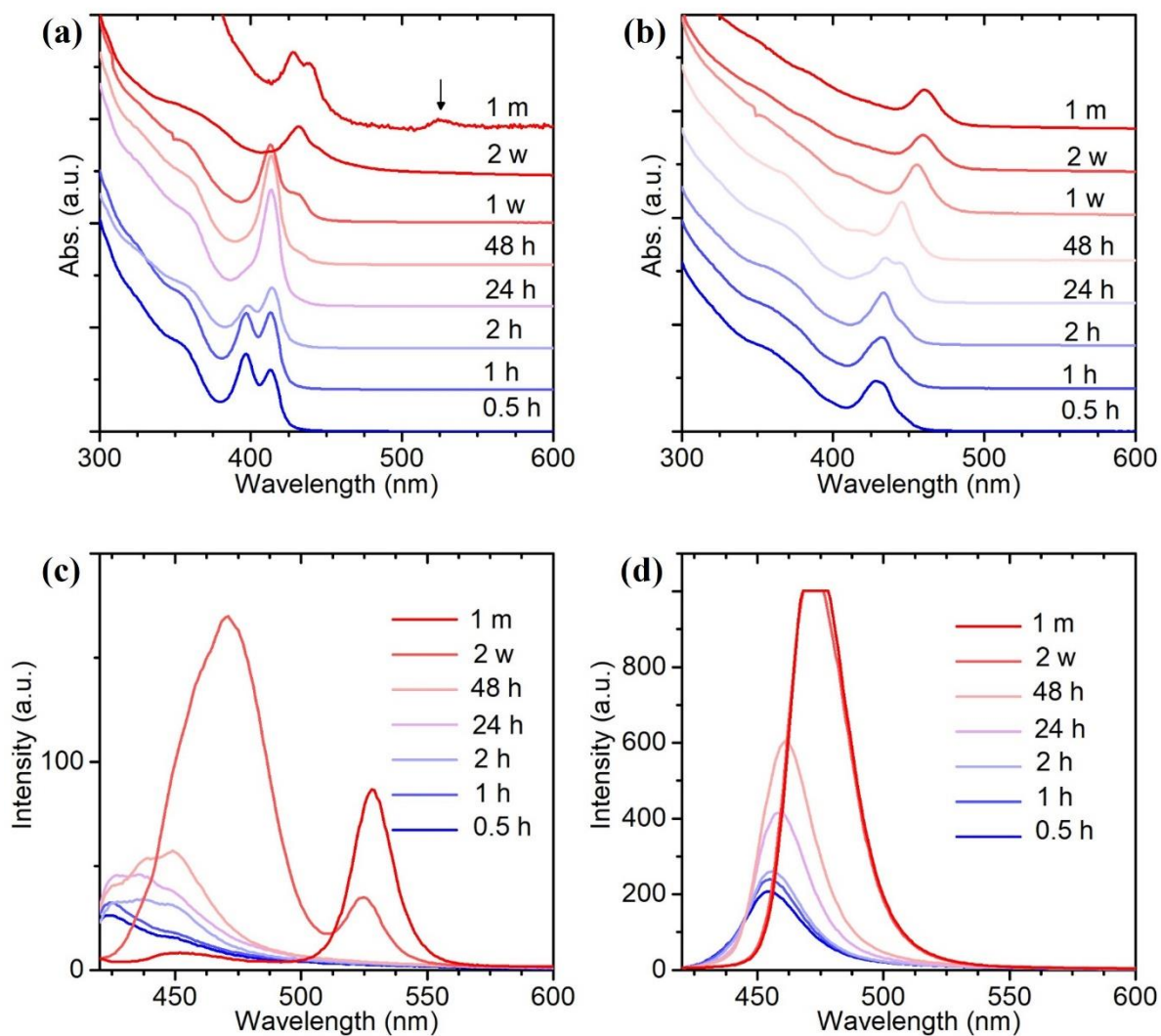


Figure 3.2. Representative UV-Vis and PL spectra of the CsPbBr_3 solution pre-treatment at room temperature collected over one month. Absorption and PL spectra in BE (a, c) and ODE (b, d).

one additional observation during the synthesis was a faint color change if the precursors were mixed long before any MWI heating. We hypothesized that this could have been growth of small CsPbBr₃ nuclei. To probe this, we followed both an ODE and a BE-based reaction mixture at room temperature over extended periods of time using UV-Vis and PL. Figure 3.2 shows the characterization of an increased yellow-orange luminescence, as documented by the broad absorption profile with band-edge of ~ 425 nm, and a broad multi-featured PL between 400-500 nm. This product was difficult to collect and as purified had the consistency of oil, thus, its XRD was featureless at first, suggesting small (<2 nm) CsPbBr₃ clusters, nuclei, or ultra-small nanocrystals. This suggests that these complexes or nuclei are present at the onset of MWI heating and are likely crucial to platelet growth. Both absorbance and PL wavelengths shifted to higher values, over a month. The PL emission changed from a low broad emission to a more defined double-peak emission after one week, and after a month, featured a mono-peak emission at ~ 525 nm, resembling the emission of the MWI-synthesized NPLs. Similarly, the room temperature precursor mixture in ODE showed a trend of redshifted absorbance and PL wavelengths over a month, while absorbing and emitting at lower wavelengths compared to the BE mixture. The lower wavelength/higher band gap could be the result of the formation of smaller NP seeds in ODE, observable in the translucent yellow solution.

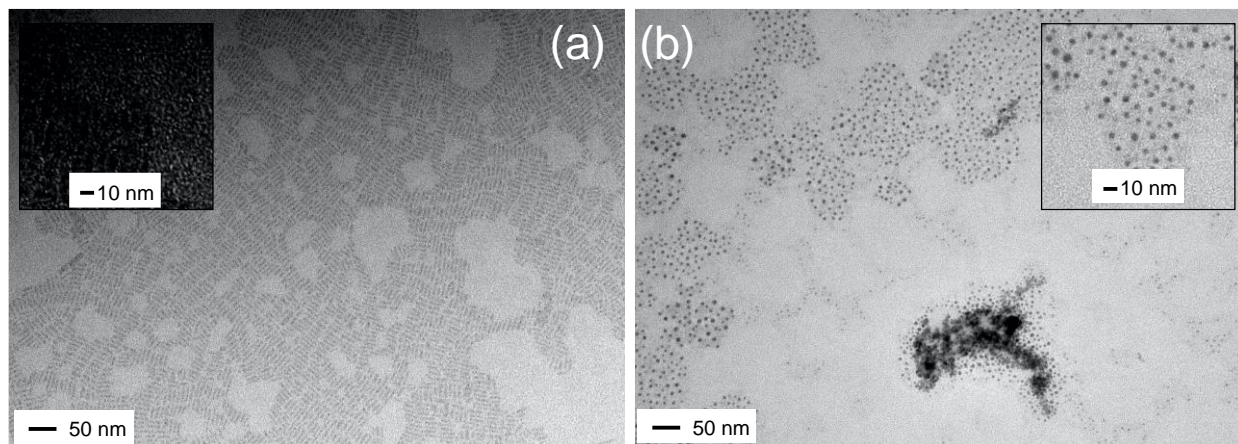


Figure 3.3. Representative TEM micrographs of ODE- (a) and BE-CsPbBr₃ (b) products formed at room temperature after 24 h reaction. Inserts: Enlarged areas within micrographs.

Kinetically, the BE-CsPbBr₃ formed slower and resulted in thinner CsPbBr₃ (Fig. 3.2), where smaller crystallites are formed that have well defined inter-crystal distances, which we attribute to repulsion from coatings of charged PbBr_n^{2-n} at the interface. A TEM image of these is shown in Figure 3.3. The slower kinetics and smaller crystal size ($d \sim 3$ nm) in the case of BE at room temperature again suggests strong coordination to PbBr_n^{2-n} , the release of which is more sensitive to temperature. ODE on the other hand formed uniform rod like structures with lengths < 15 nm. This final point suggests that judicious selection of both solvent as well as modest temperature changes may allow for a wealth of morphologies to be formed and controlled, which is part of our ongoing work and will be reported elsewhere.

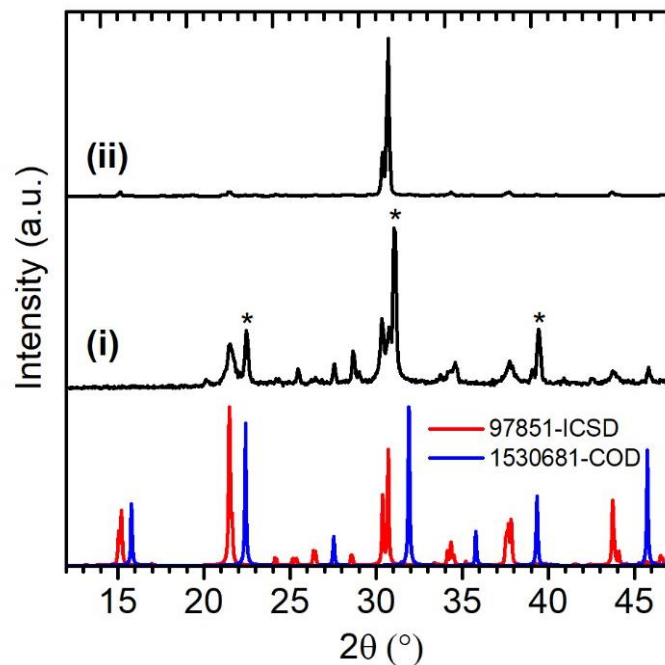


Figure 3.4. XRD of ODE-CsPbBr₃ (i) and BE-CsPbBr₃ (ii) products formed at room temperature over 1.5 months, a cubic CsPbBr₃ reference (1530681-COD) and an orthorhombic CsPbBr₃ reference (97851-ICSD) are shown for comparison.

As shown in figure 3.4, the XRD results of the ODE-CsPbBr₃ (i) and BE-CsPbBr₃ (ii) formed at room temperature over 1.5 months. Of particular interest is the observed preferred orientation in BE-CsPbBr₃ which is similar to that of the MWI samples. Interestingly, the ODE-CsPbBr₃ showed a mixture of orthorhombic and cubic crystal growth.

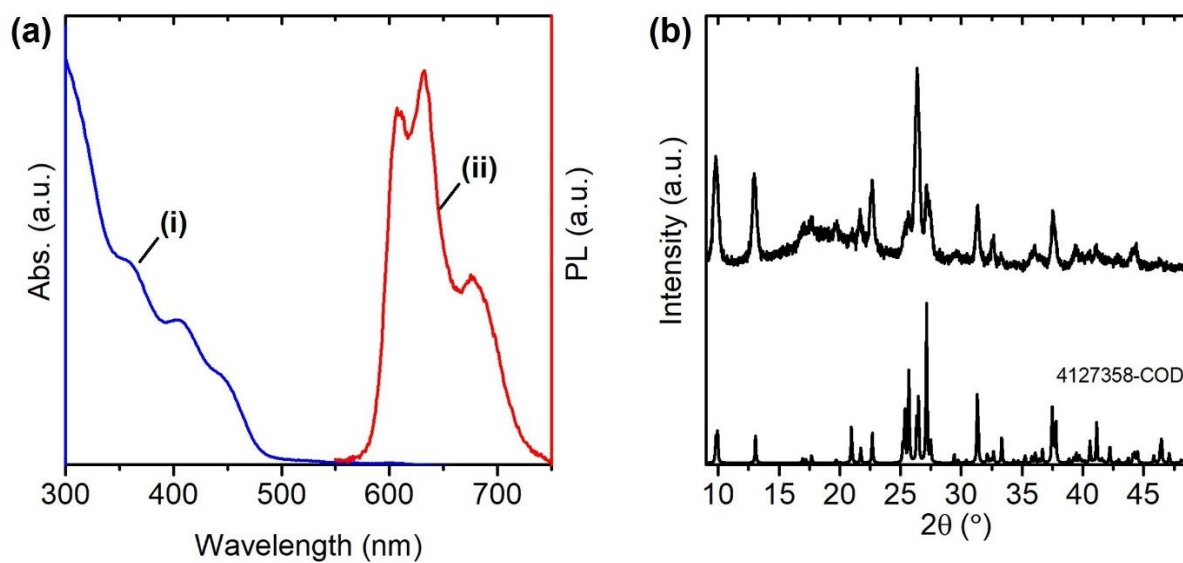


Figure 3.5. UV-Vis absorption (i) and PL emission (ii) spectra (a) of CsPbI₃ synthesized at room temperature in BE. XRD results (b) characterizing the crystal structure of CsPbI₃ nanostructures prepared in BE at room temperature after 24 h with matching standard orthorhombic XRD pattern (4127358-COD).

The absorbance and PL measurements of the Cs-PbI₂ precursor mixture also showed several peaks with an exciton peak of 490 nm and PL peaks from 600-700 nm (figure 3.5). The mixture turned into dark luminescent solution during the first couple of hours, however, it turned into a non-luminescent yellow phase the day after, hence, was not pursued.

The XRD data in figure 3.4 was indicating that even in the absence of a heating treatment, BE favors a 2D growth over the 0D structure of ODE samples. This led us to question whether the BE is interacting with the precursors or the initial nuclei differently. In order to approximate the differences between BE and ODE coordination to the precursors, in particular, halide-plumbate complexes, we performed Benesi-Hildebrand (BH) analysis to compare the equilibrium constant of iodoplumbate complexes.

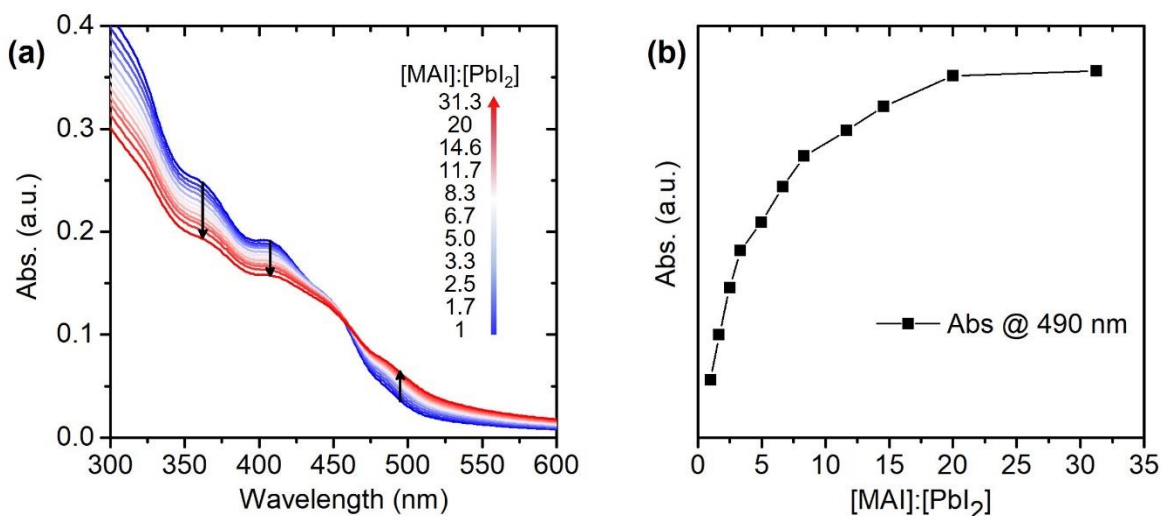


Figure 3.6. Benesi-Hildebrand analysis, UV-Vis absorption (a) of iodoplumbate complexes and absorption at 490 nm (b) as a function of [MAI]:[PbI₂] ratios in a reaction mixture of PbI₂-BE precursor and MAI-BE in toluene.

For this, a model reaction was used to best compare to published results, using iodine analogues, namely PbI₂ and methyl ammonium iodide (MAI). These precursors were dissolved first in ratios of OAm and OAc that mimics precursor synthesis, diluted in toluene to ensure solubility and then aliquots of MAI (prepared in BE) were added. Figure 3.6a shows the resulting UV-Vis, which probes the iodoplumbate cluster formations. Over the course of the reaction between PbI₂-BE and MAI-BE absorption peaks at 364, 410, 450 and 490 nm shows presence of PbI₃⁻, PbI₄²⁻, PbI₅³⁻ and PbI₆⁴⁻ complexes in solution. With increasing [MAI]:[PbI₂] ratios, peak intensity at 364 and 410 nm for PbI₃⁻ and PbI₄²⁻ decreased and PbI₆⁴⁻ peak at 490 nm increased. The isosbestic point in the absorbance is evidence of the equilibrium between species of iodoplumbates.

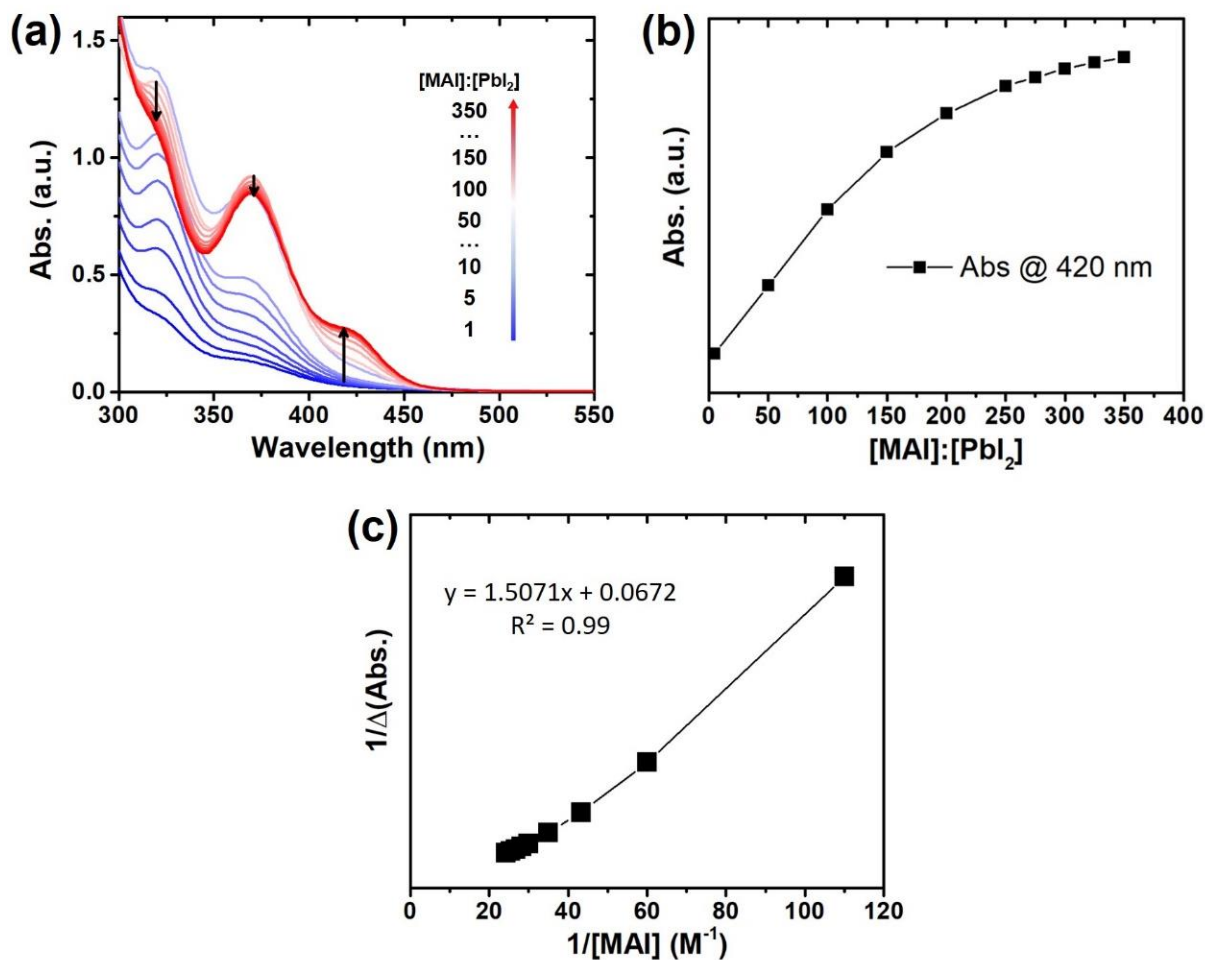
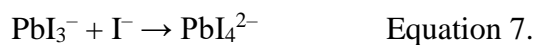


Figure 3.7. Benesi-Hildebrand analysis of iodoplumbate complexes in 0.2 mM PbI_2 with increasing $[\text{MAI}]$ in DMF. In (a) absorption of PbI_2 was monitored with increasing $[\text{MAI}]$, (b) shows absorbance at 420 nm vs $[\text{MAI}]:[\text{PbI}_2]$ ratio, (c) shows Benesi-Hildebrand plot based on the absorption profile at 420 nm.

To demonstrate the difference in our results in BE versus DMF as a conventional solvent for Benesi-Hildebrand analysis of iodoplumbate complexes, we performed the Benesi-Hildebrand analysis in DMF and 50:50 DMF:BE solvents. ODE-DMF was not pursued due to immiscibility of ODE and DMF. First, MAI was added to a 0.2 mM PbI_2 in DMF and absorption was measured as iodoplumbate complexes were formed in the mixture. Our results in figure 3.7 shows with increase in MAI concentration, absorbance at 320, 370 nm, corresponding to PbI_2

and PbI_3^- complexes, increased, simultaneously, until $[\text{MAI}]:[\text{PbI}_2]$ ratio of 150 (blue). After this ratio, peaks at 320 and 370 nm started to decline while PbI_4^{2-} absorbance at 420 nm increased. Absorption at 420 nm was traced over the $[\text{MAI}]:[\text{PbI}_2]$ ratio of 5 to 350 to monitor PbI_4^{2-} formation. Then an equilibrium constant of 0.45 M^{-1} was calculated for PbI_4^{2-} using equation 8 and the line equation of Benesi-Hildebrand plot in figure 3.7c.



$$\frac{1}{A - A_0} = \frac{1}{K} \left(\frac{1}{A_m - A_0} \right) \frac{1}{[\text{MAI}]} + \left(\frac{1}{A_m - A_0} \right) \quad \text{Equation 8.}$$

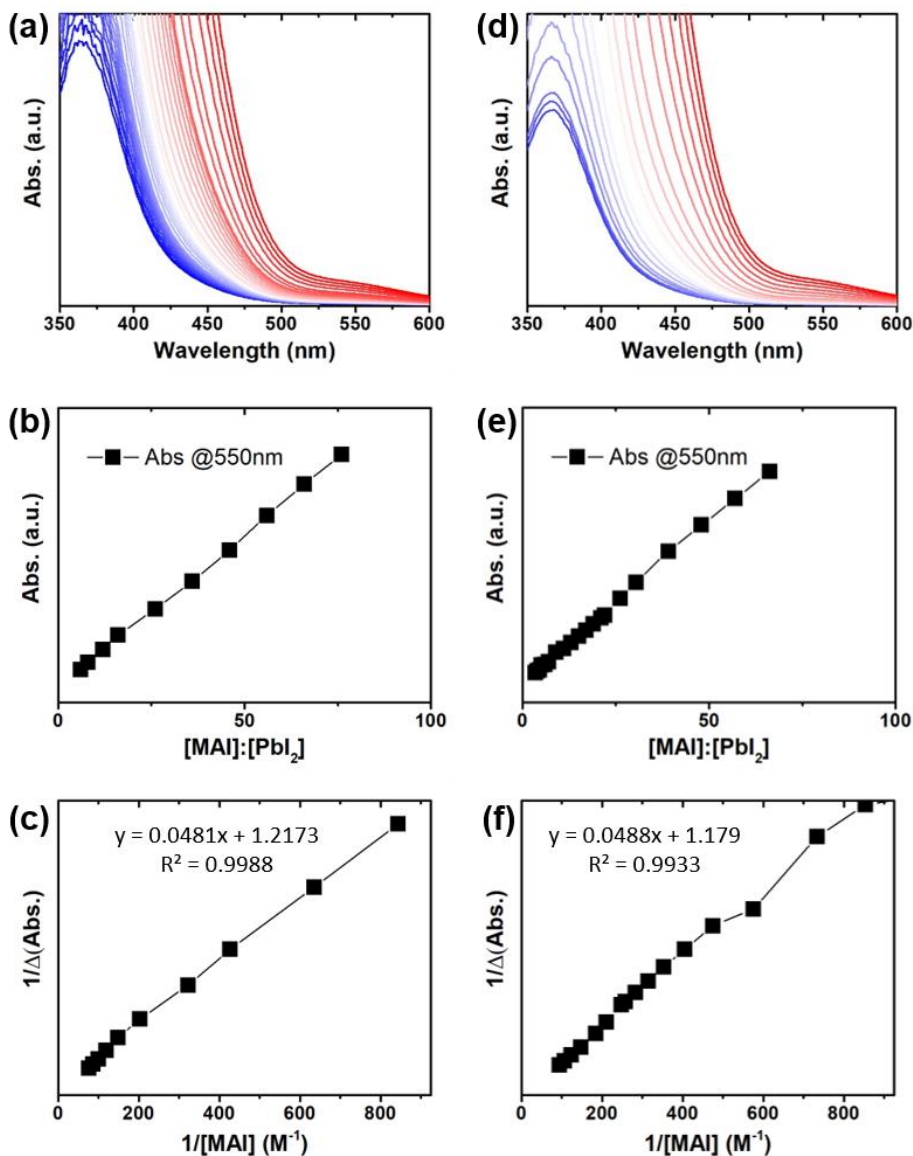


Figure 3.8. Benesi-Hildebrand analysis of iodoplumbate complexes in 0.2 mM PbI₂ with increasing [MAI] in a 50:50 (v/v) BE:DMF solvent mixture. In (a) and (d) absorption of PbI₂ was monitored with increasing [MAI]. (b) and (e) show absorbance at 550 nm versus [MAI]:[PbI₂] ratio. (c) and (f) show Benesi-Hildebrand plot based on the absorption profile at 550nm. For (d), (e) and (f) OAc was added to PbI₂ mixture prior to Benesi-Hildebrand analysis.

To test the effect of BE on the iodoplumbate complexation, MAI was added to a 0.2 mM PbI₂ in a mixture of BE-DMF (50:50 % v) and absorption was monitored as shown in figure 3.8.

Evidently, the precursors experienced a lower solubility without ligands in BE. It should be

noted that iodoplumbate complexes had a low solubility as well and much of the absorption was from the MAI. All the result of this section was acquired under the condition of PbI_2 solution in BE with no ligands. Therefore, these results must not be compared with the original analysis in figure 3.6 of this work and can only be compared in the following discussion as the no-ligand condition is consistent. The BH analysis in figure 3.6 showed increasing absorbance peaks at 370 and 550 nm, (corresponding to PbI_3^- and PbI_4^{2-} species). The equilibrium constant of PbI_4^{2-} in BE-DMF was calculated to be $\sim 25 \text{ M}^{-1}$ using the plot in figure 3.7c and equation 8. We further examined the PbI_4^{2-} equilibrium constant with incorporating OAc prior to MAI addition which did not affect the equilibrium constant, significantly ($k=24 \text{ M}^{-1}$). OAm, however, decreased the initial absorption which was consistent with the increased interaction of Lewis acid Pb^{2+} and basic amine ligand.

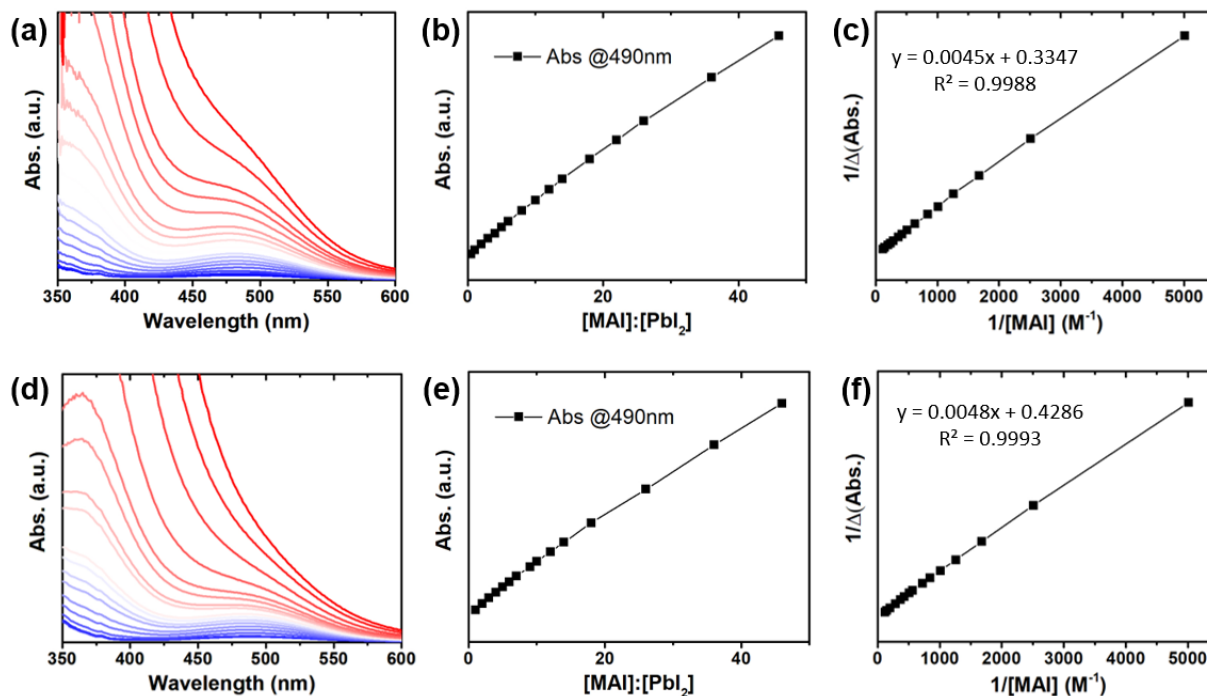


Figure 3.9. Benesi-Hildebrand analysis of iodoplumbate complexes in 0.2 mM PbI_2 with increasing [MAI] in BE shown in (a), (b), and (c) and a 50:50 (v/v) BE:ODE solvent mixture shown in (d), (e), and (f). In (a) and (d) absorption of PbI_2 was monitored with increasing [MAI], (b) and (e) shows absorbance at 490 nm versus [MAI]:[PbI_2] ratio, (c) and (f) shows Benesi-Hildebrand plot based on the absorption profile at 490 nm.

To understand the effect of BE and ODE solvents in our system, we calculated the equilibrium constant of PbI_4^{2-} in BE vs a 50:50 %v mixture of BE:ODE using BH analysis, reported in figure 3.9. Analyzing the absorption peak at 490 nm for the experiment in BE resulted in a value of $\sim 74 \text{ M}^{-1}$ for the equilibrium constant of PbI_4^{2-} . The BH analysis in a solvent mixture of BE:ODE, derived the equation 7 toward PbI_4^{2-} even more with a K of $\sim 86 \text{ M}^{-1}$, showing the higher iodoplumbates formation. The lower equilibrium constant in BE-only experiment shows, a more polar solvent such as BE could hinder the formation of iodoplumbate complexes by coordination, slowing down formation of the perovskite seeds and lead to orientational growth of the nanocrystals.

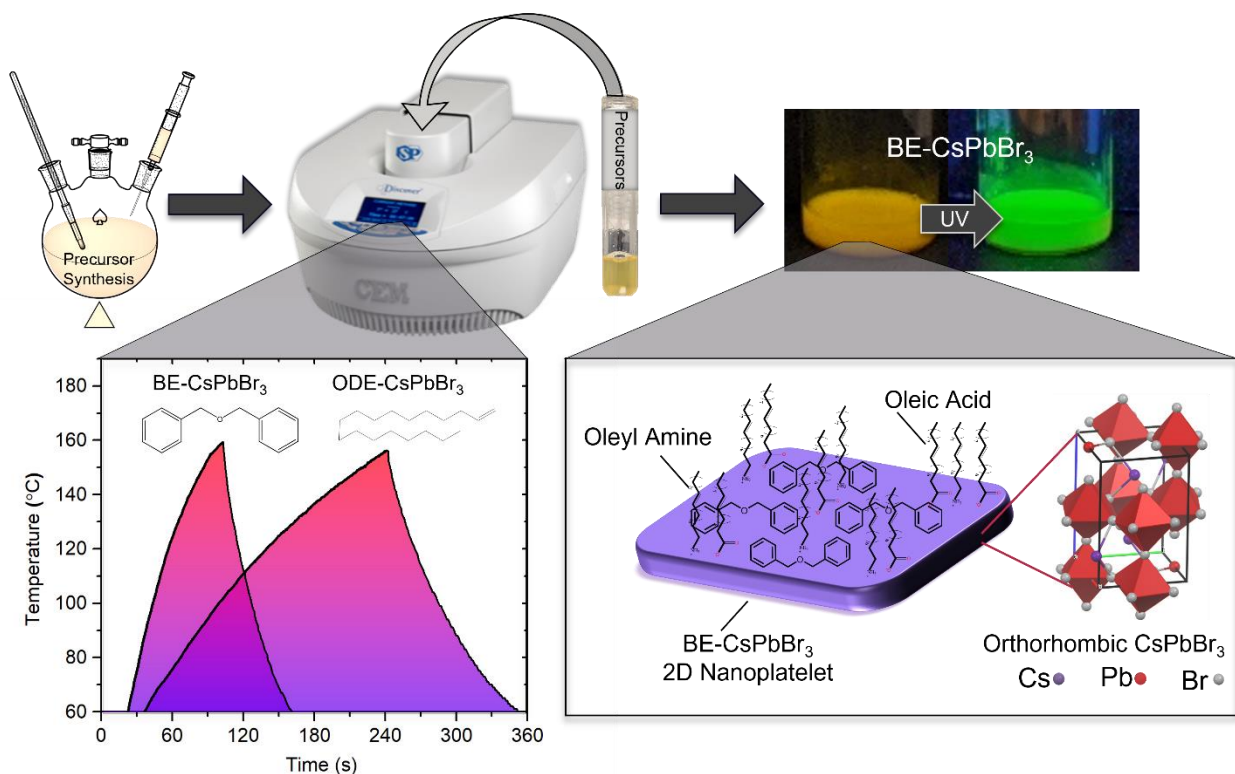


Figure 3.10. Schematic illustration of CsPbBr₃ nanoplatelets synthesis via MWI at 160 °C. First, a Cs-oleate and a PbBr₂-OAM precursor are prepared, then a mixture of them is heated in a microwave synthesizer. A temperature profile of the reaction mixture in BE and ODE is shown. An image of the final BE-CsPbBr₃ products under both ambient and UV light is displayed with an inset showing a schematic representation of a nanoplatelet with an orthorhombic unit cell (unit cell is drawn by Mercury software from a standard perovskite orthorhombic, 97851-ICSD).

Following the conclusion that BE is necessary in the anisotropic crystallization of the nanoplatelets, we investigated if MWI is also playing a role in the matter. Regarding MWI, BE has a higher dielectric constant (3.82) compared to ODE (2.25) owing largely to its higher polarity.¹⁷² Under MWI, BE could also experience intramolecular rotations.⁹⁸ These are manifested by the more rapid absorption of microwave irradiation both a faster overall heating rate, but also a higher local heating rate. This is observed in the heating profiles shown in figure 3.10.

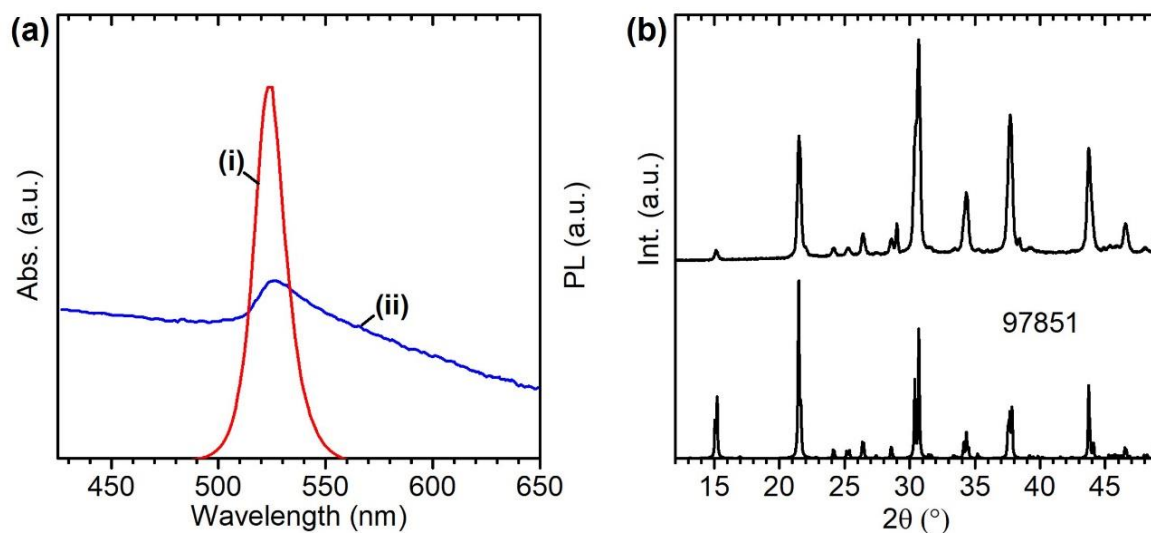


Figure 3.11. Representative photoluminescence emission (i) and absorption (ii) spectra (a) and XRD (b) of BE-CsPbBr₃ nanoparticles prepared via hot-injection synthesis at 160 °C.

To understand the effect of MWI on the structure of the nanocrystals, we synthesized the CsPbBr₃ in BE using a hot-injection method and compared the NPs prepared via MWI and the ones formed in absent of the MWI. In this case, a cesium precursor was injected into a hot 160 °C lead bromide precursor, followed by an immediate quenching of the reaction in an iced-water bath. Both precursors were prepared in BE using the same method and concentration of the ones in the MWI synthesis. Optical absorption and emission of the NPs are shown in figure 3.11. The CsPbBr₃ NPs absorbed the visible light at ~524 nm and emitted green light with a ~524 nm wavelength. Analysis of the XRD pattern of the hot-injection CsPbBr₃ NPs, depicted in figure 3.11, confirmed that these NPs formed in an orthorhombic CsPbBr₃ crystal structure, however, no indication of a 2D structure, similar to the enhanced 220 peak of the nanoplatelets, was apparent in the intensity ratio of the diffraction peaks. In fact, the XRD data resembled the orthorhombic reference more closely, indicating non-anisotropic growth of the nanocrystals. A

calculation of the grain size using the Scherrer equation, yielded an approximate of the NP's dimension ~ 22 nm (equation 5). These results show that simultaneous nucleation and growth in CsPbBr_3 synthesis via hot-injection suppressed the anisotropic crystallization of the NPs, thus, we concluded that MWI is an essential factor in the 2D growth of the CsPbBr_3 nanoplatelets.

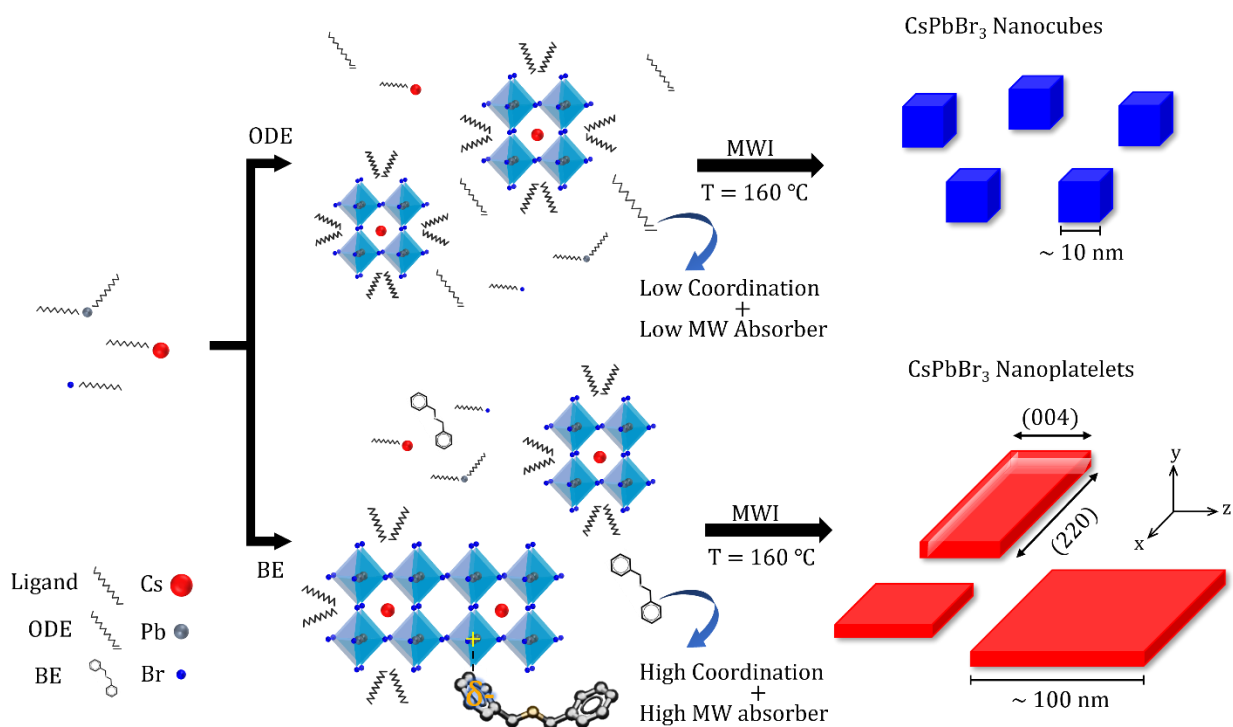


Figure 3.12. Schematic representation of the MWI based synthesis of ODE- CsPbBr_3 nanocubes and BE- CsPbBr_3 nanoplatelets.

Taken together, these results suggest that solvent choice can play a critical role in the nucleation and growth of CsPbBr_3 platelets. Figure 3.12 illustrates an idealized growth mechanism using BE as the solvent. First, nucleation of small CsPbBr_3 nuclei likely form in the time between first mixing reactants and the MWI induced growth. During the subsequent one-pot growth, in which all reactants are present simultaneously, BE coordinates strongly to the growing crystal, likely at

the surface of the platelets, exposing unsaturated Pb^{2+} sites along both the (220) and (004) crystal planes, which facilitates growth in those direction. Considering that control experiments showed that nuclei form at room temperature in both the ODE and BE products, this pre-seeding nucleation could be a factor in platelet growth, but is not likely to be the only factor. Moreover, because no red-shifting in band gap absorption or PL emission in MW-based NPs was observed, as in other nanoplatelet growth mechanisms,^{58,60,61} it is likely that the platelets formed via this approach growth from individual nuclei and not necessarily from the assembly or ripening of smaller platelets. The high crystallinity and preferred orientation of growth in the BE- CsPbBr_3 is evident from the strong XRD diffraction related at the (002) and (004) planes, which serves as a convenient crystallographic probe to product quality. Moreover, these results suggests that future studies and applications that require highly crystalline CsPbBr_3 2D materials, could benefit from these products.

The control experiments showed that both BE and MWI are essential in fabricating the CsPbBr_3 nanoplatelets, but they also suggested that the NP nuclei could grow to a 2D structure in BE at room temperature. Based on these results, we hypothesized that reacting the NP products with the comparable amounts of precursors at room temperature, could force the nanoplatelets to develop their orientational growth even further. To examine this hypothesis, we purified the NPs, redispersed them in BE, and divided the dispersion into three aliquots. Then we added the Cs^+ precursor, PbBr_2 precursor and a mixture of both to each of the aliquots. UV-Vis absorption, PL emission and XRD of the samples were monitored after the addition and the following day.

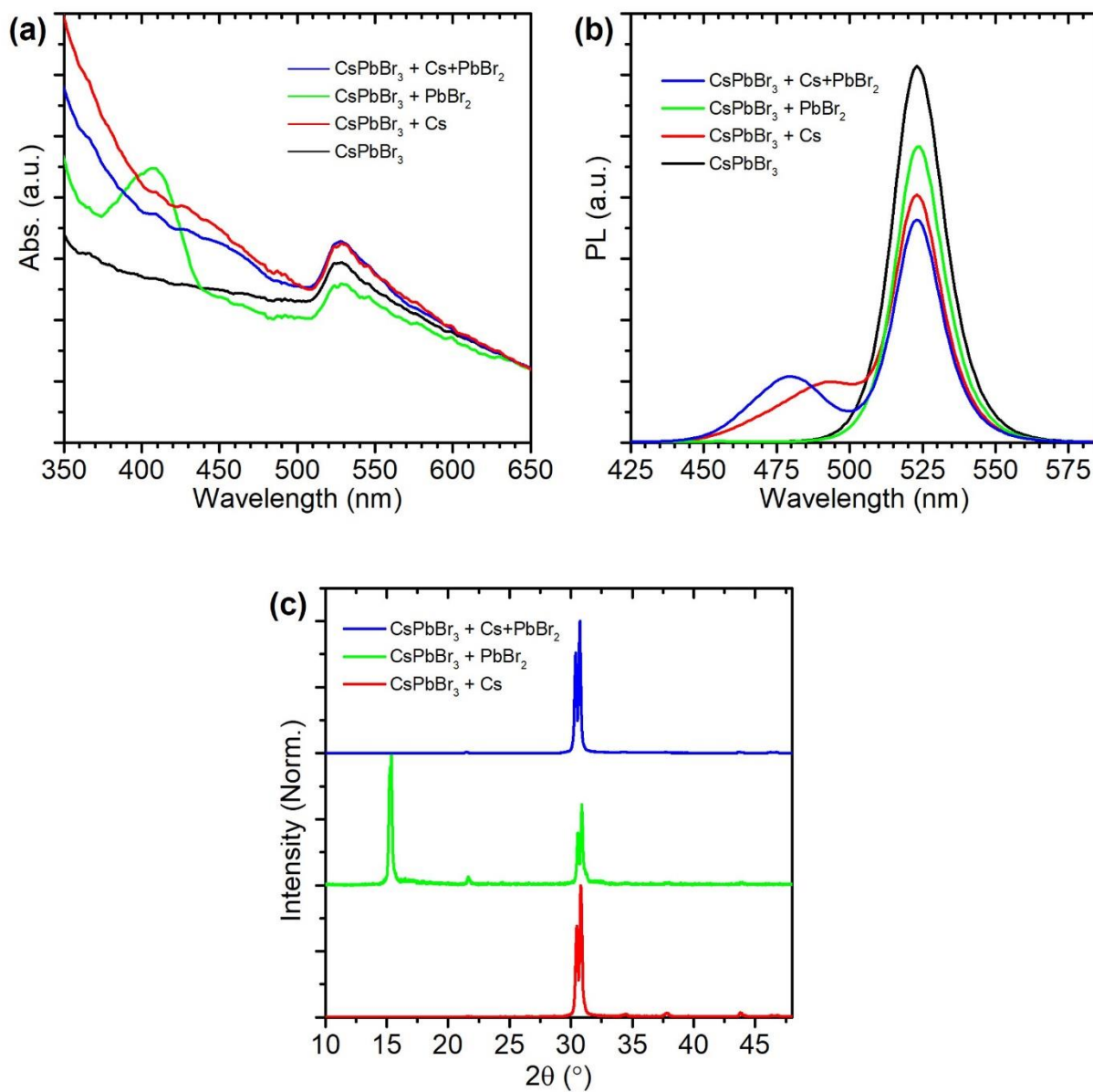


Figure 3.13. Representative UV-Vis absorption (a), PL emission (b) and XRD (c) of the CsPbBr₃ nanoplatelets post-treatment with Cs⁺, PbBr₂ and a mixture of both at room temperature.

In the first experiment, each precursor was measured to be 0.2 times of the mole value of the same species in the batch. Figure 3.13b shows the PL emission after the addition in each case.

Appearance of shoulder peaks for the samples with Cs^+ and Cs-PbBr_2 mixture suggested that different NPs from the control CsPbBr_3 were formed. But, adding PbBr_2 alone did not change the emission pattern. A similar trend was observed in the UV-Vis absorption spectra as well (figure 3.13a). In the case of the precursor-mixture addition, new NPs could form in the sample from the precursors. However, the new PL peak in the sample with 20% more Cs^+ and the lack of it in the one with PbBr_2 implied that the species on the nanoplatelets' surface are probably bromoplumbate complexes which prefer to interact with Cs^+ . This can be explained if the surface species separated from the nanoplatelets to form new NPs with the extra Cs^+ or deposition of the Cs^+ on the surface rendered a breakage in some parts of the nanoplatelets resulting in much smaller NPs. After a week, PL measurements showed a single-peak emission for all the samples. This meant that either the smaller NPs deposited on the nanoplatelets over time due to the Ostwald ripening effect or they dissociated in the solution. The XRD pattern of the three mixtures was also collected after 24 h. The results in figure 3.13c shows the 2D structure is still present after the additions, with an extra PbBr_2 diffraction peak in the second sample.

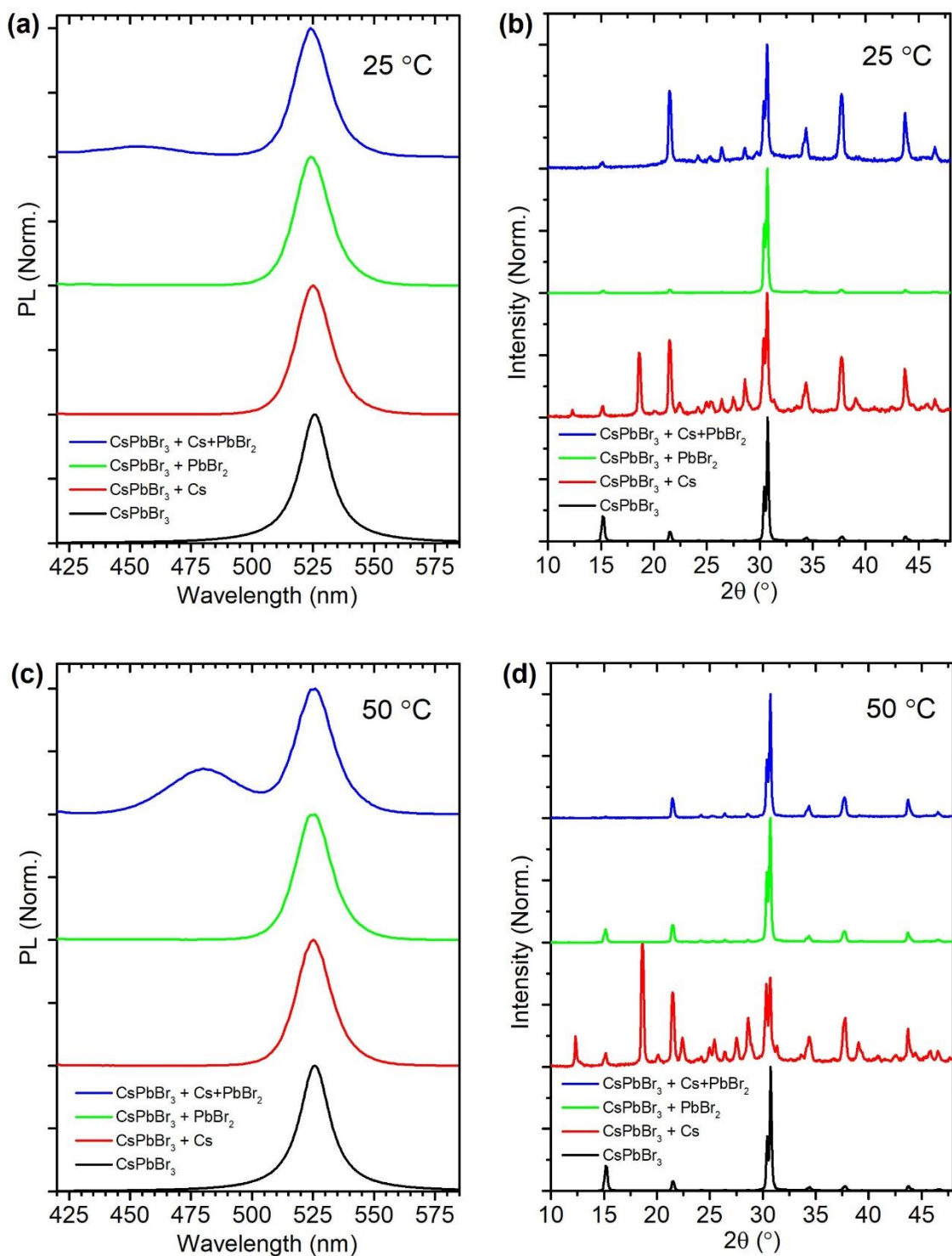


Figure 3.14. PL emission (a, c) and XRD (b, d) spectra of the CsPbBr₃ nanoplatelets post-treatment with Cs⁺, PbBr₂ and a mixture of both at room temperature (a, b) and 50 °C (c, d). NPs and precursors were combined with a 1:1 ratio of moles of that precursor in the NP solution.

For a better understanding of these reactions, we decided to force the reactions forward by increasing the amount of the precursors. For this experiment, each precursor was added with the equal moles of that species in the nanoplatelets aliquots. We also divided each mixture, stirred one set at room temperature and transferred the other set to a shaker at 50 °C. For the 1:1 mole ratio additions, the PL emission only showed new peaks for the addition of the Cs^+ - PbBr_2 mixture which disappeared over time. However, the XRD data revealed more information regarding changes in the nanostructure of the CsPbBr_3 . Figure 3.14b shows the XRD pattern of all the six samples after 24 h along with the control CsPbBr_3 nanoplatelets. The peak intensities in the XRD pattern of samples with the Cs^+ and Cs-PbBr_2 mixture additions did not show the 2D nanostructure signature anymore. Particularly, the Cs^+ addition transformed the highly oriented features of the XRD to diffraction peaks that resembled the standard orthorhombic structure in the intensity as well. However, the PL emission did not differ from the control. These findings suggests that the Cs^+ addition probably broke the long nanoplatelets into smaller NPs but did not bring the length of them to the quantum confinement regime. One other possibility is the self-assembly of the nanoplatelets by intercalating the new Cs^+ layer between them. Similar final PL emission and XRD of the sample with the precursor-mixture addition indicates that Cs^+ is the driving force in this transition. Confirming these hypotheses requires further structural analysis by TEM and AFM microscopies. Overall, it can also be speculated from these experiments that while the CsPbBr_3 nanoplatelets could stack together and make larger structures, the 2D growth could not continue post-synthesis.

3.4 Conclusion

The effect of changing the high-boiling point solvent during the synthesis of CsPbBr₃ nanomaterials while also undergoing MWI-based heating has been described. The findings demonstrate that both BE and MWI heating prove effective at influencing nucleation and growth to the point of forming highly crystalline nanosized platelets. Control experiments suggest that BE does act as a coordinating solvent in the reaction, and that small CsPbBr₃ nuclei form at room temperature before MWI heating which grow in 2D directions over time. In addition, absence of 2D structure in NPs prepared with hot-injection synthesis, confirmed that MWI is the answer to a fast and reproducible synthesis of CsPbBr₃ nanoplatelet.

Chapter 4 – 2D CsPbI₃ Nanoparticles Synthesis via Halide Exchange Reaction of CsPbBr₃ Nanoplatelets and PbI₂

Abstract

The capability of CsPbX₃ nanoparticles to undergo halide exchange reactions have been widely utilized in recent years. One of the halide exchange advantages is in fabricating CsPbI₃ NPs that have higher optical stability compared to the synthesized ones, owing to preservation of the structural properties of the CsPbBr₃ reactant. In this study, we successfully produced 2D I-rich CsPbX₃ nanoplatelets via a halide exchange reaction at room temperature. In this chapter, we describe the halide exchange mechanism of the 2D CsPbBr₃ nanoplatelets with a PbI₂ solution through comparison with 0D CsPbBr₃ nanoparticles. The results showed that 2D I-rich nanocrystals were shaped by halide exchange on the surface and shell-to-core halide migration. We modified the method to an in-situ reaction with the advantage of studying the structural properties of the nanoplatelets using XRD. In addition, this modified method promoted the halide exchange toward a complete conversion to CsPbI₃ nanoplatelets by removing the Br⁻ from the media. To examine the potential of CsPbI₃ nanoplatelets in thin film application, progression of halide exchange on a CsPbBr₃ film is also described.

4.1 Introduction

CsPbX₃ perovskite semiconductors have been a hot topic in materials science due to their outstanding properties such as, wide optical absorption, narrow photoluminescence (PL) emission, high quantum yield, high electron mobility, and low band gap energy.^{66,173,174} In addition, these optical and electronic properties can be tuned precisely to accommodate various applications in optoelectronic devices. These characteristics originates in the composition, structure and size of the perovskites which can be altered by either synthesis parameters or post-synthesis modification of CsPbX₃ perovskites. In particular, adjusting the composition via a halide exchange reaction of CsPbX₃ perovskites have been investigated in several studies.^{24,106,107,116} For example, right after the first report on the colloidal CsPbX₃ nanoparticle (NP) synthesis via the hot-injection method, a dynamic halide exchange was displayed between CsPbBr₃ and either CsPbI₃ or CsPbCl₃ NPs.^{6,103} Similar results were obtained by reacting the CsPbBr₃ with either PbI₂ or PbCl₂. A particular point of interest is the capability to produce stable I-rich perovskite NPs. Among CsPbX₃ perovskites, CsPbI₃ has the lowest band gap energy which makes it a great candidate for optoelectronic devices such as solar cells.^{175,176} Although synthesis of CsPbI₃ NPs is achievable with various methods, they often lose their PL in a short period of time due to structural changes leading to an orthorhombic δ phase.^{110,177,178}

Another perk of fabricating the NP of interest via halide exchange is the robustness and simplicity of the process. High reactivity of CsPbX₃ NPs in either colloidal form or thin film have made it possible to react them with various halide species under ambient conditions.¹⁷⁹ Such functionality has enabled the use of lead halide perovskites as a halide reservoir or a halide detector. For example, our lab showed that CsPbI₃ can be utilized as a halide reservoir to

catalyze an organohalide exchange in a Finkelstein reaction.²⁴ In another study, researchers detected several halomethanes in ppmv traces using CsPbBr₃.¹⁰⁹

Previously, we showed that 2D CsPbBr₃ nanoplatelets can be produced in the presence of benzyl ether (BE) via a microwave-assisted synthesis. In this study, we report on the halide exchange reaction of CsPbBr₃ nanoplatelets with PbI₂ while preserving the 2D structure. The reaction was monitored by UV-Vis absorption, PL emission and powder X-Ray Diffraction (XRD) measurements. We compared the halide exchange of the nanoplatelets with nanocube counterparts and introduced a modified *in-situ* method to better understand the structural changes during the reaction. Lastly, we present the challenges of halide exchange on a perovskite film. In this case, the 2D CsPbBr₃ NPs were coated on a borosilicate glass cover using a chemical route and employed in an exchange with a PbI₂ solution at room temperature.

4.2 Experimental

4.2.1 Materials

Lead(II) iodide (PbI_2 , 99%), lead(II) bromide (PbBr_2 , 99.99%), cesium carbonate (Cs_2CO_3 , 97%), oleyl amine (OAm, 70%, technical grade), oleic acid (OAc, 90%), 10-undecanoic acid, (3-mercaptopropyl)-trimethoxy silane solution (95%, Sigma-Aldrich), tetrabutylammonium tetrafluoroborate (99%, Sigma-Aldrich), dichloromethane, 1-octadecene (ODE, 90%), and benzyl ether (BE, 98%) were purchased from Sigma Aldrich.

4.2.2 Methods

4.2.2.1 Synthesis of CsPbBr_3 Perovskite Nanoplatelets

Synthesis of the CsPbBr_3 nanoplatelets was done by a microwave irradiation method reported in chapter 2. In summary, cesium oleate precursor was prepared by mixing 0.80 g of cesium carbonate, 2.4 μL OAc and 30 mL BE in 120 °C under vacuum. Lead bromide precursor was prepared by adding 2 mL of OAc and 2 mL of OAm to a 20 mL of 0.03 M PbBr_2 suspension at 120 C. Next, 3 mL of lead bromide precursor was purged with Ar gas for 5 min at room temperature, and 200 μL of an 85 °C cesium oleate precursor was injected to that, followed immediately by microwave irradiation (Discover-SP, CEM Inc.) at 160 °C. NPs were purified by first centrifugation at 10k rpm for 3 minutes, second, centrifugation at 4.4k rpm for 3 minutes and redispersed in toluene. In a modified purification method, a PbBr_2 solution in toluene was added to the precipitates after the first centrifugation.

4.2.2.2 Halide Exchange of CsPbBr₃ Nanoplatelets with PbI₂

A 18.8 mM solution of PbI₂ was prepared in 10 mL toluene by dissolving 86.5 mg of PbI₂ using 400 μ L 10-undecanoic acid and 700 μ L OAm. The mixture was heated at 80°C till complete dispersion of PbI₂. Then it was diluted to the relevant concentration for each halide exchange experiment. In a typical experiment, CsPbBr₃ NPs were purified and diluted in toluene and PbI₂ was titrated into a cuvette of the CsPbBr₃ solution. UV-Vis absorption and PL emission were monitored during the red-shift of the NPs.

4.2.2.3 In-situ Halide Exchange of CsPbBr₃ Nanoplatelets with PbI₂

Prior to the halide exchange, CsPbBr₃ nanoplatelets were purified and redispersed in toluene to the initial concentration. Then, CsPbBr₃ nanoplatelets and a 0.20 M PbI₂ solution were combined with $[I^-]:[Br^-] = 1:1$. The mixture was allowed to react for 30 min, then PL emission was measured without any dilution. For the XRD measurement, a portion of the mixture was separated, purified and drop-casted on a zero-diffraction quartz. The rest of the mixture was centrifuged and redispersed in toluene to the initial volume to remove the free Br⁻ in the solution. In the three following steps, PbI₂ with the same ratio of 1:1 was added to the remaining solution, followed by XRD and PL measurements.

4.2.2.4 Preparation of CsPbBr₃ Film on Borosilicate Glass Slides

First, borosilicate glass covers were rinsed with DMSO, ethanol, and DI water thoroughly. Then, they were etched in a %10 NaOH solution at ambient condition for 1 hour. Etched glasses were rinsed with DI water and dried in an 85 °C oven overnight. Next, the glass surface was functionalized by soaking in a 50 °C (3-mercaptopropyl)-trimethoxy silane solution (5%) for 18 h. The 5% (v/v) silane solution was prepared by mixing 2 mL (3-mercaptopropyl)-trimethoxy silane and 38 mL toluene and was kept at 50 °C using a water bath. CsPbBr₃

nanoplatelets were purified and dispersed in toluene prior to deposition on the functionalized glass surface. The glass covers were propped vertically in a stirring CsPbBr₃ solution at ambient condition for 24 h. Lastly, coated glasses were rinsed by toluene to prepare for the halide exchange.

4.2.2.5 Halide Exchange on CsPbBr₃ Film

Halide exchange was performed immediately after the cover glasses were coated by the CsPbBr₃ film. The coated glasses were submerged in a 0.3 mM PbI₂ solution and allowed to react for a specific amount of time without agitation. PbI₂ was prepared by heating 43.3 mg PbI₂, 0.4 mL OAm, and 0.2 mL 10-undecenoic acid in toluene at 80 °C for ~3h. After each step of the halide exchange reaction, the cover glass was rinsed with toluene and air-dried prior to optical absorption and PL emission measurements.

4.2.3 Instrumentation

UV-Visible Absorption Spectrophotometry (UV-Vis)

A Cary 50 Bio UV-Vis spectrophotometer (VARIAN Inc.) was used for the UV-Vis absorption measurements between 300 - 700 nm. CsPbBr₃ platelets were diluted in toluene for the measurements. Absorption of toluene was measured before addition of the NPs and automatically subtracted from the sample's spectrum. Absorbance of the colloidal samples were less than 0.1 to reduce reabsorption effects in photoluminescence measurements. In perovskite film measurements, absorption of a cleaned cover glass was used as the reference. Films were positioned vertically in a way that center of the films were absorbing the light in the same location for each measurement.

Photoluminescence Spectroscopy (PL)

PL emission spectra were recorded using a Cary Eclipse fluorescence spectrophotometer (VARIAN Inc.). The excitation wavelength was set at 400 nm and excitation and emission slit widths were set at 5 nm. For high concentration CsPbBr₃, a microplate reader accessory was positioned in the sample holder and the slit widths were set at 10 nm. The emission of the perovskite films was also recorded using the microplate reader by placing the cover glass on the microplate.

Powder X-Ray Diffraction (XRD)

A D2 PHASER XRD instrument with a Cu radiation source was used to produce the XRD spectra, according to the method described in chapter 2. Samples were prepared by drop-casting purified NPs on a zero-diffraction quartz holder.

Thermal Gravimetric Analysis (TGA)

A PerkinElmer Pyris1 instrument was used for the TGA measurements. The instrument was equipped with a thermal analysis gas station and <20% O₂ in N₂ tank. The analysis was performed at a heating rate of 15 °C.min⁻¹ between 50–750 °C.

Electrochemical measurements, Cyclic Voltammetry (CV)

A 600-E Electrochemical Analyzer instrument (CH Instruments Inc.) connected to a voltaic electrochemical cell was applied to run the cyclic voltammetry. An electrolyte solution of 0.1 M tetrabutylammonium tetrafluoroborate (Bu₄NBF₄) in DCM was first prepared. A glassy carbon electrode, a Pt wire, and an Ag wire were utilized for the working electrode (WE), counter electrode (CE), and quasi-reference electrode, respectively. The electrolyte solution was purged with Ar prior to the CV and a background CV was measured before the analysis of the NPs. To

prepare the perovskite-coated WE, the NPs were purified, drop-casted on the WE, and dried in air. Extra care was practiced in setting up the electrochemical cell to not disturb the NP film on the WE. CVs were run with a speed rate of 0.1 V/s between -2 and 2 V. All potentials are calibrated versus the Ferrocene/Ferrocenium (Fc/Fc^+) potential. After each measurement, Fc was added to the electrochemical cell (1.9 mM) and a CV was run to calculate the formal reduction potential of the Fc/Fc^+ redox couple.

4.3 Results and Discussion

Halide exchange reaction in CsPbX_3 NPs have been widely reported as a method to tune the optoelectronic properties of NPs. For this study, CsPbBr_3 nanoplatelets were synthesized using our previously reported method in chapter 2 and halide exchange was performed in order to synthesize stable CsPbI_3 nanoparticles with 2D structure. In short, a precursor of Cs-OAc and another containing Pb-OAc and OAm-Br were prepared in Benzyl Ether (BE). Then a mixture of the precursors was heated to 160 °C via microwave Irradiation (MWI). Halide exchange reaction between CsPbBr_3 and PbI_2 was performed on purified nanoplatelets at room temperature. The CsPbBr_3 nanoplatelets were diluted in toluene prior to the halide exchange reaction. Iodide source for this reaction was PbI_2 dissolved in toluene with Oleyl Amin (OAm) and either Oleic Acid (OAc) or 10-Undecanoic Acid (UnAc).

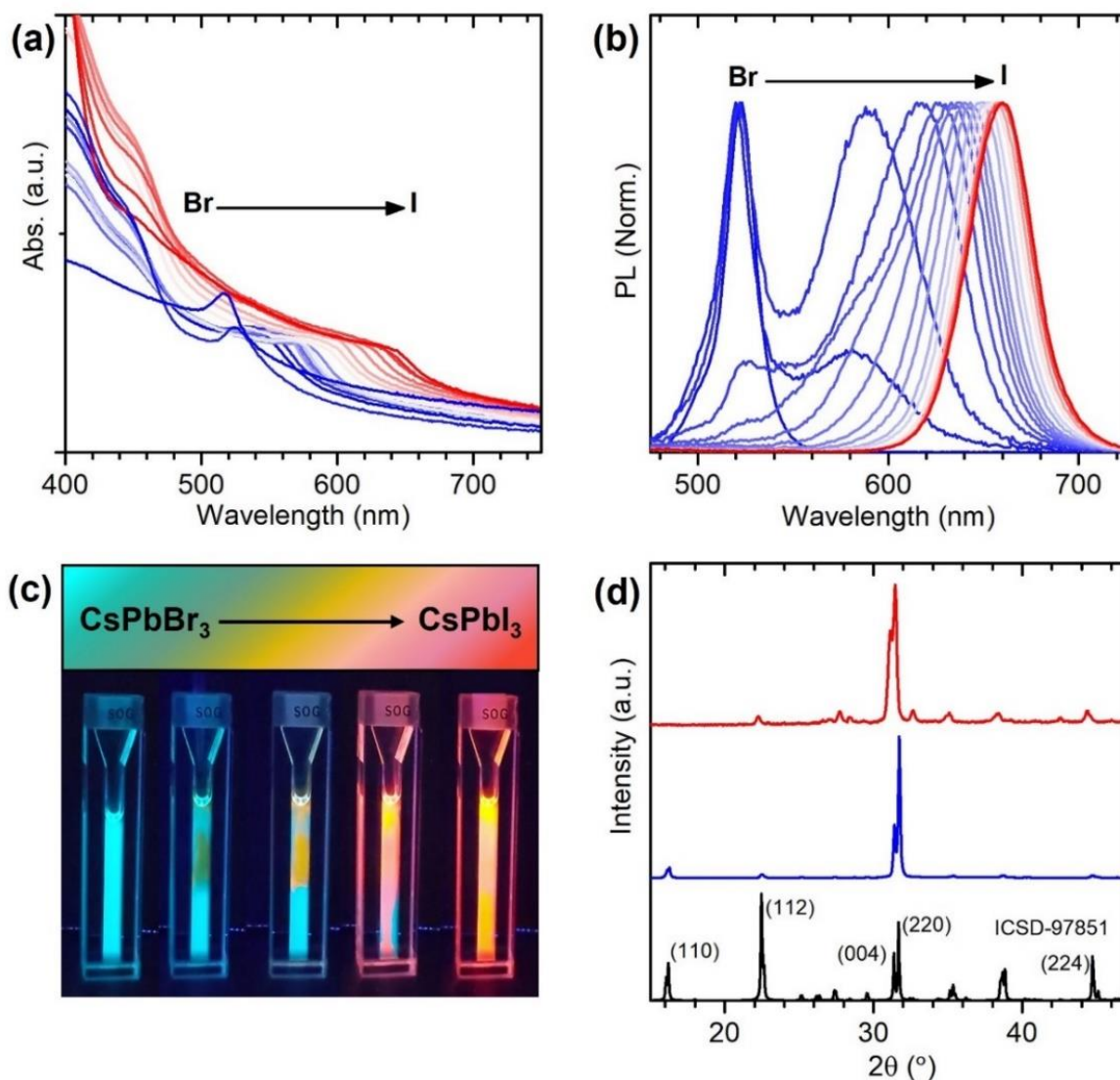


Figure 4.1. UV-Vis absorption (a) and photoluminescence emission (b) of CsPbX₃ during the halide exchange reaction of CsPbBr₃ and PbI₂. Pictures (c) taken during the halide exchange reaction under a UV lamp. XRD pattern (d) of CsPbBr₃ (blue), the post-reaction I-rich CsPbX₃ (red), and an orthorhombic CsPbBr₃ reference (black) 97851- ICSD.

Figure 4.1 shows a set of optical and structural properties of the NPs during the halide exchange reaction. UV-Vis absorption and PL emission were recorded every one minute as depicted in figure 4.1. Both absorption and emission peaks redshifted to higher wavelengths, characteristic of I-rich CsPbX₃ NPs. starting the halide exchange reaction from NPs with a monomodal

emission peak at ~523 nm resulted in a monomodal PL peak of I-rich NPs at ~660 nm, however, a bimodal emission peak was observed at the beginning of the reaction. The PL bimodality could arise from coexistence of Br-rich and I-rich NPs. The reaction was also visually observed under a UV lamp where PbI_2 was injected in a CsPbBr_3 solution at room temperature with no agitation. CsPbBr_3 nanoplatelet solution gradually changed colors upon exchanging the Br^- with I^- and turned red after about two minutes. Figure 4.1c illustrates the pictures taken during the reaction which demonstrates the *in-situ* progression of iodide species and the fast reaction with the CsPbBr_3 NPs while each color represents a different combination of halides in the NPs. XRD spectrum was measured before and after the halide exchange which are depicted in figure 4.1d along with an orthorhombic perovskite reference (97851- ICSD). The XRD pattern of CsPbBr_3 NPs matched with the orthorhombic crystal structure with prominent diffraction peaks from (110), (112), (004), (220), and (224) planes. The diffraction peak from (220) plane at 30.7° had a massive intensity that overshadowed the other peaks. Analogous to the previous chapters, this pattern was considered as the signature of the anisotropic structure of the platelets (Structural analyses are detailed in chapter 2). The characteristic XRD features of the nanoplatelets, particularly the enhanced intensity of (220) diffraction peak, were maintained in the I-rich NPs as well which proves the 2D morphology was preserved after the halide exchange.

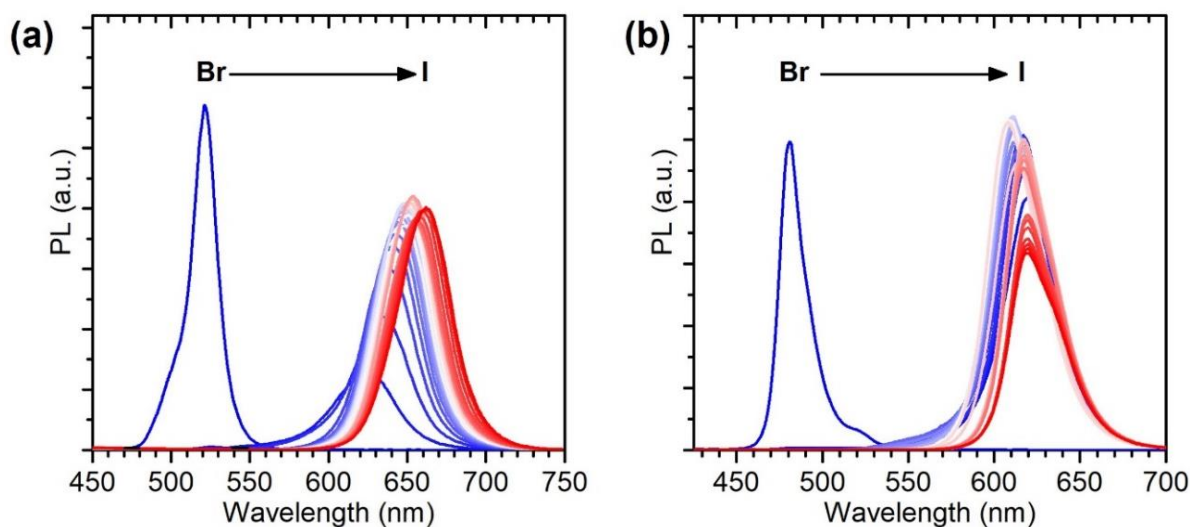


Figure 4.2. PL emission of 2D BE- CsPbX_3 (a) and 0D ODE- CsPbBr_3 (b) during the halide exchange reaction of CsPbBr_3 and PbI_2 . PbI_2 was added in three steps of 50 μL .

The results in figure 4.1 showed that CsPbBr_3 nanoplatelets can exchange Br^- with an I^- source spontaneously at room temperature, while both PL intensity and structural properties are retrieved after the reaction. We then compared the halide exchange reaction of the CsPbBr_3 nanoplatelets with CsPbBr_3 nanocubes prepared in ODE under a similar condition. Optical and structural properties of these nanocubes are illustrated in figure 3.1 which demonstrated the ~ 10 nm nanocubes with PL emission at 481 nm. Both nanocubes and nanoplatelets were purified and redispersed in toluene, then 50 μL PbI_2 aliquots were added in three steps to ensure a maximum exchange. UV-Vis absorption of nanoplatelets and nanocubes were set at 0.06 to ensure a similar concentration. Concentration of PbI_2 was 45, 90 and 135 μM in the cuvette after each addition. Figure 4.2 shows the PL emission shifted gradually from ~ 522 nm to higher wavelengths reaching ~ 648 nm during the first step in nanoplatelets' reaction (~ 126 nm red-shift). The PL emission of the nanocubes had a big jump from ~ 481 to ~ 614 nm during the first step (~ 133 nm red-shift). The sudden PL shift and seemingly faster reaction in nanocubes could be the result of

several factors. Firstly, it could originate from an intrinsic higher reactivity in nanocubes. Secondly, it could simply be a difference in the concentration of the NPs, more precisely the Br^- amount. It should be noted that the concentration was initially set equal between different batches by fixing the absorption value at the excitation wavelength, 400 nm. The issue with this method will be discussed later in details and a more robust technique will be introduced. Lastly, it could demonstrate the availability of Br^- species in 0D NPs versus 2D NPs. To understand the roots of these differences, we designed the halide exchange experiments in various conditions.

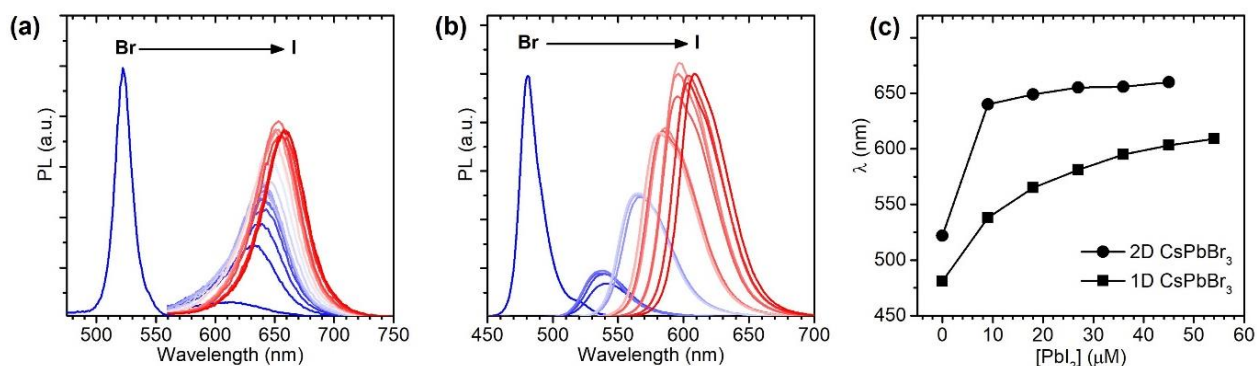


Figure 4.3. PL emission of 2D BE- CsPbX_3 (a) and 1D ODE- CsPbBr_3 (b) during the halide exchange reaction of CsPbBr_3 and PbI_2 . (c) shows the trend of maximum emission wavelength over the course of the reaction. PL was recorded after addition of 10 μL PbI_2 until the emission was stable.

We followed with two different control experiments to investigate if this difference between nanocubes and nanoplatelets derives from the nature of NPs' reactivity. In one experiment, the PbI_2 source was added to the NPs in a smaller aliquot of 10 μL with the concentration ranging from 9 to 45 μM . After each addition, PL emission spectrum was recorded several times until the PL intensity and wavelength were stable. This step was repeated four more times where the PL

shift was not significant anymore. The results are shown in figure 4.3. The PL shift followed two different patterns in nanocubes and nanoplatelets. After the first PbI_2 addition, the nanoplatelets experienced a gradual shift in wavelength (~ 522 nm to ~ 640 nm), nevertheless the wavelength stabilized after a huge red-shift of ~ 118 nm. In the contrary, the nanocubes had a sudden PL shift (~ 481 nm to ~ 538 nm) which showcased a smaller red-shift of ~ 57 nm. Another interesting observation was that the total change in the PL wavelength of the nanoplatelets after several PbI_2 addition was 16 nm more than that of the nanocubes. The nanoplatelets' results can be explained if first a halide exchange happens on the surface of the NPs then the I^- ions migrate toward the core of the NPs while Br^- ions move to the surface and consequently, the exchange will continue among surface Br^- and I^- species in the solution. However, for the nanocubes this means the I^- could not diffuse into the NPs' core without destabilizing the NPs, unless the halide equilibrium was forced by a higher I^- concentration. This also accounts for the broad PL peak of nanoplatelets as the emission wavelength could cover a wide range based on the variety of halide ratios in the beginning of the reaction. While the monodispersed size distribution of nanocubes and consequently, uniform halide composition resulted in narrower emission. We note that the initial PL change in the nanoplatelets were also ~ 20 nm higher than the initial shift of the nanocubes. This significant difference suggested that with low I^- content, a higher exchange of halides is possible in nanoplatelets. The larger surface to volume ratio and higher surface energy in smaller NPs can lead to higher activation energy for the halide exchange in nanocubes. Additionally, the NP structure can be destabilized by distortion of the octahedral PbX_6^{4-} while the 2D structure has a better capacity for halide exchanged induced distortions in the reactions with low I^- content.

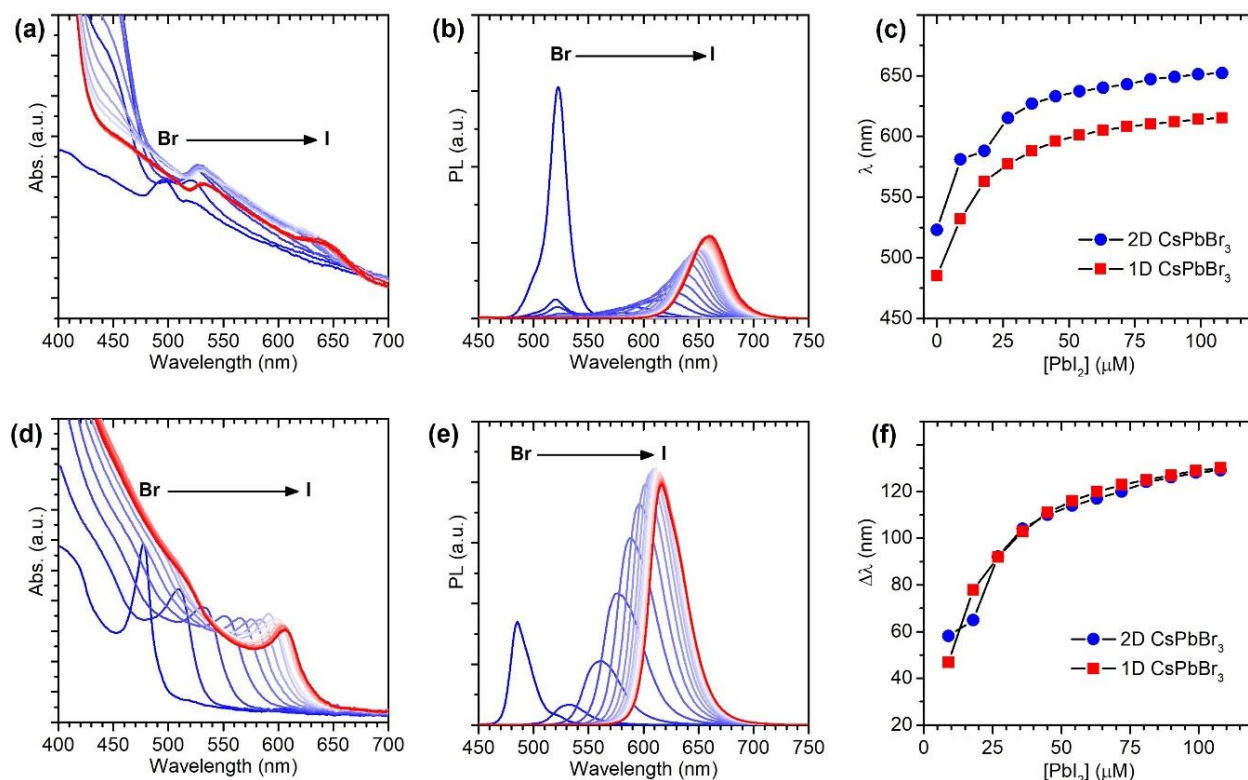


Figure 4.4. UV-Vis absorption and PL emission spectra of 2D BE-CsPbX₃ (a-b) and 1D ODE-CsPbBr₃ (d-e) during the halide exchange reaction of CsPbBr₃ nanoplatelets and PbI₂. (c) shows the trend of maximum emission wavelength versus PbI₂ concentration over the course of the reaction and (f) shows the difference of emission wavelength between CsPbX₃ at each step and the initial CsPbBr₃. 10 μ L PbI₂ was added every minute for 12 minutes and absorption and PL were recorded after each addition.

In the next control experiment, the halide exchange reaction was controlled by addition of 10 μ L PbI₂ to the NPs every minute and UV-Vis absorption and PL emission spectra were obtained for each step, as depicted in figure 4.4. In this case, the NPs were reacted with equal amounts of PbI₂ in a shorter timeline of 12 minutes with the PbI₂ concentration ranging from 9 to 108 μ M. The analyses of the PL emission in figure 4.4c and 4.4f show that the PL emission redshifted similarly in either nanocubes or nanoplatelets except in the two initial additions. This confirms that a higher number of surface Br⁻ might undergo halide exchange in nanoplatelets without

destroying the crystal structure, resulting in larger red-shifts in low Γ content. However, nanoplatelets and nanocubes had a similar halide exchange rate with higher Γ content and the Γ diffusion rate did not limit the reaction of nanoplatelets and high concentration of Γ . Also, in agreement with the last two experiments, the nanoplatelets demonstrated a wider PL peak with a larger maximum wavelength. As discussed before, the reason behind the broad peak was the polydispersity of the nanoplatelets.

While PL emission provided valuable insight into the mechanism of the halide exchange in CsPbBr_3 nanoparticles, there are uncertainties in interpreting the emission data as only affected by the halide composition. Therefore, we decided to investigate the structural changes of nanoplatelets during the halide exchange by XRD analysis as well.

We note that the UV-Vis absorption spectra of NPs were acquired prior to the compared experiments and absorptions at 400 nm (PL excitation wavelength) were matching between the nanocubes and nanoplatelets. This method was used to estimate an equal concentration between two different sets of experiments. A common method to calculate the perovskite NP concentration is to use the extinction coefficient (ϵ) calculated for the CsPbBr_3 quantum dots.¹⁸⁰ However, such ϵ values are reported for 0D nanocubes only and should not be applied in calculating the concentration of 2D nanomaterials. On the other hand, larger nanoplatelets in our system tend to scatter light as evidenced in the absorption spectrum in figure 4.1a, therefore, the ϵ would differ even more from the value for nanocubes.

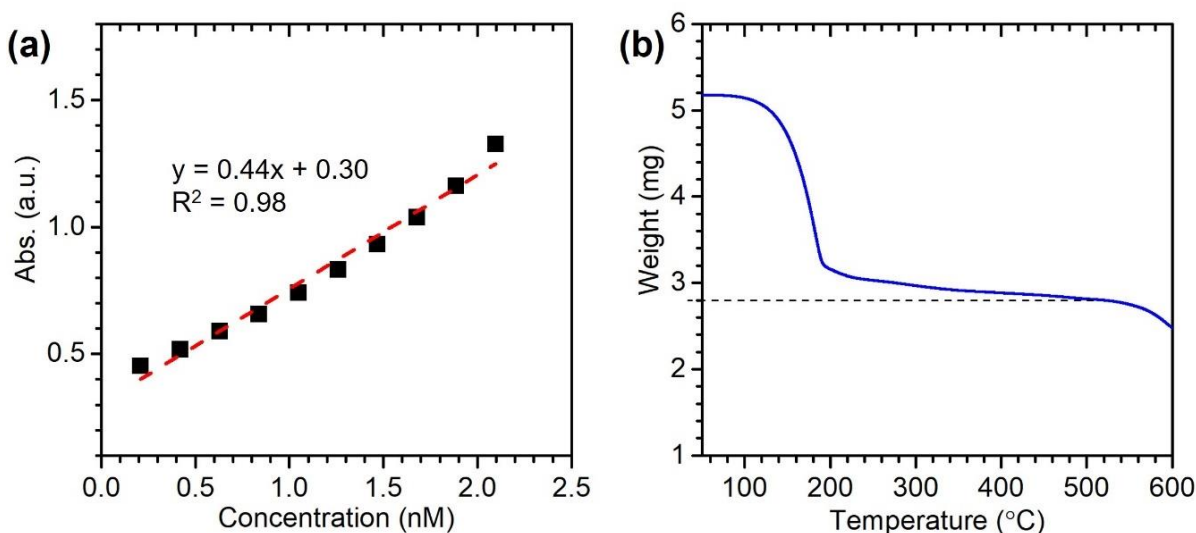


Figure 4.5. Calibration curve (a) and TGA (b) of CsPbBr₃ nanoplatelets. Concentration of a known volume of the CsPbBr₃ solution was calculated using the mass of the NPs from TGA and calibration curve was produced for several dilution of the same stock solution.

To tackle this problem, we adopted a method by Ravi et. al. to calculate the nanoplatelets concentration by TGA analysis and used a UV-Vis calibration curve to estimate the extinction coefficient of the nanoplatelets.¹⁸¹ The TGA and calibration plot are shown in figure 4.5. First, a known volume of the nanoplatelets dispersion was purified and concentrated with care to minimize particle loss. Then, a TGA was performed to obtain the mass of the NPs apart from the organic content. Mass of each nanoplatelet was estimated using the dimension of the NPs and density of bulk CsPbBr₃ crystals. Totals mass of the NPs was divided by the mass of one NP to quantify the number of nanoplatelets, followed by calculation of NPs' moles using Avogadro's number. Lastly, moles of the nanoplatelets and the known volume of the dispersion was used to calculate the molar concentration. This concentration was used as a reference to calculate the concentration of 10 different diluted solutions from the same batch of the nanoplatelets. A calibration curve was then developed by measuring the absorption of these samples at 400 nm

and an extinction coefficient value of $4.5 \times 10^8 \text{ M}^{-1} \cdot \text{cm}^{-1}$ was determined for the CsPbBr₃ nanoplatelets, accordingly.

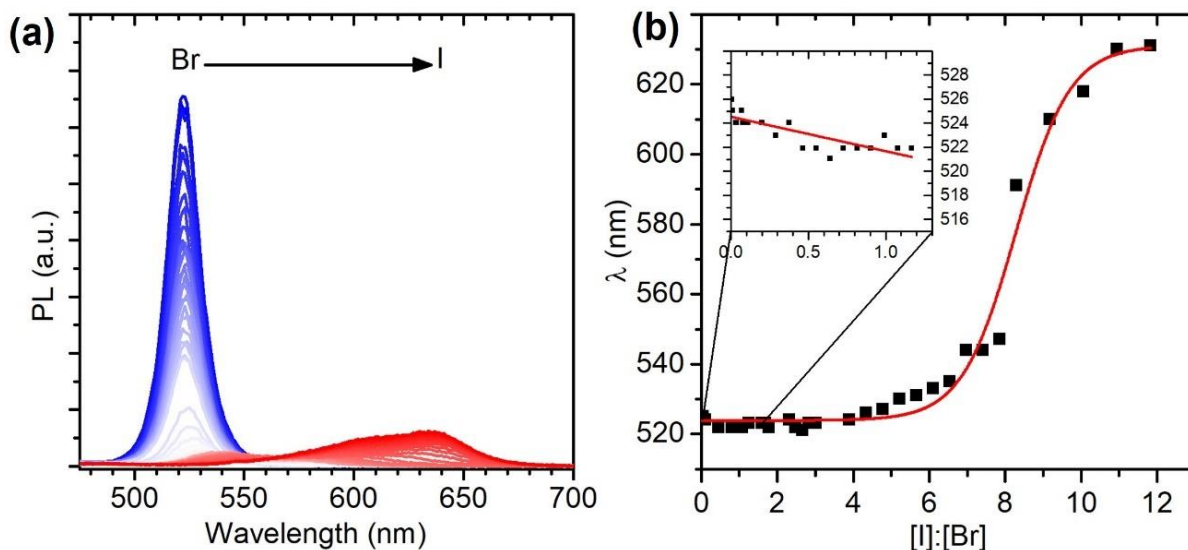


Figure 4.6. PL emission spectra of 2D BE-CsPbX₃ (a) during the halide exchange reaction of CsPbBr₃ nanoplatelets and PbI₂ with [I⁻] to [Br⁻] ratio ranging from 0.0005 to 3. (c) shows the trend of maximum emission wavelength versus [I⁻]:[Br⁻] ratio over the course of the reaction.

Quantification of the concentration helped us to reevaluate the halide exchange strategy at three fronts. For example, the Br⁻ concentration was significantly higher in the nanoplatelets compared to the nanocubes with the same concentration. Therefore, we concluded that the best way to investigate the halide exchange is to add the I⁻ source with respect to the Br⁻ content of a sample. Next, we performed a halide exchange experiment with [I⁻] to [Br⁻] ratio ranging from 0.0005 to 3. PL emission, illustrated in figure 4.6, did not red-shifted in lower ratios than 0.3. Instead, PL gradually quenched with a slight shift to lower wavelengths. A ratio of 1 or higher was required to initiate a red-shift. Although, the factors behind this inconsistency were not clear, the

quenching and blue-shift of the nanoplatelets suggested that in this diluted solutions, NPs are probably ripped apart before Γ^- can diffuse into the structure.

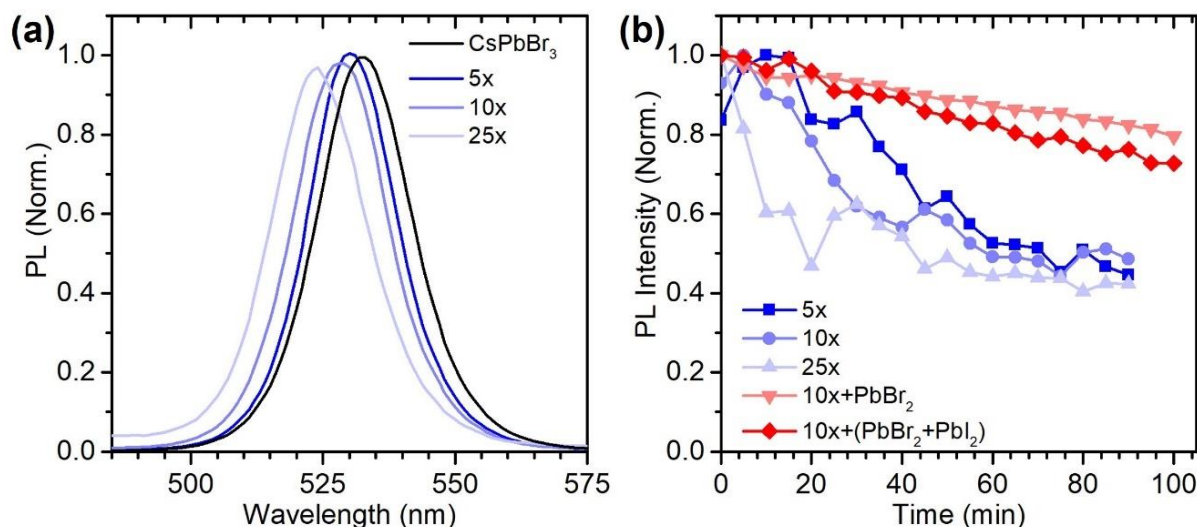


Figure 4.7. PL emission spectra of CsPbBr₃ nanoplatelets diluted in toluene by a factor of 5, 10 and 25 (a). Trend of PL intensity at maximum quenching over time (b) for 5x, 10x and 25x diluted CsPbBr₃ nanoplatelets vs the 10x solution modified by PbBr₂ and a 50:50 (v/v) PbBr₂:PbI₂.

This was further investigated by monitoring the PL emission of diluted NP solutions over time in absence of the Γ^- source. Figure 4.7a illustrates the blue-shift in the PL emission of the three different diluted solution of NPs versus the stock solution with PL emission at ~536 nm. We noticed when NPs are diluted in toluene, PL wavelength blue-shifted slightly, and PL intensity quenched slowly over time as well. On top of that, the lower the concentration the larger PL emission blue-shifted and quenched. Hence, we modified the experiment by utilizing a fluorospectrometer equipped with a microplate reader in order to assess a high concentration halide exchange reaction. In this method the inner filter effect is not an issue as the PL emission from the excited NPs on the surface is detected. To improve dispersity and QY of the NPs, we

also adjusted the purification process by incorporating a $\text{PbBr}_2(\text{OAc/OAm})$ solution in toluene, a method developed previously in our lab.¹⁰⁸ In this case, after spinning down the NPs, the PbBr_2 solution was added to the precipitates instead of toluene for a better surface passivation and the excess ligands were washed away in the next step. PL emission of the nanoplatelets and three diluted solutions (5x, 10x, 25x) were recorded every 5 minutes along with two 10x diluted solution purified with the modified method. One sample was purified using the PbBr_2 solution and the other one using a 50:50 (v/v) mixture of $\text{PbBr}_2\text{:PbI}_2$ solution. Figure 4.7b shows the trend of PL emission quenching over 90 minutes for these samples. Emission from 5x and 10x diluted samples quenched 50% and plateaued after one hour while PL of the 25x diluted sample dropped faster. However, the modified samples retained ~80% of their initial emission even after one hour which demonstrates how the modified purification technique limited the PL decay in CsPbBr_3 nanoplatelets.

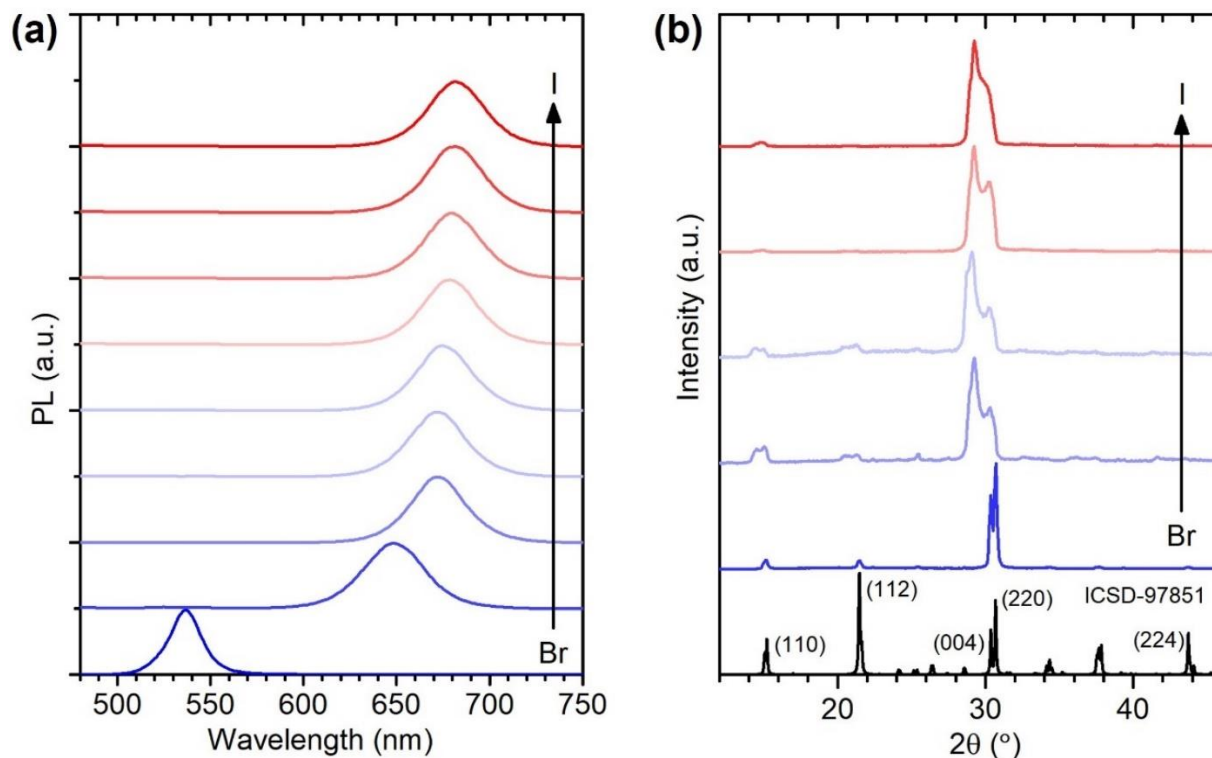


Figure 4.8. PL emission (a) and XRD pattern (b) of 2D BE-CsPbX₃ during the halide exchange reaction of CsPbBr₃ and PbI₂ (0.195 M). The CsPbX₃ NPs were purified and reacted with an [I⁻]:[Br⁻] ratio of 1:1 four times and PL was measured in 2 and 30 minutes after each addition.

With the above information in hand, we designed an *in-situ* halide exchange experiment where CsPbBr₃ nanoplatelets were purified and redispersed in toluene to the initial concentration. The optical and structural changes during this halide exchange were monitored as illustrated in figure 4.8. In this case, CsPbBr₃ nanoplatelets and PbI₂ solution were combined with 1:1 ratio of [I⁻]:[Br⁻]. Then, a portion of the mixture was separated and prepared for an XRD measurement. At this step, PL emission spectrum was obtained after two minutes and thirty minutes of reaction. Then the mixture was centrifuged and redispersed in toluene to the initial volume. This step purifies the NPs from the excess Br⁻ in the solution and prevents a reverse halide exchange

reaction. Again, PbI_2 with the same ratio was added to the remaining solution with respect to the new Br^- concentration, followed by XRD and PL measurements. These steps were repeated four times, figure 4.8 shows PL emission and XRD after each step of the reaction. PL emission red-shifted from 536 nm to 673 nm after the first addition and stabilized at 682 nm after the fourth addition. The red emission at 682 nm aligns closely with a typical CsPbI_3 emission (figure 2.10) which demonstrates that a near-complete halide exchange from CsPbBr_3 to CsPbI_3 is achievable by removing the excess Br^- from the system.

Figure 4.8b shows the XRD pattern of the NPs in each step of the reaction. While a peak widening was observed after the first step due to the excess ligands, the high intensity double diffraction peaks from (004) and (220) planes persisted in each step till the end. In addition, it appeared that a second set of orthorhombic NPs with slightly different lattice parameters were present which gave the XRD pattern a double peak for each diffraction. We calculated the lattice parameter c of the unit cell in each step using the (004) diffraction peak at 2θ of 30.7° . The result show that unit cell expanded after the halide exchange with the c value growing from 11.98 to 12.21 Å. The larger size of the I^- species accounts for the 0.23 Å expansion which agrees with a 0.20 Å difference between octahedral complexes of PbX_6^{4-} with either halide.¹⁸² This method illustrated a better picture of the structural changes during a complete halide exchange and showed the advantage of XRD analysis along with PL survey in investigating perovskite reactions.

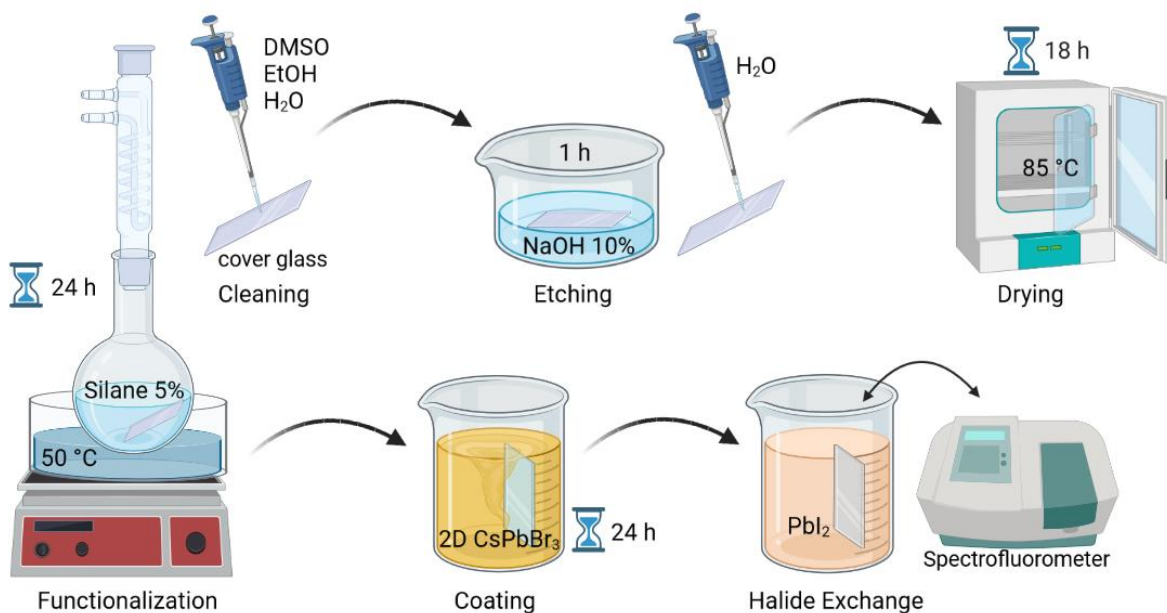


Figure 4.9. Schematic overview of CsPbBr₃ film preparation and halide exchange created with BioRender.com.

Aside from the halide exchange reaction in the perovskite colloids, several studies have been reported on the halide exchange of perovskite films.^{102,116,183} These studies are particularly important in understanding the performance of the perovskite films as a common form of perovskites in optoelectronic devices.^{114,184} We explored two aspects in perovskite thin films: the halide exchange capability in an immobilized form and the stability of the reacted film. To investigate this, we coated a borosilicate cover glass with CsPbBr₃ 2D perovskite and gradually reacted the CsPbBr₃ with I⁻ in a PbI₂ solution. A schematic representation of these steps from the cover glass preparation until halide exchange is shown in figure 4.9. Etching the glass surface was done by a high concentration NaOH solution (10%) in order to prepare the glass surface to cross-link with the O-Si of the (3-mercaptopropyl)-trimethoxy silane. The methoxy groups on the (3-mercaptopropyl)-trimethoxy silane were first hydrolyzed and self-condensed via Si-O-

Si bonding, followed by cross-linking of the silane with the glass surface. To make the perovskite film, nanoplatelets were deposited on the functionalized cover glass overnight. The CsPbBr₃ film was then submerged in the PbI₂ solution and PL emission of the films were recorded over the course of the halide exchange reaction. Silane compounds have been used in stabilizing perovskites for different purposes. In one study, passivating the perovskite layer with a crosslinked layer of trichloro(octyl)silane increased the stability and photovoltaic performance of the film by cross-linking the grain boundaries and reducing the trap density.¹⁸⁵ In another study, dodecyltrichloro silane was reported as the Cl⁻ source in a halide exchange reaction and ligand for CsPbCl₃ NPs which increased dispersibility and QY of the Cl-rich CsPbX₃ NPs. In this report, Uddin et. al. hypothesized that oxygen from O-Si could coordinate to Pb on the surface of the perovskites.¹⁰⁴ In a recent study, 3-aminopropyl(diethoxy)methyl silane (APDEMS) was used in a colloidal MAPbX₃ synthesis via LARP technique which demonstrated high dispersibility and PL stability as shown in figure 4.10.¹⁸⁶ Herein, we use (3-mercaptopropyl)-trimethoxy silane to immobilize the CsPbBr₃ nanoplatelets on the cover glass to stabilize the film during the halide exchange reaction and rinsing of the perovskite film.

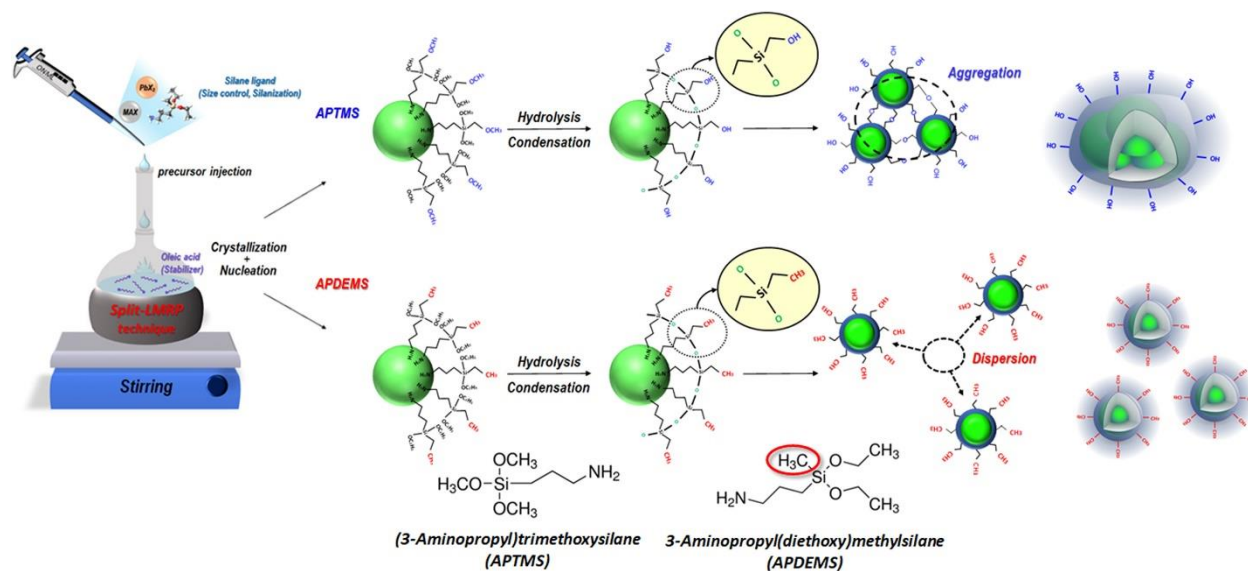


Figure 4.10. Schematic illustration of MAPbBr₃ QDs@SiO₂ core/shell LARP synthesis using (3-aminopropyl)trimethoxy silane (APTMS) and 3-aminopropyl(diethoxy)methyl silane (APDEMS).¹⁸⁶

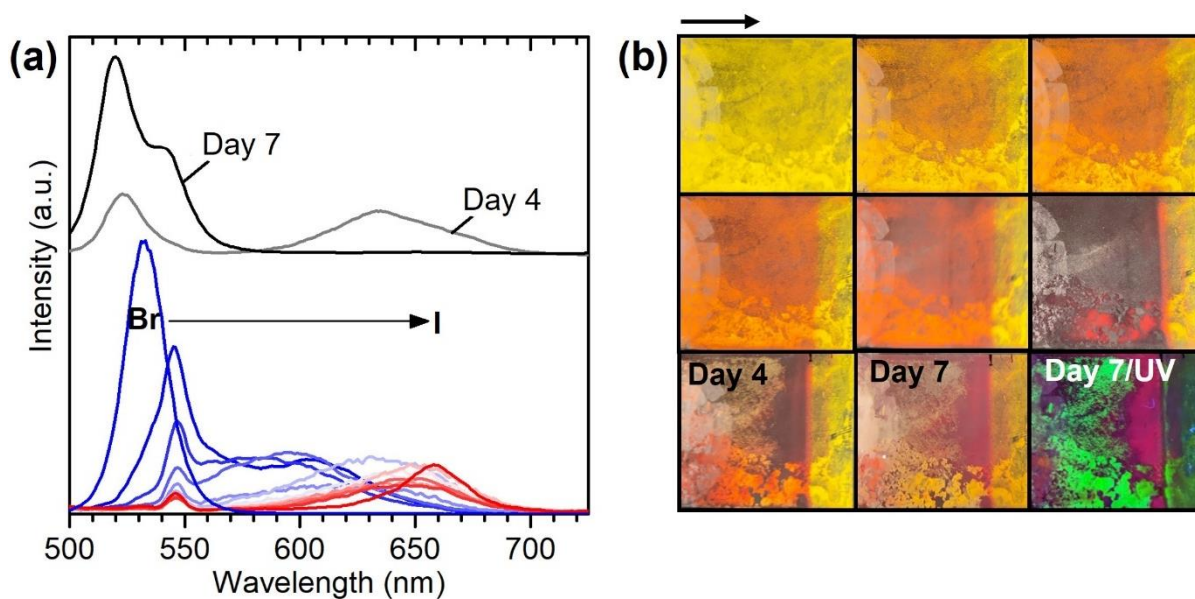


Figure 4.11. PL spectra (a) and optical images (b) during the halide exchange reaction between CsPbBr₃ film and PbI₂. PL emission from the middle section of the films is reported. PL emission and images of the film 4 days and 7 days after the halide exchange are marked.

PL emission of the perovskite film during the halide exchange reaction is shown in figure 4.11, along with pictures of the film in several stages. The emission peak shifted from 531 nm to higher wavelengths while a small peak around 545 nm persisted till the end of the experiment. As presented in figure 4.11b, the yellow color of the film changed to orange and eventually dark brown, visually displaying the transition to I-rich perovskite film. These results demonstrated that the halide exchange was achievable on the cover glass. Also, the I-rich NPs did not dissociate from the surface after 24 h submerging in the PbI_2 solution and rinsing with toluene before each measurement. After the halide exchange, the I-rich perovskite film was stored at room temperature under ambient conditions and its properties were monitored over the next week. Interestingly, the dark brown color of the film changed to brighter red and yellow colors over time with PL showing two strong emissions that blue-shifted (denoted as day 4 and day 7 in the figure 4.11). As illustrated in figure 4.11b, in this experiment, a small section of the film was not exposed to PbI_2 for the contrast comparison and due to nonhomogeneous deposition of the NPs, patches of dense NPs were formed on the cover glass. We suspected that these inconsistencies might have led to further migration of the halides after the halide exchange reaction resulting in Br-rich and I-rich sections on the film.

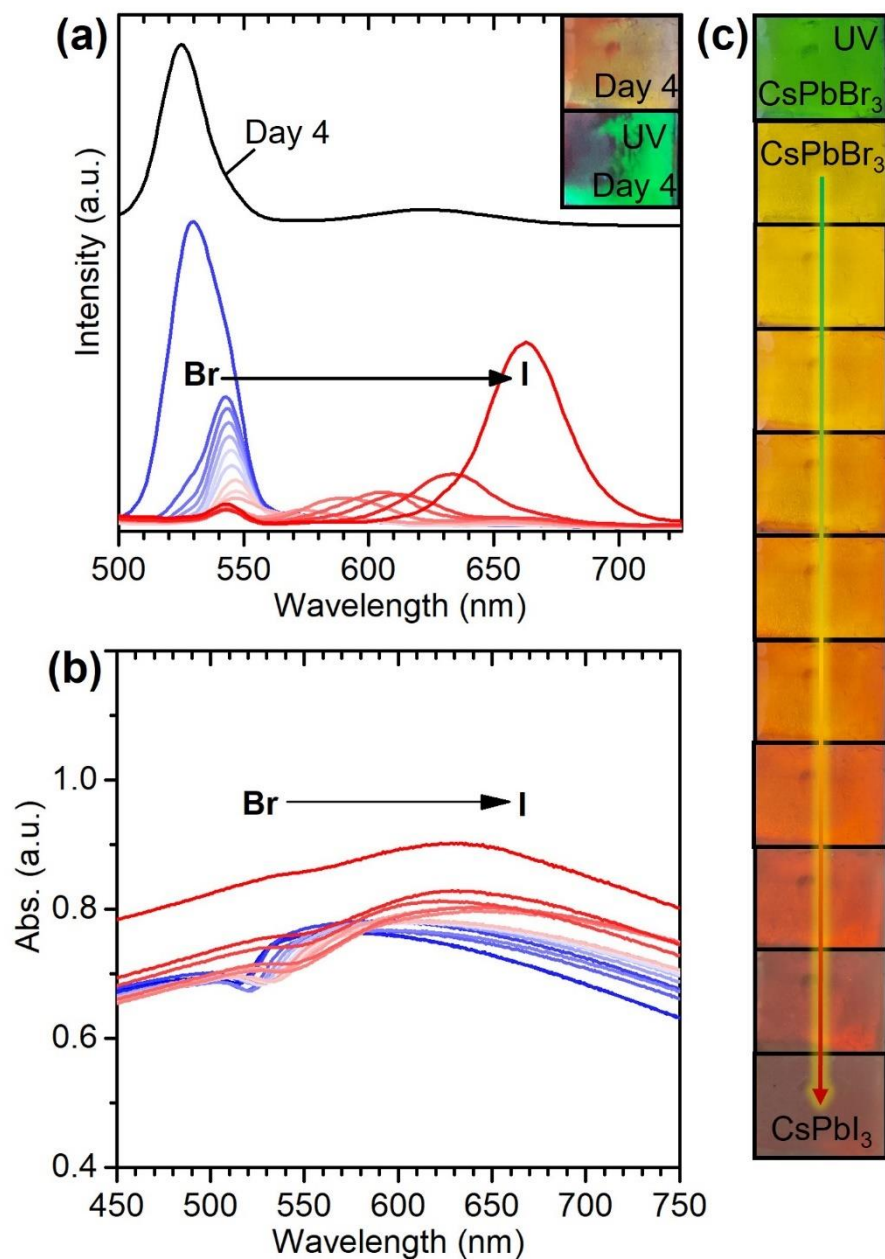


Figure 4.12. PL emission (a) and UV-Vis absorption (b) spectra and optical images (b) during the halide exchange reaction between CsPbBr₃ film and PbI₂. PL emission and images of the film 4 days after the halide exchange are marked.

Accordingly, the NP deposition method was modified to produce a more even layer and during the halide exchange reaction, the cover glass was completely submerged in the PbI₂ solution. The

PL emission of the perovskite film followed a similar trend during the halide exchange reaction as shown in figure 4.12a and c. Emission wavelength red-shifted from ~533 nm upon reaction with I^- to ~664 nm and shifted back to the green region after 4 days under ambient conditions. These results show that although a uniform $\text{CsPb}(\text{Br/I})_3$ film is formed after the halide exchange, Br^- and I^- are segregated in two sections of Br-rich and I-rich CsPbX_3 , over time, in absence of a homogeneous solution.

Another important characteristic of the all-inorganic perovskites that must be evaluated for optoelectronic applications is the band gap value and the nature of the conduction band minimum (CBM) and valence band maximum (VBM). The band gap energy can be calculated using the excitonic peak in the UV-Vis absorption spectrum by a simple wavelength conversion. For instance, CsPbBr_3 nanoplatelets with an absorption spectrum shown in figure 4.13b, had an optical band gap of 2.37 eV. Another method to determine the band gap value is through cyclic voltammetry, with which, the nature of the CBM and VBM can be investigated as well.^{31,187,188} In one study, Ravi et. al. evaluated the electrochemical parameters of five different CsPbX_3 NPs by cyclic voltammetry using a 50 mM tetrabutylammonium perchlorate solution in a toluene/acetonitrile mixture. This comparison between the CBM and VBM values in different halide composition demonstrated a stronger dependence between the halide type and the VBM which agreed with the hypothesis that VBM mostly consists of *p* orbitals of the halides while Pb orbitals are the major component of the CBM. In addition, they reported a 2.50 eV band gap for the CsPbBr_3 NPs which was comparable with the optical band gap of 2.48 eV.³¹ In another study, Samu et. al. investigated the electrochemical reactions happening during a cyclic voltammetry of a CsPbBr_3 film. Their results suggested that the observed cathodic and anodic

peaks were corrosion potentials rather than charge transfer in the CBM and VBM.¹⁸⁸ In any case, valuable information regarding either charge transfer and/or stability of the perovskite materials can be deduced from the cyclic voltammograms.

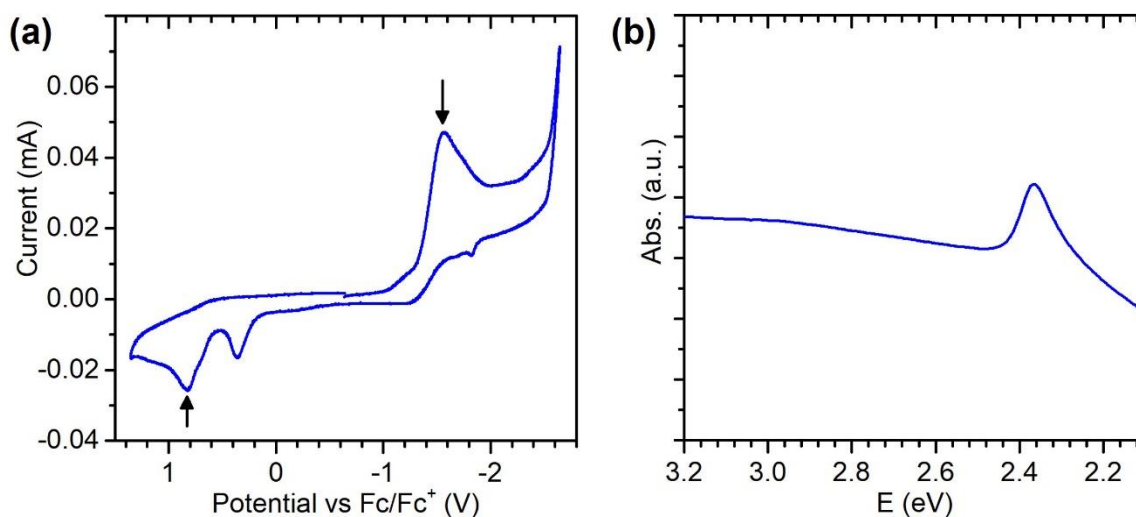


Figure 4.13. Cyclic voltammogram (a) and UV-Vis absorption spectrum (b) of CsPbBr₃ nanoplatelets. Cyclic voltammetry was recorded using a 0.1 M Bu₄NBF₄ (in DCM) with the scan rate of 0.1 V/s.

Herein, we calculated the electrochemical band gap using cyclic voltammetry and compared it to the optical band gap. Figure 4.13a shows a cyclic voltammogram of CsPbBr₃ nanoplatelets in dichloromethane using tetrabutylammonium tetrafluoroborate (Bu₄NBF₄) as an electrolyte where a CsPbBr₃ film was dried on a glassy carbon working electrode's surface. Potential is reported vs Fc/Fc⁺ as an internal standard per IUPAC recommendation.¹⁸⁹ For this analysis, 36 cycles were recorded at 0.1 V/s and the final cycle is illustrated in figure 4.13a. We interpreted the potential values of the oxidation peak at 0.81 V and the reduction peak at -1.56 V as the electron transfer

at the HOMO of the valence band and LUMO of the conduction band in the CsPbBr₃ nanoplatelets, respectively. The energy values at the CBM and VBM were calculated using the following equation.

$$E_{\text{HOMO/LUMO}} (eV) = - (E_{\text{Ox/Red}} - E_{\text{Fc/Fc}^+}^{1/2}) eV - 4.80 eV \quad \text{Equation 9.}$$

The electrochemical band gap of 2.39 eV was then calculated from the difference of the LUMO (− 3.22 eV) and HOMO (− 5.61 eV) energy values which was close to the optical band gap of 2.36 eV (524 nm) from the UV-Vis absorption measurement in figure 4.13b. Several other oxidation peaks were also observed in each cycle which suggests other species might be created and/or oxidized during the analysis. As Samu et. al. reported CsPbBr₃ and PbBr₂ could undergo oxidation during a cyclic voltammetry.¹⁸⁸ However, more analysis is required to assign these peaks to each phenomenon in this study.

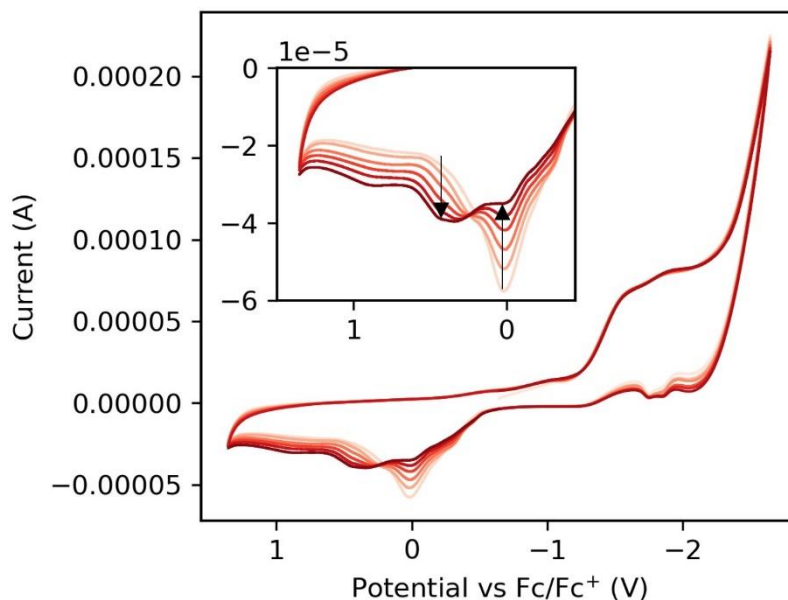


Figure 4.14. Cyclic voltammogram of CsPb(Br/I)₃ nanoplatelets in a 0.1 M Bu₄NBF₄ (in DCM) with the scan rate of 0.1 V/s over six cycles.

We also performed a cyclic voltammetry with the I-rich CsPb(Br/I)₃ NPs prepared by the halide exchange of CsPbBr₃ nanoplatelets and PbI₂. Our results agree with Ravi et. al. data, showing a significant shift in the oxidation peak potential for I-rich NPs. Figure 4.14 shows the cyclic voltammogram of I-rich CsPb(Br/I)₃ nanoplatelets. The band gap for the I-rich nanoplatelets was assessed using the above calculation. The reduction peak at ~ -1.6 V and oxidation peak at 0.34 V were assigned to CBM and VBM, respectively. Thus, the band gap was 1.94 eV for I-rich NPs which showed a decrease of 0.45 eV compared to the CsPbBr₃ nanoplatelets. (The optical band gap for I-rich NPs was ~ 1.97 eV.) I-rich NPs, similar to CsPbBr₃ nanoplatelets, showed several oxidation peaks other than the VBM peak. One interesting observation was the change in the intensity of the two oxidation peaks over the cycles. Particularly, the peak assigned to the HOMO of the VB increased over the 15 cycles.

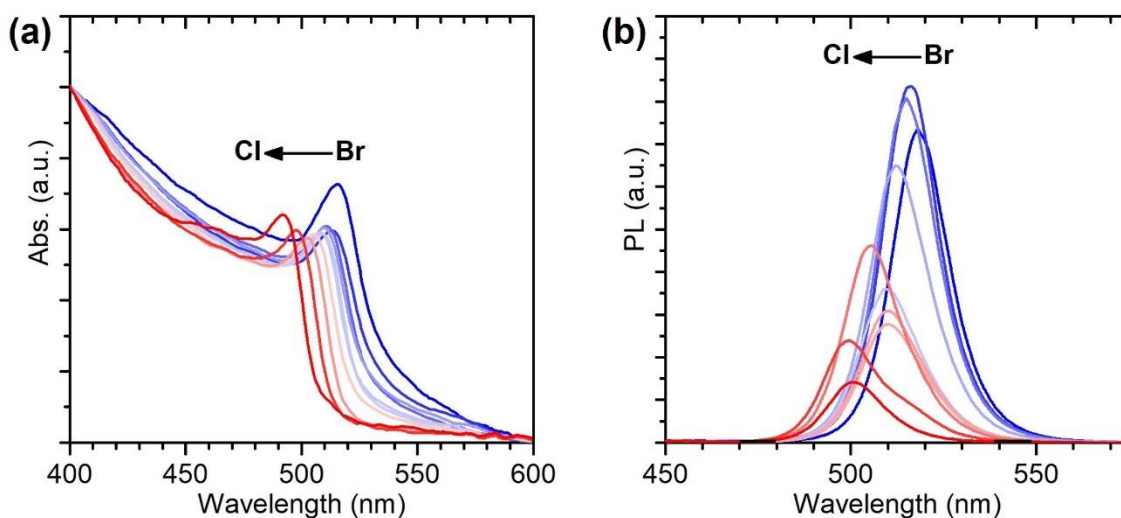


Figure 4.15. UV-Vis absorption (a) and PL emission (b) spectra during the halide exchange reaction of CsPbX_3 and HAuCl_4 .

While halide exchange between CsPbBr_3 NPs and an I^- source has interested many due to its wide range of visible absorption, simplicity of the method and stability of the I-rich products, some researchers have also investigated the halide exchange to produce Cl-rich perovskite NPs. CsPbCl_3 NPs are particularly utilized in blue light LEDs.^{7,190} In figure 4.15 halide exchange experiments with Cl containing precious metal complexes are shown. Overall, these results show CsPbBr_3 nanoplatelets can undergo halide exchange to make Cl-rich NPs as well.

4.4 Conclusion

A successful synthesis of 2D CsPbI₃ NPs is reported via halide exchange between 2D CsPbBr₃ NPs and a PbI₂ solution. The CsPbBr₃ nanoplatelets were prepared according to a MWI method in BE, described in chapter 2. The retention of the 2D morphology from CsPbBr₃ to CsPbI₃ NPs was confirmed by the signature peaks in the XRD pattern. As discussed in chapter 2, the diffraction peaks from (220) and (004) planes in these perovskite nanoplatelets demonstrated a much higher intensity compared to the other peaks which arose from the 2D growth perpendicular to these planes. A comparison between the halide exchange in 0D and 2D NPs revealed that the halide exchange reaction between 2D CsPbBr₃ and low I⁻ content is slightly retarded by I⁻ diffusion in the nanoplatelets, nonetheless, the 2D structure showed a higher capacity for I⁻ which we attributed to a higher stability against the lattice expansion during the halide exchange. We then designed an *in-situ* halide exchange reaction with as-synthesized concentration. With this method, we were able to monitor the structural changes during the reaction using XRD analysis, as well as the optical properties. Plus, it led to a near-complete halide exchange in CsPbBr₃ nanoplatelets by removing the released Br⁻ from solution. The halide exchange was also explored on a perovskite film made of the 2D CsPbBr₃ NPs. A uniform I-rich CsPbX₃ film was fabricated during the reaction, however Br and I species gradually segregated in the dynamic structure of the perovskite NPs resulting in Br-rich and I-rich sections on the film. This study provides a path to produce 2D CsPbI₃ NPs and insights into the structural changes during the halide exchange reaction of perovskite NPs.

Chapter 5 – Conclusion and Outlook

A fascination with CsPbX_3 nanoparticles and their unique optoelectronic properties inspired me to study, research and write this dissertation. The overarching goal of the dissertation is to describe the unique effect of a non-coordinating solvent such as benzyl ether (BE) along with the influence of microwave irradiation (MWI) on orientational growth of CsPbBr_3 nanoplatelets.

In chapter 1, the scope of the dissertation is outlined and a background pertaining to 2D all-inorganic NPs and content of the following chapters is established. First, we described the 2D CsPbX_3 NPs and their unique properties, such as, optoelectronic tunability by composition and size of the NPs. Then, we report on the factors affecting the synthesis of nanoplatelets and the most common synthesis techniques that lead to 2D growth in all-inorganic NPs including, ligand-assisted precipitation, hot injection, solvothermal synthesis and microwave-assisted synthesis. Halide exchange reactions of perovskite NPs is also summarized as it relates to chapter 4 of this dissertation.

In chapter 2, we described a microwave-based technique to synthesize 2-dimensional CsPbBr_3 perovskite nanoparticles in benzyl ether as a coordinating solvent. First, oleic acid (OAc) and oleyl amine (OAm) were employed to prepare two sets of precursors in BE: Cs^+ -OAc and PbBr_2 -OAm/OAc. Then a mixture of precursors with a $\text{Cs}^+:\text{PbBr}_2$ ratio of 1:3 was heated to 160 °C using MWI. The optical and structural properties of these nanoplatelets are demonstrated using UV-Vis spectroscopy, fluorescence spectroscopy, TEM, AFM, XRD, FTIR, ^1H -NMR and TGA. The nanoplatelets emitted a green light with the wavelength of 523 nm upon excitation. They had an average length of ~100 nm and up to 300 nm with a narrow thickness of ~ 4 nm. The XRD pattern matched precisely with a standard orthorhombic perovskite structure. Surface analysis

showed that a low organic content on the NP's surface is remained after several purification steps while BE marks in FTIR, ^1H -NMR and TGA analyses persisted stronger than the organic ligands. An important feature of the results was manifestation of the preferential growth perpendicular to (220) and (004) planes in the XRD. These XRD peaks were significantly stronger than others and therefore were selected as a signature of the 2D structure in different batches and experiments.

The growth mechanism from nuclei formation to thin nanoplatelets and post-synthesis modifications is discussed in chapter 3. A set of synthesis experiments were carried out to access the influence of BE as a coordinating solvent in our one-pot synthesis and the effect of MWI as the energy source in gradual heating of the medium. Synthetically, nucleation and growth were dependent on the polarity of the solvent used, which is shown to influence precursor/nuclei solubility, microwave absorption and heating rates, and coordination affinity to the CsPbX_3 interface. MWI was also proven to be crucial in the preferential growth of the nanoplatelets.

In chapter 4, halide exchange reaction of CsPbBr_3 nanoplatelets with PbI_2 was carried out to fabricate 2D CsPbI_3 NPs. Halide exchange reactions were monitored by red-shift of the PL emission as I^- replaces the Br^- in the nanostructure. A comparison between halide exchange reaction of nanoplatelets and nanocubes, showed a higher capacity of the nanoplatelets in accepting I^- at low concentrations which was attributed to the lower surface to volume ratio and lower surface energy of 2D CsPbBr_3 NPs. In addition, a detailed analysis of PL emission demonstrated that diluting the CsPbBr_3 nanoplatelets in toluene prior to the halide exchange resulted in quenching of the PL emission as well as blue-shift in the PL wavelength. Therefore, a modified *in-situ* halide exchange was applied to monitor the optical and structural changes during the reaction by microplate reader fluorescence spectroscopy and XRD. This method

facilitated a near-complete reaction which resulted in CsPbI₃ nanoplatelets with a red PL emission at 682 nm. Next, challenges of halide exchange on a film of CsPbBr₃ nanoplatelets are discussed in this chapter. While a halide exchange was displayed by red-shift of the PL emission and brown color of the film, the uniformity of the I-rich film did not last long and sections of BR-rich and I-rich CsPbX₃ appeared on the film after 4 days. Lastly, cyclic voltammetry of Br-rich and I-rich nanoplatelets was employed to quantify the electrochemical band gap of the NPs.

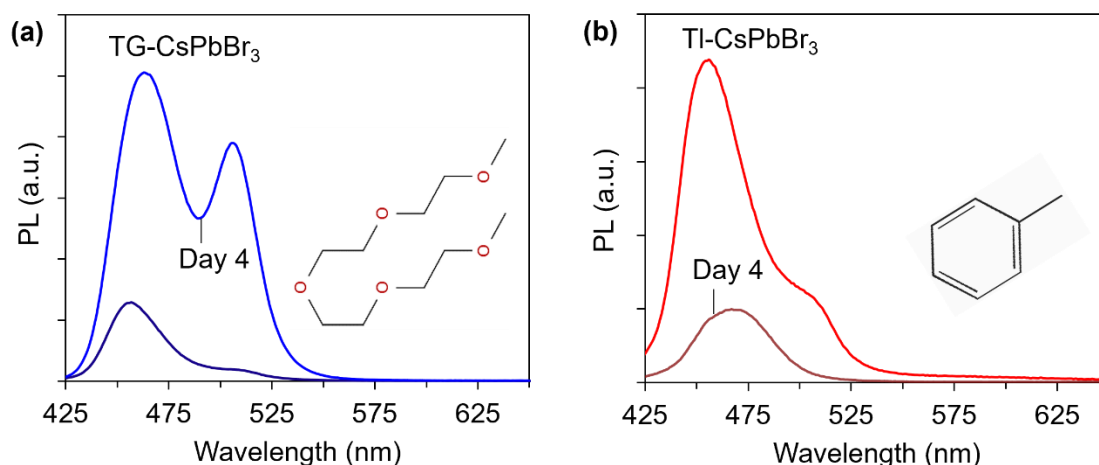


Figure 5.1. Photoluminescence spectra of CsPbBr₃ solution pre-treatment at room temperature in (a) tetraglyme (TG) and (b) toluene (TI) collected on the first and fourth day of the preparation.

There is a great opportunity to explore, implement or continue the findings of this dissertation to design and tailor perovskite nanoparticles for optoelectronic, sensing and catalysis applications. For instance, A MW synthesizer provides a dynamic environment to examine MW-based synthesis of perovskite NPs in various solvents. Preliminary studies showed CsPbBr₃ nuclei can form in various polar and nonpolar solvents such as tetraethylene glycol dimethyl ether (tetraglyme) and toluene at room temperature. The PL emission of the NPs after the synthesis

and 4 days later is shown in figure 5.1. Interestingly, PL intensity of the NPs in the more polar solvent, tetraglyme, increased over time. NPs are commonly dispersed in toluene, however toluene has a low boiling point which causes limits in the synthesis. With MW-based synthesis, a solvothermal process can be pursued due to control over pressure of the vial in a MW synthesizer. Another interesting avenue to follow based on this dissertation is fabricating larger nanoplatelets via pre- or post-synthesis modifications. Particularly, optimizing the concentration of precursors or ligands could lead to distinct NPs. The post-synthesis growth study in chapter 3 of this dissertation could be applied in discovering these possibilities. It is worth noting that using TEM and AFM microscopy could benefit the analyses tremendously. Considering the polydispersity of the CsPbBr₃ nanoplatelets in this study, it would also be beneficial to find a path to more uniform NPs.

Chapter 6 – References

- (1) Abramov, V. A.; Permogorov, S. A.; Razbirin, B. S.; Ekimov, A. I. Phonon-Assisted Exciton Annihilation in CdSe Crystals. *physica status solidi (b)* **1970**, 42 (2), 627–635. <https://doi.org/10.1002/pssb.19700420216>.
- (2) Rossetti, R.; Brus, L. *Electron-hole recombination emission as a probe of surface chemistry in aqueous cadmium sulfide colloids*. ACS Publications. <https://doi.org/10.1021/j100220a003>.
- (3) Reed, M. A.; Bate, R. T.; Bradshaw, K.; Duncan, W. M.; Frensley, W. R.; Lee, J. W.; Shih, H. D. Spatial Quantization in GaAs–AlGaAs Multiple Quantum Dots. *Journal of Vacuum Science & Technology B: Microelectronics Processing and Phenomena* **1986**, 4 (1), 358–360. <https://doi.org/10.1116/1.583331>.
- (4) Novoselov, K. S.; Geim, A. K.; Morozov, S. V.; Jiang, D.; Zhang, Y.; Dubonos, S. V.; Grigorieva, I. V.; Firsov, A. A. Electric Field Effect in Atomically Thin Carbon Films. *Science* **2004**, 306 (5696), 666–669. <https://doi.org/10.1126/science.1102896>.
- (5) Gupta, A.; Sakthivel, T.; Seal, S. Recent Development in 2D Materials beyond Graphene. *Progress in Materials Science* **2015**, 73, 44–126. <https://doi.org/10.1016/j.pmatsci.2015.02.002>.
- (6) Protesescu, L.; Yakunin, S.; Bodnarchuk, M. I.; Krieg, F.; Caputo, R.; Hendon, C. H.; Yang, R. X.; Walsh, A.; Kovalenko, M. V. Nanocrystals of Cesium Lead Halide Perovskites (CsPbX₃, X = Cl, Br, and I): Novel Optoelectronic Materials Showing Bright Emission with Wide Color Gamut. *Nano Lett.* **2015**, 15 (6), 3692–3696. <https://doi.org/10.1021/nl5048779>.
- (7) Naresh, V.; Kim, B. H.; Lee, N. Synthesis of CsPbX₃ (X = Cl/Br, Br, and Br/I)@SiO₂/PMMA Composite Films as Color-Conversion Materials for Achieving Tunable Multi-Color and White Light Emission. *Nano Res.* **2021**, 14 (4), 1187–1194. <https://doi.org/10.1007/s12274-020-3170-5>.
- (8) Lee, J.-W.; Dai, Z.; Han, T.-H.; Choi, C.; Chang, S.-Y.; Lee, S.-J.; Marco, N. D.; Zhao, H.; Sun, P.; Huang, Y.; Yang, Y. 2D Perovskite Stabilized Phase-Pure Formamidinium Perovskite Solar Cells. *Nature Communications* **2018**, 9 (1), 3021. <https://doi.org/10.1038/s41467-018-05454-4>.
- (9) Song, J.; Xu, L.; Li, J.; Xue, J.; Dong, Y.; Li, X.; Zeng, H. Monolayer and Few-Layer All-Inorganic Perovskites as a New Family of Two-Dimensional Semiconductors for Printable Optoelectronic Devices. *Advanced Materials* **2016**, 28 (24), 4861–4869. <https://doi.org/10.1002/adma.201600225>.
- (10) Liu, D.; Lin, Q.; Zang, Z.; Wang, M.; Wangyang, P.; Tang, X.; Zhou, M.; Hu, W. Flexible All-Inorganic Perovskite CsPbBr₃ Nonvolatile Memory Device. *ACS Applied Materials & Interfaces* **2017**, 9 (7), 6171–6176. <https://doi.org/10.1021/acsami.6b15149>.
- (11) Chen, S.; Shi, G. Two-Dimensional Materials for Halide Perovskite-Based Optoelectronic Devices. *Advanced Materials* **2017**, 29 (24), 1605448. <https://doi.org/10.1002/adma.201605448>.
- (12) Xu, X.; Wang, Z.; Yu, J.; Li, L.; Yan, X. Phase Engineering for Highly Efficient Quasi-Two-Dimensional All-Inorganic Perovskite Light-Emitting Diodes via Adjusting the Ratio of Cs Cation. *Nanoscale Res Lett* **2019**, 14 (1), 255. <https://doi.org/10.1186/s11671-019-3076-x>.
- (13) Chen, W.; Li, X.; Li, Y.; Li, Y. A Review: Crystal Growth for High-Performance All-Inorganic Perovskite Solar Cells. *Energy Environ. Sci.* **2020**, 13 (7), 1971–1996. <https://doi.org/10.1039/D0EE00215A>.
- (14) Ma, T.; Wang, S.; Zhang, Y.; Zhang, K.; Yi, L. The Development of All-Inorganic CsPbX₃ Perovskite Solar Cells. *J Mater Sci* **2020**, 55 (2), 464–479. <https://doi.org/10.1007/s10853-019-03974-y>.
- (15) K. Momma and F. Izumi. *VESTA 3 for Three-Dimensional Visualization of Crystal, Volumetric and Morphology Data*; 2011.

- (16) Bube, R. H. Electrons in Solids. In *Encyclopedia of Physical Science and Technology (Third Edition)*; Meyers, R. A., Ed.; Academic Press: New York, 2003; pp 307–329.
<https://doi.org/10.1016/B0-12-227410-5/00216-7>.
- (17) Chen, J.-S.; Doane, T. L.; Li, M.; Zang, H.; Maye, M. M.; Cotlet, M. Perovskite Nanomaterials: 0D–2D and 1D–2D Semiconductor Hybrids Composed of All Inorganic Perovskite Nanocrystals and Single-Layer Graphene with Improved Light Harvesting (Part. Part. Syst. Charact. 2/2018). *Particle & Particle Systems Characterization* **2018**, 35 (2), 1870006.
<https://doi.org/10.1002/ppsc.201870006>.
- (18) Tang, X.; Khurana, M.; Rossi, D.; Luo, L.; Akimov, A. V.; Son, D. H. Exciton Photoluminescence of Strongly Quantum-Confined Formamidinium Lead Bromide (FAPbBr₃) Quantum Dots. *J. Phys. Chem. C* **2022**, 126 (43), 18366–18373. <https://doi.org/10.1021/acs.jpcc.2c05661>.
- (19) Steele, J. A.; Lai, M.; Zhang, Y.; Lin, Z.; Hofkens, J.; Roeyffers, M. B. J.; Yang, P. Phase Transitions and Anion Exchange in All-Inorganic Halide Perovskites. *Acc. Mater. Res.* **2020**, 1 (1), 3–15.
<https://doi.org/10.1021/accountsmr.0c00009>.
- (20) Johnsson, M.; Lemmens, P. Crystallography and Chemistry of Perovskites. In *Handbook of Magnetism and Advanced Magnetic Materials*; Kronmüller, H., Parkin, S., Eds.; John Wiley & Sons, Ltd: Chichester, UK, 2007; p hmm411. <https://doi.org/10.1002/9780470022184.hmm411>.
- (21) Wang, B.; Navrotsky, A. Thermodynamics of Cesium Lead Halide (CsPbX₃, X = I, Br, Cl) Perovskites. *Thermochimica Acta* **2021**, 695, 178813.
<https://doi.org/10.1016/j.tca.2020.178813>.
- (22) Wang, Y.; Chen, Y.; Zhang, T.; Wang, X.; Zhao, Y. Chemically Stable Black Phase CsPbI₃ Inorganic Perovskites for High-Efficiency Photovoltaics. *Advanced Materials* **2020**, 32 (45), 2001025.
<https://doi.org/10.1002/adma.202001025>.
- (23) Linaburg, M. R.; McClure, E. T.; Majher, J. D.; Woodward, P. M. Cs₁–XRb_xPbCl₃ and Cs₁–XRb_xPbBr₃ Solid Solutions: Understanding Octahedral Tilting in Lead Halide Perovskites. *Chem. Mater.* **2017**, 29 (8), 3507–3514. <https://doi.org/10.1021/acs.chemmater.6b05372>.
- (24) Doane, T. L.; Ryan, K. L.; Pathade, L.; Cruz, K. J.; Zang, H.; Cotlet, M.; Maye, M. M. Using Perovskite Nanoparticles as Halide Reservoirs in Catalysis and as Spectrochemical Probes of Ions in Solution. *ACS Nano* **2016**, 10 (6), 5864–5872. <https://doi.org/10.1021/acsnano.6b00806>.
- (25) Li, Z.-J.; Hofman, E.; Davis, A. H.; Khammang, A.; Wright, J. T.; Dzikovski, B.; Meulenberg, R. W.; Zheng, W. Complete Dopant Substitution by Spinodal Decomposition in Mn-Doped Two-Dimensional CsPbCl₃ Nanoplatelets. *Chem. Mater.* **2018**, 30 (18), 6400–6409.
<https://doi.org/10.1021/acs.chemmater.8b02657>.
- (26) Zhou, X.; Zhao, Y.; Huang, W.; Wu, Y.; Wu, Z.; He, G. Enhanced Performance of Inverted CsPbBr₃ Nanocrystal LEDs via Zn(II) Doping. *Organic Electronics* **2021**, 96, 106253.
<https://doi.org/10.1016/j.orgel.2021.106253>.
- (27) Kim, H.; Bae, S.-R.; Lee, T. H.; Lee, H.; Kang, H.; Park, S.; Jang, H. W.; Kim, S. Y. Enhanced Optical Properties and Stability of CsPbBr₃ Nanocrystals Through Nickel Doping. *Advanced Functional Materials* **2021**, 31 (28), 2102770. <https://doi.org/10.1002/adfm.202102770>.
- (28) Yan, D.; Mo, Q.; Zhao, S.; Cai, W.; Zang, Z. Room Temperature Synthesis of Sn²⁺ Doped Highly Luminescent CsPbBr₃ Quantum Dots for High CRI White Light-Emitting Diodes. *Nanoscale* **2021**, 13 (21), 9740–9746. <https://doi.org/10.1039/D1NR01492G>.
- (29) Zheng, Y.; Yuan, X.; Yang, J.; Li, Q.; Yang, X.; Fan, Y.; Li, H.; Liu, H.; Zhao, J. Cu Doping-Enhanced Emission Efficiency of Mn²⁺ in Cesium Lead Halide Perovskite Nanocrystals for Efficient White Light-Emitting Diodes. *Journal of Luminescence* **2020**, 227, 117586.
<https://doi.org/10.1016/j.jlumin.2020.117586>.
- (30) Davis, A. H.; Li, S.; Lin, H.; Chu, C.; Franck, J. M.; Leem, G.; Maye, M. M.; Zheng, W. Ligand-Mediated Synthesis of Chemically Tailored Two-Dimensional All-Inorganic Perovskite

- Nanoplatelets Under Ambient Conditions. *J. Mater. Chem. C* **2021**.
<https://doi.org/10.1039/D1TC02931B>.
- (31) Ravi, V. K.; Markad, G. B.; Nag, A. Band Edge Energies and Excitonic Transition Probabilities of Colloidal CsPbX₃ (X = Cl, Br, I) Perovskite Nanocrystals. *ACS Energy Lett.* **2016**, *1* (4), 665–671.
<https://doi.org/10.1021/acseenergylett.6b00337>.
 - (32) Butler, K. T.; Frost, J. M.; Walsh, A. Band Alignment of the Hybrid Halide Perovskites CH₃NH₃PbCl₃, CH₃NH₃PbBr₃ and CH₃NH₃PbI₃. *Mater. Horiz.* **2015**, *2* (2), 228–231.
<https://doi.org/10.1039/C4MH00174E>.
 - (33) Umebayashi, T.; Asai, K.; Kondo, T.; Nakao, A. Electronic Structures of Lead Iodide Based Low-Dimensional Crystals. *Physical Review B* **2003**, *67*, 155405.
<https://doi.org/10.1103/PhysRevB.67.155405>.
 - (34) Filippetti, A.; Mattoni, A. Hybrid Perovskites for Photovoltaics: Insights from First Principles. *Phys. Rev. B* **2014**, *89* (12), 125203. <https://doi.org/10.1103/PhysRevB.89.125203>.
 - (35) Bryant, G. W. Excitons in Quantum Boxes: Correlation Effects and Quantum Confinement. *Phys. Rev. B* **1988**, *37* (15), 8763–8772. <https://doi.org/10.1103/PhysRevB.37.8763>.
 - (36) Agrawal, D. C. Introduction to Nanoscience and Nanomaterials. *MRS Bulletin* **2014**, *39* (10), 909–909. <https://doi.org/10.1557/mrs.2014.233>.
 - (37) Brennan, M. C.; Forde, A.; Zhukovskiy, M.; Baublis, A. J.; Morozov, Y. V.; Zhang, S.; Zhang, Z.; Kilin, D. S.; Kuno, M. Universal Size-Dependent Stokes Shifts in Lead Halide Perovskite Nanocrystals. *J. Phys. Chem. Lett.* **2020**, *11* (13), 4937–4944.
<https://doi.org/10.1021/acs.jpclett.0c01407>.
 - (38) Zhang, Z.; Zhang, S.; Gushchina, I.; Guo, T.; Brennan, M. C.; Pavlovets, I. M.; Grusenmeyer, T. A.; Kuno, M. Excitation Energy Dependence of Semiconductor Nanocrystal Emission Quantum Yields. *J. Phys. Chem. Lett.* **2021**, *12* (16), 4024–4031.
<https://doi.org/10.1021/acs.jpclett.1c00811>.
 - (39) VanWie, T.; Wysocki, E.; McBride, J. R.; Rosenthal, S. J. Bright Cool White Emission from Ultrasmall CdSe Quantum Dots. *Chem. Mater.* **2019**, *31* (20), 8558–8562.
<https://doi.org/10.1021/acs.chemmater.9b03718>.
 - (40) Pradhan, J.; Moitra, P.; Umesh; Das, B.; Mondal, P.; Kumar, G. S.; Ghorai, U. K.; Acharya, S.; Bhattacharya, S. Encapsulation of CsPbBr₃ Nanocrystals by a Tripodal Amine Markedly Improves Photoluminescence and Stability Concomitantly via Anion Defect Elimination. *Chem. Mater.* **2020**, *32* (17), 7159–7171. <https://doi.org/10.1021/acs.chemmater.0c00385>.
 - (41) Palazon, F.; El Ajjouri, Y.; Sebastia-Luna, P.; Lauciello, S.; Manna, L.; Bolink, H. J. Mechanochemical Synthesis of Inorganic Halide Perovskites: Evolution of Phase-Purity, Morphology, and Photoluminescence. *J. Mater. Chem. C* **2019**, *7* (37), 11406–11410.
<https://doi.org/10.1039/C9TC03778K>.
 - (42) Fichtner, J.; Watzele, S.; Garlyyev, B.; Kluge, R. M.; Haimerl, F.; El-Sayed, H. A.; Li, W.-J.; Maillard, F. M.; Dubau, L.; Chattot, R.; Michalička, J.; Macak, J. M.; Wang, W.; Wang, D.; Gigl, T.; Hugenschmidt, C.; Bandarenka, A. S. Tailoring the Oxygen Reduction Activity of Pt Nanoparticles through Surface Defects: A Simple Top-Down Approach. *ACS Catal.* **2020**, *10* (5), 3131–3142.
<https://doi.org/10.1021/acscatal.9b04974>.
 - (43) Pan, A.; He, B.; Fan, X.; Liu, Z.; Urban, J. J.; Alivisatos, A. P.; He, L.; Liu, Y. Insight into the Ligand-Mediated Synthesis of Colloidal CsPbBr₃ Perovskite Nanocrystals: The Role of Organic Acid, Base, and Cesium Precursors. *ACS Nano* **2016**, *10* (8), 7943–7954.
<https://doi.org/10.1021/acsnano.6b03863>.
 - (44) Wu, L.; Zhong, Q.; Yang, D.; Chen, M.; Hu, H.; Pan, Q.; Liu, H.; Cao, M.; Xu, Y.; Sun, B.; Zhang, Q. Improving the Stability and Size Tunability of Cesium Lead Halide Perovskite Nanocrystals Using

- Trioctylphosphine Oxide as the Capping Ligand. *Langmuir* **2017**, *33* (44), 12689–12696. <https://doi.org/10.1021/acs.langmuir.7b02963>.
- (45) Lian, X.; Wang, X.; Ling, Y.; Lochner, E.; Tan, L.; Zhou, Y.; Ma, B.; Hanson, K.; Gao, H. Light Emitting Diodes Based on Inorganic Composite Halide Perovskites. *Advanced Functional Materials* **2019**, *29* (5), 1807345. <https://doi.org/10.1002/adfm.201807345>.
- (46) Li, X.; Wu, Y.; Zhang, S.; Cai, B.; Gu, Y.; Song, J.; Zeng, H. CsPbX₃ Quantum Dots for Lighting and Displays: Room-Temperature Synthesis, Photoluminescence Superiorities, Underlying Origins and White Light-Emitting Diodes. *Advanced Functional Materials* **2016**, *26* (15), 2435–2445. <https://doi.org/10.1002/adfm.201600109>.
- (47) Kirakosyan, A.; Kim, Y.; Sihn, M. R.; Jeon, M.-G.; Jeong, J.-R.; Choi, J. Solubility-Controlled Room-Temperature Synthesis of Cesium Lead Halide Perovskite Nanocrystals. *ChemNanoMat* **2020**, *6* (12), 1863–1869. <https://doi.org/10.1002/cnma.202000471>.
- (48) Lu, C.; Wright, M. W.; Ma, X.; Li, H.; Itanze, D. S.; Carter, J. A.; Hewitt, C. A.; Donati, G. L.; Carroll, D. L.; Lundin, P. M.; Geyer, S. M. Cesium Oleate Precursor Preparation for Lead Halide Perovskite Nanocrystal Synthesis: The Influence of Excess Oleic Acid on Achieving Solubility, Conversion, and Reproducibility. *Chem. Mater.* **2019**, *31* (1), 62–67. <https://doi.org/10.1021/acs.chemmater.8b04876>.
- (49) Imran, M.; Caligiuri, V.; Wang, M.; Goldoni, L.; Prato, M.; Krahne, R.; De Trizio, L.; Manna, L. Benzoyl Halides as Alternative Precursors for the Colloidal Synthesis of Lead-Based Halide Perovskite Nanocrystals. *J. Am. Chem. Soc.* **2018**, *140* (7), 2656–2664. <https://doi.org/10.1021/jacs.7b13477>.
- (50) Grisorio, R.; Fanizza, E.; Striccoli, M.; Altamura, D.; Giannini, C.; Allegretta, I.; Terzano, R.; Suranna, G. P. Shape Tailoring of Iodine-Based Cesium Lead Halide Perovskite Nanocrystals in Hot-Injection Methods. *ChemNanoMat* **2020**, *6* (3), 356–361. <https://doi.org/10.1002/cnma.202000036>.
- (51) Bonato, L. G.; Moral, R. F.; Nagamine, G.; Alo, A.; Germino, J. C.; Silva, D. S. da; Almeida, D. B.; Zagonel, L. F.; Galembeck, F.; Padilha, L. A.; Nogueira, A. F. Revealing the Role of Tin(IV) Halides in the Anisotropic Growth of CsPbX₃ Perovskite Nanoplates. *Angewandte Chemie International Edition* **2020**, *59* (28), 11501–11509. <https://doi.org/10.1002/anie.202002641>.
- (52) Sun, S.; Yuan, D.; Xu, Y.; Wang, A.; Deng, Z. Ligand-Mediated Synthesis of Shape-Controlled Cesium Lead Halide Perovskite Nanocrystals *via* Reprecipitation Process at Room Temperature. *ACS Nano* **2016**, *10* (3), 3648–3657. <https://doi.org/10.1021/acsnano.5b08193>.
- (53) Do, M.; Kim, I.; Kolaczowski, M. A.; Kang, J.; Kamat, G. A.; Yuan, Z.; Barchi, N. S.; Wang, L.-W.; Liu, Y.; Jurow, M. J.; Sutter-Fella, C. M. Low-Dimensional Perovskite Nanoplatelet Synthesis Using *in Situ* Photophysical Monitoring to Establish Controlled Growth. *Nanoscale* **2019**, *11* (37), 17262–17269. <https://doi.org/10.1039/C9NR04010B>.
- (54) Peng, L.; Dutta, A.; Xie, R.; Yang, W.; Pradhan, N. Dot–Wire–Platelet–Cube: Step Growth and Structural Transformations in CsPbBr₃ Perovskite Nanocrystals. *ACS Energy Letters* **2018**, *3* (8), 2014–2020. <https://doi.org/10.1021/acsenenergylett.8b01037>.
- (55) Weidman, M. C.; Seitz, M.; Stranks, S. D.; Tisdale, W. A. Highly Tunable Colloidal Perovskite Nanoplatelets through Variable Cation, Metal, and Halide Composition. *ACS Nano* **2016**, *10* (8), 7830–7839. <https://doi.org/10.1021/acsnano.6b03496>.
- (56) Burlakov, V. M.; Hassan, Y.; Danaie, M.; Snaith, H. J.; Goriely, A. Competitive Nucleation Mechanism for CsPbBr₃ Perovskite Nanoplatelet Growth. *J. Phys. Chem. Lett.* **2020**, 6535–6543. <https://doi.org/10.1021/acs.jpcllett.0c01794>.
- (57) Yang, D.; Zou, Y.; Li, P.; Liu, Q.; Wu, L.; Hu, H.; Xu, Y.; Sun, B.; Zhang, Q.; Lee, S.-T. Large-Scale Synthesis of Ultrathin Cesium Lead Bromide Perovskite Nanoplates with Precisely Tunable

- Dimensions and Their Application in Blue Light-Emitting Diodes. *Nano Energy* **2018**, *47*, 235–242. <https://doi.org/10.1016/j.nanoen.2018.03.019>.
- (58) Scheidt, R. A.; Atwell, C.; Kamat, P. V. Tracking Transformative Transitions: From CsPbBr₃ Nanocrystals to Bulk Perovskite Films. *ACS Materials Lett.* **2019**, *1* (1), 8–13. <https://doi.org/10.1021/acsmaterialslett.9b00001>.
- (59) Tong, Y.; Bohn, B. J.; Bladt, E.; Wang, K.; Müller-Buschbaum, P.; Bals, S.; Urban, A. S.; Polavarapu, L.; Feldmann, J. From Precursor Powders to CsPbX₃ Perovskite Nanowires: One-Pot Synthesis, Growth Mechanism, and Oriented Self-Assembly. *Angewandte Chemie International Edition* **2017**, *56* (44), 13887–13892. <https://doi.org/10.1002/anie.201707224>.
- (60) Li, Z.-J.; Hofman, E.; Davis, A. H.; Maye, M. M.; Zheng, W. General Strategy for the Growth of CsPbX₃ (X = Cl, Br, I) Perovskite Nanosheets from the Assembly of Nanorods. *Chem. Mater.* **2018**, *30* (11), 3854–3860. <https://doi.org/10.1021/acs.chemmater.8b01283>.
- (61) Jeon, S.; Jung, M.-C.; Ahn, J.; Woo, H. K.; Bang, J.; Kim, D.; Lee, S. Y.; Woo, H. Y.; Jeon, J.; Han, M. J.; Paik, T.; Oh, S. J. Post-Synthetic Oriented Attachment of CsPbBr₃ Perovskite Nanocrystal Building Blocks: From First Principle Calculation to Experimental Demonstration of Size and Dimensionality (0D/1D/2D). *Nanoscale Horiz.* **2020**, *5* (6), 960–970. <https://doi.org/10.1039/D0NH00029A>.
- (62) Bekenstein, Y.; Koscher, B. A.; Eaton, S. W.; Yang, P.; Alivisatos, A. P. Highly Luminescent Colloidal Nanoplates of Perovskite Cesium Lead Halide and Their Oriented Assemblies. *J. Am. Chem. Soc.* **2015**, *137* (51), 16008–16011. <https://doi.org/10.1021/jacs.5b11199>.
- (63) Kovalenko, M. V.; Bodnarchuk, M. I. Lead Halide Perovskite Nanocrystals: From Discovery to Self-Assembly and Applications. *CHIMIA International Journal for Chemistry* **2017**, *71* (7–8), 461–470. <https://doi.org/10.2533/chimia.2017.461>.
- (64) Guo, J.; Ye, S.; Song, J.; Qu, J. Large-Scale Synthesis of Cesium Lead Halide Perovskite Nanocrystals for Zinc Ion Detection. *J Nanopart Res* **2020**, *22* (6), 153. <https://doi.org/10.1007/s11051-020-04887-7>.
- (65) Kang, T. W.; Lee, S.; Park, Y. J.; Jeong, G. J.; Jeong, G. J.; Kim, J. S.; Bae, B.; Bae, B.; Hwang, J.; Hwang, J.; Kim, S. W. Enhancement of the Optical Properties of CsPbBr₃ Perovskite Nanocrystals Using Three Different Solvents. *Opt. Lett., OL* **2020**, *45* (18), 4972–4975. <https://doi.org/10.1364/OL.401058>.
- (66) Dey, A.; Ye, J.; De, A.; Debroye, E.; Ha, S. K.; Bladt, E.; Kshirsagar, A. S.; Wang, Z.; Yin, J.; Wang, Y.; Quan, L. N.; Yan, F.; Gao, M.; Li, X.; Shamsi, J.; Debnath, T.; Cao, M.; Scheel, M. A.; Kumar, S.; Steele, J. A.; Gerhard, M.; Chouhan, L.; Xu, K.; Wu, X.; Li, Y.; Zhang, Y.; Dutta, A.; Han, C.; Vincon, I.; Rogach, A. L.; Nag, A.; Samanta, A.; Korgel, B. A.; Shih, C.-J.; Gamelin, D. R.; Son, D. H.; Zeng, H.; Zhong, H.; Sun, H.; Demir, H. V.; Scheblykin, I. G.; Mora-Seró, I.; Stolarczyk, J. K.; Zhang, J. Z.; Feldmann, J.; Hofkens, J.; Luther, J. M.; Pérez-Prieto, J.; Li, L.; Manna, L.; Bodnarchuk, M. I.; Kovalenko, M. V.; Roelofs, M. B. J.; Pradhan, N.; Mohammed, O. F.; Bakr, O. M.; Yang, P.; Müller-Buschbaum, P.; Kamat, P. V.; Bao, Q.; Zhang, Q.; Krahne, R.; Galian, R. E.; Stranks, S. D.; Bals, S.; Biju, V.; Tisdale, W. A.; Yan, Y.; Hoyer, R. L. Z.; Polavarapu, L. State of the Art and Prospects for Halide Perovskite Nanocrystals. *ACS Nano* **2021**, *acs.nano.0c08903*. <https://doi.org/10.1021/acsnano.0c08903>.
- (67) Huang, H.; Li, Y.; Tong, Y.; Yao, E.-P.; Feil, M. W.; Richter, A. F.; Döblinger, M.; Rogach, A. L.; Feldmann, J.; Polavarapu, L. Spontaneous Crystallization of Perovskite Nanocrystals in Nonpolar Organic Solvents: A Versatile Approach for Their Shape-Controlled Synthesis. *Angewandte Chemie International Edition* **2019**, *58* (46), 16558–16562. <https://doi.org/10.1002/anie.201906862>.

- (68) Ng, C. K.; Yin, W.; Li, H.; Jasieniak, J. J. Scalable Synthesis of Colloidal CsPbBr₃ Perovskite Nanocrystals with High Reaction Yields through Solvent and Ligand Engineering. *Nanoscale* **2020**, *12* (8), 4859–4867. <https://doi.org/10.1039/C9NR10726F>.
- (69) Hamill, J. C.; Schwartz, J.; Loo, Y.-L. Influence of Solvent Coordination on Hybrid Organic–Inorganic Perovskite Formation. *ACS Energy Lett.* **2018**, *3* (1), 92–97. <https://doi.org/10.1021/acsenergylett.7b01057>.
- (70) Cinquino, M.; Polimeno, L.; Lerario, G.; De Giorgi, M.; Moliterni, A.; Olieric, V.; Fieramosca, A.; Carallo, S.; Mastria, R.; Ardizzone, V.; Dominici, L.; Ballarini, D.; Giannini, C.; Sanvitto, D.; Rizzo, A.; De Marco, L. One-Step Synthesis at Room Temperature of Low Dimensional Perovskite Single Crystals with High Optical Quality. *Journal of Luminescence* **2020**, *221*, 117079. <https://doi.org/10.1016/j.jlumin.2020.117079>.
- (71) Manser, J. S.; Saidaminov, M. I.; Christians, J. A.; Bakr, O. M.; Kamat, P. V. Making and Breaking of Lead Halide Perovskites. *Acc. Chem. Res.* **2016**, *49* (2), 330–338. <https://doi.org/10.1021/acs.accounts.5b00455>.
- (72) Sun, J.-K.; Huang, S.; Liu, X.-Z.; Xu, Q.; Zhang, Q.-H.; Jiang, W.-J.; Xue, D.-J.; Xu, J.-C.; Ma, J.-Y.; Ding, J.; Ge, Q.-Q.; Gu, L.; Fang, X.-H.; Zhong, H.-Z.; Hu, J.-S.; Wan, L.-J. Polar Solvent Induced Lattice Distortion of Cubic CsPbI₃ Nanocubes and Hierarchical Self-Assembly into Orthorhombic Single-Crystalline Nanowires. *J. Am. Chem. Soc.* **2018**, *140* (37), 11705–11715. <https://doi.org/10.1021/jacs.8b05949>.
- (73) Swarnkar, A.; Marshall, A. R.; Sanehira, E. M.; Chernomordik, B. D.; Moore, D. T.; Christians, J. A.; Chakrabarti, T.; Luther, J. M. Quantum Dot–Induced Phase Stabilization of α -CsPbI₃ Perovskite for High-Efficiency Photovoltaics. *Science* **2016**, *354* (6308), 92–95. <https://doi.org/10.1126/science.aag2700>.
- (74) Schmidt, L. C.; Pertegás, A.; González-Carrero, S.; Malinkiewicz, O.; Agouram, S.; Mínguez Espallargas, G.; Bolink, H. J.; Galian, R. E.; Pérez-Prieto, J. Nontemplate Synthesis of CH₃NH₃PbBr₃ Perovskite Nanoparticles. *J. Am. Chem. Soc.* **2014**, *136* (3), 850–853. <https://doi.org/10.1021/ja4109209>.
- (75) Zhang, F.; Zhong, H.; Chen, C.; Wu, X.; Hu, X.; Huang, H.; Han, J.; Zou, B.; Dong, Y. Brightly Luminescent and Color-Tunable Colloidal CH₃NH₃PbX₃ (X = Br, I, Cl) Quantum Dots: Potential Alternatives for Display Technology. *ACS Nano* **2015**, *9* (4), 4533–4542. <https://doi.org/10.1021/acsnano.5b01154>.
- (76) Sichert, J. A.; Tong, Y.; Mutz, N.; Vollmer, M.; Fischer, S.; Milowska, K. Z.; García Cortadella, R.; Nickel, B.; Cardenas-Daw, C.; Stolarczyk, J. K.; Urban, A. S.; Feldmann, J. Quantum Size Effect in Organometal Halide Perovskite Nanoplatelets. *Nano Lett.* **2015**, *15* (10), 6521–6527. <https://doi.org/10.1021/acs.nanolett.5b02985>.
- (77) Tyagi, P.; Arveson, S. M.; Tisdale, W. A. Colloidal Organohalide Perovskite Nanoplatelets Exhibiting Quantum Confinement. *J. Phys. Chem. Lett.* **2015**, *6* (10), 1911–1916. <https://doi.org/10.1021/acs.jpcllett.5b00664>.
- (78) Akkerman, Q. A.; Motti, S. G.; Srimath Kandada, A. R.; Mosconi, E.; D’Innocenzo, V.; Bertoni, G.; Marras, S.; Kamino, B. A.; Miranda, L.; De Angelis, F.; Petrozza, A.; Prato, M.; Manna, L. Solution Synthesis Approach to Colloidal Cesium Lead Halide Perovskite Nanoplatelets with Monolayer-Level Thickness Control. *J. Am. Chem. Soc.* **2016**, *138* (3), 1010–1016. <https://doi.org/10.1021/jacs.5b12124>.
- (79) Ha, S. K.; Tisdale, W. A. Facile Synthesis of Colloidal Lead Halide Perovskite Nanoplatelets via Ligand-Assisted Reprecipitation. *JoVE* **2019**, No. 152, 60114. <https://doi.org/10.3791/60114>.
- (80) Murray, C. B.; Norris, D. J.; Bawendi, M. G. Synthesis and Characterization of Nearly Monodisperse CdE (E = Sulfur, Selenium, Tellurium) Semiconductor Nanocrystallites. *J. Am. Chem. Soc.* **1993**, *115* (19), 8706–8715. <https://doi.org/10.1021/ja00072a025>.

- (81) Wei, H.; Guo, W.; Sun, Y.; Yang, Z.; Zhang, Y. Hot-Injection Synthesis and Characterization of Quaternary Cu₂ZnSnSe₄ Nanocrystals. *Materials Letters* **2010**, *64* (13), 1424–1426. <https://doi.org/10.1016/j.matlet.2010.03.034>.
- (82) Ou, K.-L.; Fan, J.-C.; Chen, J.-K.; Huang, C.-C.; Chen, L.-Y.; Ho, J.-H.; Chang, J.-Y. Hot-Injection Synthesis of Monodispersed Cu₂ZnSn(S_xSe_{1-x})₄ Nanocrystals: Tunable Composition and Optical Properties. *J. Mater. Chem.* **2012**, *22* (29), 14667–14673. <https://doi.org/10.1039/C2JM31901B>.
- (83) Abe, S.; Capek, R. K.; De Geyter, B.; Hens, Z. Reaction Chemistry/Nanocrystal Property Relations in the Hot Injection Synthesis, the Role of the Solute Solubility. *ACS Nano* **2013**, *7* (2), 943–949. <https://doi.org/10.1021/nn3059168>.
- (84) Shamsi, J.; Dang, Z.; Bianchini, P.; Canale, C.; Di Stasio, F.; Brescia, R.; Prato, M.; Manna, L. Colloidal Synthesis of Quantum Confined Single Crystal CsPbBr₃ Nanosheets with Lateral Size Control up to the Micrometer Range. *J. Am. Chem. Soc.* **2016**, *138* (23), 7240–7243. <https://doi.org/10.1021/jacs.6b03166>.
- (85) Chen, M.; Zou, Y.; Wu, L.; Pan, Q.; Yang, D.; Hu, H.; Tan, Y.; Zhong, Q.; Xu, Y.; Liu, H.; Sun, B.; Zhang, Q. Solvothermal Synthesis of High-Quality All-Inorganic Cesium Lead Halide Perovskite Nanocrystals: From Nanocube to Ultrathin Nanowire. *Advanced Functional Materials* **2017**, *27* (23), 1701121. <https://doi.org/10.1002/adfm.201701121>.
- (86) Zhai, W.; Lin, J.; Li, Q.; Zheng, K.; Huang, Y.; Yao, Y.; He, X.; Li, L.; Yu, C.; Liu, C.; Fang, Y.; Liu, Z.; Tang, C. Solvothermal Synthesis of Ultrathin Cesium Lead Halide Perovskite Nanoplatelets with Tunable Lateral Sizes and Their Reversible Transformation into Cs₄PbBr₆ Nanocrystals. *Chemistry of Materials* **2018**, *30* (11), 3714–3721. <https://doi.org/10.1021/acs.chemmater.8b00612>.
- (87) Han, H.; Francesco, G. D.; Maye, M. M. Size Control and Photophysical Properties of Quantum Dots Prepared via a Novel Tunable Hydrothermal Route. *J. Phys. Chem. C* **2010**, *114* (45), 19270–19277. <https://doi.org/10.1021/jp107702b>.
- (88) Njoki, P. N.; Wu, W.; Lutz, P.; Maye, M. M. Growth Characteristics and Optical Properties of Core/Alloy Nanoparticles Fabricated via the Layer-by-Layer Hydrothermal Route. *Chemistry of Materials* **2013**, *25* (15), 3105–3113. <https://doi.org/10.1021/cm401286w>.
- (89) Maye, M.; Njoki, P.; Wu, W.; Han, H. System and Method for Synthesizing Core/Alloy Nanostructures. US20120114962A1, May 10, 2012. <https://patents.google.com/patent/US20120114962A1/en> (accessed 2019-02-26).
- (90) Wu, W.; Njoki, P. N.; Han, H.; Zhao, H.; Schiff, E. A.; Lutz, P. S.; Solomon, L.; Matthews, S.; Maye, M. M. Processing Core/Alloy/Shell Nanoparticles: Tunable Optical Properties and Evidence for Self-Limiting Alloy Growth. *J. Phys. Chem. C* **2011**, *115* (20), 9933–9942. <https://doi.org/10.1021/jp201151m>.
- (91) Yazdanparast, M. S.; McLaurin, E. J. Microwave-Assisted Synthesis and Assembly of Hyperbranched Supra Quantum Dot CdE (E = S, Se, Te) Nanocrystals. *Crystal Growth & Design* **2020**, *20* (3), 1442–1450. <https://doi.org/10.1021/acs.cgd.9b01007>.
- (92) Baghbanzadeh, M.; Carbone, L.; Cozzoli, P. D.; Kappe, C. O. Microwave-Assisted Synthesis of Colloidal Inorganic Nanocrystals. *Angewandte Chemie International Edition* **2011**, *50* (48), 11312–11359. <https://doi.org/10.1002/anie.201101274>.
- (93) Liu, W.; Zheng, J.; Cao, S.; Wang, L.; Gao, F.; Chou, K.-C.; Hou, X.; Yang, W. General Strategy for Rapid Production of Low-Dimensional All-Inorganic CsPbBr₃ Perovskite Nanocrystals with Controlled Dimensionalities and Sizes. *Inorg. Chem.* **2018**, *57* (3), 1598–1603. <https://doi.org/10.1021/acs.inorgchem.7b02941>.
- (94) Washington II, A. L.; Strouse, G. F. Microwave Synthesis of CdSe and CdTe Nanocrystals in Nonabsorbing Alkanes. *J. Am. Chem. Soc.* **2008**, *130* (28), 8916–8922. <https://doi.org/10.1021/ja711115r>.

- (95) Pan, Q.; Hu, H.; Zou, Y.; Chen, M.; Wu, L.; Yang, D.; Yuan, X.; Fan, J.; Sun, B.; Zhang, Q. Microwave-Assisted Synthesis of High-Quality “All-Inorganic” CsPbX₃ (X = Cl, Br, I) Perovskite Nanocrystals and Their Application in Light Emitting Diodes. *J. Mater. Chem. C* **2017**, *5* (42), 10947–10954. <https://doi.org/10.1039/C7TC03774K>.
- (96) Long, Z.; Ren, H.; Sun, J.; Ouyang, J.; Na, N. High-Throughput and Tunable Synthesis of Colloidal CsPbX₃ Perovskite Nanocrystals in a Heterogeneous System by Microwave Irradiation. *Chemical Communications* **2017**, *53* (71), 9914–9917. <https://doi.org/10.1039/C7CC04862A>.
- (97) Shamsi, J.; Rastogi, P.; Caligiuri, V.; Abdelhady, A. L.; Spirito, D.; Manna, L.; Krahne, R. Bright-Emitting Perovskite Films by Large-Scale Synthesis and Photoinduced Solid-State Transformation of CsPbBr₃ Nanoplatelets. *ACS Nano* **2017**, *11* (10), 10206–10213. <https://doi.org/10.1021/acsnano.7b04761>.
- (98) Gabriel, C.; Gabriel, S.; H. Grant, E.; H. Grant, E.; S. J. Halstead, B.; Michael P. Mingos, D. Dielectric Parameters Relevant to Microwave Dielectric Heating. *Chem. Soc. Rev.* **1998**, *27* (3), 213. <https://doi.org/10.1039/a827213z>.
- (99) Khan, N. R.; Rathod, V. K. Microwave Assisted Enzymatic Synthesis of Speciality Esters: A Mini - Review. *Process Biochemistry* **2018**, *75*, 89–98. <https://doi.org/10.1016/j.procbio.2018.08.019>.
- (100) Kappe, C. O. Controlled Microwave Heating in Modern Organic Synthesis. *Angewandte Chemie International Edition* **2004**, *43* (46), 6250–6284. <https://doi.org/10.1002/anie.200400655>.
- (101) Rao, L.; Tang, Y.; Song, C.; Xu, K.; Vickers, E. T.; Bonabi Naghadeh, S.; Ding, X.; Li, Z.; Zhang, J. Z. Polar-Solvent-Free Synthesis of Highly Photoluminescent and Stable CsPbBr₃ Nanocrystals with Controlled Shape and Size by Ultrasonication. *Chem. Mater.* **2019**, *31* (2), 365–375. <https://doi.org/10.1021/acs.chemmater.8b03298>.
- (102) Hossain, M. K.; Guo, P.; Qarony, W.; Tsang, Y. H.; Liu, C.; Tsang, S. W.; Ho, J. C.; Yu, K. M. Controllable Optical Emission Wavelength in All-Inorganic Halide Perovskite Alloy Microplates Grown by Two-Step Chemical Vapor Deposition. *Nano Res.* **2020**, *13* (11), 2939–2949. <https://doi.org/10.1007/s12274-020-2951-1>.
- (103) Nedelcu, G.; Protesescu, L.; Yakunin, S.; Bodnarchuk, M. I.; Grotevent, M. J.; Kovalenko, M. V. Fast Anion-Exchange in Highly Luminescent Nanocrystals of Cesium Lead Halide Perovskites (CsPbX₃, X = Cl, Br, I). *Nano Lett.* **2015**, *15* (8), 5635–5640. <https://doi.org/10.1021/acs.nanolett.5b02404>.
- (104) Uddin, M. A.; Calabro, R. L.; Kim, D.-Y.; Graham, K. R. Halide Exchange and Surface Modification of Metal Halide Perovskite Nanocrystals with Alkyltrichlorosilanes. *Nanoscale* **2018**, *10* (35), 16919–16927. <https://doi.org/10.1039/C8NR04763D>.
- (105) Dutt, V. G. V.; Akhil, S.; Mishra, N. Fast, Tunable and Reversible Anion-Exchange in CsPbBr₃ Perovskite Nanocrystals with Hydrohalic Acids. *CrystEngComm* **2020**, *22* (30), 5022–5030. <https://doi.org/10.1039/D0CE00722F>.
- (106) Yan, A.; Guo, Y.; Liu, C.; Deng, Z.; Guo, Y.; Zhao, X. Tuning the Optical Properties of CsPbBr₃ Nanocrystals by Anion Exchange Reactions with CsX Aqueous Solution. *Nanoscale Research Letters* **2018**, *13* (1), 185. <https://doi.org/10.1186/s11671-018-2592-4>.
- (107) Akkerman, Q. A.; D’Innocenzo, V.; Accornero, S.; Scarpellini, A.; Petrozza, A.; Prato, M.; Manna, L. Tuning the Optical Properties of Cesium Lead Halide Perovskite Nanocrystals by Anion Exchange Reactions. *J. Am. Chem. Soc.* **2015**, *137* (32), 10276–10281. <https://doi.org/10.1021/jacs.5b05602>.
- (108) Ripka, E. G.; Deschene, C. R.; Franck, J. M.; Bae, I.-T.; Maye, M. M. Understanding the Surface Properties of Halide Exchanged Cesium Lead Halide Nanoparticles. *Langmuir* **2018**, *34* (37), 11139–11146. <https://doi.org/10.1021/acs.langmuir.8b02148>.
- (109) Yin, W.; Li, H.; Chesman, A. S. R.; Tadgell, B.; Scully, A. D.; Wang, M.; Huang, W.; McNeill, C. R.; Wong, W. W. H.; Medhekar, N. V.; Mulvaney, P.; Jasieniak, J. J. Detection of Halomethanes

- Using Cesium Lead Halide Perovskite Nanocrystals. *ACS Nano* **2021**, *15* (1), 1454–1464. <https://doi.org/10.1021/acsnano.0c08794>.
- (110) Ahmad, W.; Khan, J.; Niu, G.; Tang, J. Inorganic CsPbI₃ Perovskite-Based Solar Cells: A Choice for a Tandem Device. *Solar RRL* **2017**, *1* (7), 1700048. <https://doi.org/10.1002/solr.201700048>.
- (111) Zhang, Z.; Li, Z.; Meng, L.; Lien, S.-Y.; Gao, P. Perovskite-Based Tandem Solar Cells: Get the Most Out of the Sun. *Advanced Functional Materials* **2020**, *30* (38), 2001904. <https://doi.org/10.1002/adfm.202001904>.
- (112) Thomas, C. J.; Zhang, Y.; Guillaussier, A.; Bdeir, K.; Aly, O. F.; Kim, H. G.; Noh, J.; Reimnitz, L. C.; Li, J.; Deepak, F. L.; Smilgies, D.-M.; Milliron, D. J.; Korgel, B. A. Thermal Stability of the Black Perovskite Phase in Cesium Lead Iodide Nanocrystals Under Humid Conditions. *Chem. Mater.* **2019**, *31* (23), 9750–9758. <https://doi.org/10.1021/acs.chemmater.9b03533>.
- (113) Liu, X.; Cao, L.; Guo, Z.; Li, Y.; Gao, W.; Zhou, L. A Review of Perovskite Photovoltaic Materials' Synthesis and Applications via Chemical Vapor Deposition Method. *Materials* **2019**, *12* (20), 3304. <https://doi.org/10.3390/ma12203304>.
- (114) Hoffman, J. B.; Zaiats, G.; Wappes, I.; Kamat, P. V. CsPbBr₃ Solar Cells: Controlled Film Growth through Layer-by-Layer Quantum Dot Deposition. *Chem. Mater.* **2017**, *29* (22), 9767–9774. <https://doi.org/10.1021/acs.chemmater.7b03751>.
- (115) Weidman, M. C.; Goodman, A. J.; Tisdale, W. A. Colloidal Halide Perovskite Nanoplatelets: An Exciting New Class of Semiconductor Nanomaterials. *Chemistry of Materials* **2017**, *29* (12), 5019–5030. <https://doi.org/10.1021/acs.chemmater.7b01384>.
- (116) Hoffman, J. B.; Schleper, A. L.; Kamat, P. V. Transformation of Sintered CsPbBr₃ Nanocrystals to Cubic CsPbI₃ and Gradient CsPbBr_{1-x}I_{3-x} through Halide Exchange. *J. Am. Chem. Soc.* **2016**, *138* (27), 8603–8611. <https://doi.org/10.1021/jacs.6b04661>.
- (117) Ha, S.-T.; Su, R.; Xing, J.; Zhang, Q.; Xiong, Q. Metal Halide Perovskite Nanomaterials: Synthesis and Applications. *Chem. Sci.* **2017**, *8* (4), 2522–2536. <https://doi.org/10.1039/C6SC04474C>.
- (118) Zhang, Y.; Lu, D.; Gao, M.; Lai, M.; Lin, J.; Lei, T.; Lin, Z.; Quan, L. N.; Yang, P. Quantitative Imaging of Anion Exchange Kinetics in Halide Perovskites. *Proc Natl Acad Sci USA* **2019**, *116* (26), 12648–12653. <https://doi.org/10.1073/pnas.1903448116>.
- (119) Kojima, A.; Teshima, K.; Shirai, Y.; Miyasaka, T. Organometal Halide Perovskites as Visible-Light Sensitizers for Photovoltaic Cells. *J. Am. Chem. Soc.* **2009**, *131* (17), 6050–6051. <https://doi.org/10.1021/ja809598r>.
- (120) Yoo, J. J.; Seo, G.; Chua, M. R.; Park, T. G.; Lu, Y.; Rotermund, F.; Kim, Y.-K.; Moon, C. S.; Jeon, N. J.; Correa-Baena, J.-P.; Bulović, V.; Shin, S. S.; Bawendi, M. G.; Seo, J. Efficient Perovskite Solar Cells via Improved Carrier Management. *Nature* **2021**, *590* (7847), 587–593. <https://doi.org/10.1038/s41586-021-03285-w>.
- (121) Kuang, Y.; Ma, Y.; Zhang, D.; Wei, Q.; Wang, S.; Yang, X.; Hong, X.; Liu, Y. Enhanced Optical Absorption in Perovskite/Si Tandem Solar Cells with Nanoholes Array. *Nanoscale Research Letters* **2020**, *15* (1), 213. <https://doi.org/10.1186/s11671-020-03445-3>.
- (122) Zhang, P.; Zhu, G.; Shi, Y.; Wang, Y.; Zhang, J.; Du, L.; Ding, D. Ultrafast Interfacial Charge Transfer of Cesium Lead Halide Perovskite Films CsPbX₃ (X = Cl, Br, I) with Different Halogen Mixing. *J. Phys. Chem. C* **2018**, *122* (48), 27148–27155. <https://doi.org/10.1021/acs.jpcc.8b07237>.
- (123) Zou, W.; Li, R.; Zhang, S.; Liu, Y.; Wang, N.; Cao, Y.; Miao, Y.; Xu, M.; Guo, Q.; Di, D.; Zhang, L.; Yi, C.; Gao, F.; Friend, R. H.; Wang, J.; Huang, W. Minimising Efficiency Roll-off in High-Brightness Perovskite Light-Emitting Diodes. *Nature Communications* **2018**, *9* (1), 608. <https://doi.org/10.1038/s41467-018-03049-7>.
- (124) Pramanik, A.; Patibandla, S.; Gao, Y.; Gates, K.; Ray, P. C. Water Triggered Synthesis of Highly Stable and Biocompatible 1D Nanowire, 2D Nanoplatelet, and 3D Nanocube CsPbBr₃

- Perovskites for Multicolor Two-Photon Cell Imaging. *JACS Au* **2021**, 1 (1), 53–65.
<https://doi.org/10.1021/jacsau.0c00038>.
- (125) Liu, Y.; Wang, J.; Han, S.; Liu, X.; Li, M.; Xu, Z.; Guo, W.; Hong, M.; Luo, J.; Sun, Z. Multilayered 2D Cesium-Based Hybrid Perovskite with Strong Polarization Sensitivity: Dimensional Reduction of CsPbBr₃. *Chemistry – A European Journal* **2020**, 26 (16), 3494–3498.
<https://doi.org/10.1002/chem.201905531>.
- (126) Chen, K.; Wang, Y.; Liu, J.; Kang, J.; Ge, Y.; Huang, W.; Lin, Z.; Guo, Z.; Zhang, Y.; Zhang, H. In Situ Preparation of a CsPbBr₃/Black Phosphorus Heterostructure with an Optimized Interface and Photodetector Application. *Nanoscale* **2019**, 11 (36), 16852–16859.
<https://doi.org/10.1039/C9NR06488E>.
- (127) Wang, T.; Yang, W.; Li, B.; Bian, R.; Jia, X.; Yu, H.; Wang, L.; Li, X.; Xie, F.; Zhu, H.; Yang, J.; Gao, Y.; Zhou, Q.; He, C.; Liu, X.; Ye, Y. Radiation-Resistant CsPbBr₃ Nanoplate-Based Lasers. *ACS Appl. Nano Mater.* **2020**, 3 (12), 12017–12024. <https://doi.org/10.1021/acsanm.0c02543>.
- (128) Li, H.; Luo, T.; Zhang, S.; Sun, Z.; He, X.; Zhang, W.; Chang, H. Two-Dimensional Metal-Halide Perovskite-Based Optoelectronics: Synthesis, Structure, Properties and Applications. *ENERGY & ENVIRONMENTAL MATERIALS* **2021**, 4 (1), 46–64. <https://doi.org/10.1002/eem2.12087>.
- (129) Chen, N.; Bai, Z.; Wang, Z.; Ji, H.; Liu, R.; Cao, C.; Wang, H.; Jiang, F.; Zhong, H. P-119: Low Cost Perovskite Quantum Dots Film Based Wide Color Gamut Backlight Unit for LCD TVs. *SID Symposium Digest of Technical Papers* **2018**, 49 (1), 1657–1659.
<https://doi.org/10.1002/sdtp.12303>.
- (130) Chen, Y.; Liu, X.; Zhao, Y. Organic Matrix Assisted Low-temperature Crystallization of Black Phase Inorganic Perovskites. *Angewandte Chemie Intl Edit* **2022**, 61 (1).
<https://doi.org/10.1002/anie.202110603>.
- (131) Chen, Y.; Liu, X.; Wang, T.; Zhao, Y. Highly Stable Inorganic Lead Halide Perovskite toward Efficient Photovoltaics. *Acc. Chem. Res.* **2021**, 54 (17), 3452–3461.
<https://doi.org/10.1021/acs.accounts.1c00343>.
- (132) Liu, W.; Zheng, J.; Cao, S.; Wang, L.; Gao, F.; Chou, K.-C.; Hou, X.; Yang, W. General Strategy for Rapid Production of Low-Dimensional All-Inorganic CsPbBr₃ Perovskite Nanocrystals with Controlled Dimensionalities and Sizes. *Inorg. Chem.* **2018**, 57 (3), 1598–1603.
<https://doi.org/10.1021/acs.inorgchem.7b02941>.
- (133) Pradhan, N. Alkylammonium Halides for Facet Reconstruction and Shape Modulation in Lead Halide Perovskite Nanocrystals. *Acc. Chem. Res.* **2021**, 54 (5), 1200–1208.
<https://doi.org/10.1021/acs.accounts.0c00708>.
- (134) Pradhan, N. Journey of Making Cesium Lead Halide Perovskite Nanocrystals: What's Next. *J. Phys. Chem. Lett.* **2019**, 10 (19), 5847–5855. <https://doi.org/10.1021/acs.jpcllett.9b02412>.
- (135) Zhang, Y.; Siegler, T. D.; Thomas, C. J.; Abney, M. K.; Shah, T.; De Gorostiza, A.; Greene, R. M.; Korgel, B. A. A “Tips and Tricks” Practical Guide to the Synthesis of Metal Halide Perovskite Nanocrystals. *Chem. Mater.* **2020**, 32 (13), 5410–5423.
<https://doi.org/10.1021/acs.chemmater.0c01735>.
- (136) Hintermayr, V. A.; Polavarapu, L.; Urban, A. S.; Feldmann, J. Accelerated Carrier Relaxation through Reduced Coulomb Screening in Two-Dimensional Halide Perovskite Nanoplatelets. *ACS Nano* **2018**, 12 (10), 10151–10158. <https://doi.org/10.1021/acs.nano.8b05029>.
- (137) Almeida, G.; Goldoni, L.; Akkerman, Q.; Dang, Z.; Khan, A. H.; Marras, S.; Moreels, I.; Manna, L. Role of Acid–Base Equilibria in the Size, Shape, and Phase Control of Cesium Lead Bromide Nanocrystals. *ACS Nano* **2018**, 12 (2), 1704–1711. <https://doi.org/10.1021/acs.nano.7b08357>.
- (138) Ahmed, G. H.; Yin, J.; Bose, R.; Sinatra, L.; Alarousu, E.; Yengel, E.; AlYami, N. M.; Saidaminov, M. I.; Zhang, Y.; Hedhili, M. N.; Bakr, O. M.; Brédas, J.-L.; Mohammed, O. F. Pyridine-Induced

- Dimensionality Change in Hybrid Perovskite Nanocrystals. *Chem. Mater.* **2017**, *29* (10), 4393–4400. <https://doi.org/10.1021/acs.chemmater.7b00872>.
- (139) Liang, Z.; Zhao, S.; Xu, Z.; Qiao, B.; Song, P.; Gao, D.; Xu, X. Shape-Controlled Synthesis of All-Inorganic CsPbBr₃ Perovskite Nanocrystals with Bright Blue Emission. *ACS Appl. Mater. Interfaces* **2016**, *8* (42), 28824–28830. <https://doi.org/10.1021/acsami.6b08528>.
- (140) Zhang, D.; Eaton, S. W.; Yu, Y.; Dou, L.; Yang, P. Solution-Phase Synthesis of Cesium Lead Halide Perovskite Nanowires. *Journal of the American Chemical Society* **2015**, *137* (29), 9230–9233. <https://doi.org/10.1021/jacs.5b05404>.
- (141) Liu, X.-D.; Wang, Q.; Cheng, Z.-Q.; Qiu, Y.-H.; Zhou, L.; Wang, Q.-Q. Solution-Phase Growth of Organolead Halide Perovskite Nanowires and Nanoplates Assisted by Long-Chain Alkylammonium and Solvent Polarity. *Materials Letters* **2017**, *206*, 75–79. <https://doi.org/10.1016/j.matlet.2017.06.113>.
- (142) Shamsi, J.; Urban, A. S.; Imran, M.; De Trizio, L.; Manna, L. Metal Halide Perovskite Nanocrystals: Synthesis, Post-Synthesis Modifications, and Their Optical Properties. *Chem. Rev.* **2019**, *119* (5), 3296–3348. <https://doi.org/10.1021/acs.chemrev.8b00644>.
- (143) Tong, Y.; Bladt, E.; Aygüler, M. F.; Manzi, A.; Milowska, K. Z.; Hintermayr, V. A.; Docampo, P.; Bals, S.; Urban, A. S.; Polavarapu, L.; Feldmann, J. Highly Luminescent Cesium Lead Halide Perovskite Nanocrystals with Tunable Composition and Thickness by Ultrasonication. *Angew. Chem. Int. Ed.* **2016**, *55* (44), 13887–13892. <https://doi.org/10.1002/anie.201605909>.
- (144) Jana, A.; Mittal, M.; Singla, A.; Sapra, S. Solvent-Free, Mechanochemical Syntheses of Bulk Trihalide Perovskites and Their Nanoparticles. *Chem. Commun.* **2017**, *53* (21), 3046–3049. <https://doi.org/10.1039/C7CC00666G>.
- (145) Lv, L.; Xu, Y.; Fang, H.; Luo, W.; Xu, F.; Liu, L.; Wang, B.; Zhang, X.; Yang, D.; Hu, W.; Dong, A. Generalized Colloidal Synthesis of High-Quality, Two-Dimensional Cesium Lead Halide Perovskite Nanosheets and Their Applications in Photodetectors. *Nanoscale* **2016**, *8* (28), 13589–13596. <https://doi.org/10.1039/C6NR03428D>.
- (146) Zhang, X.; Bai, X.; Wu, H.; Zhang, X.; Sun, C.; Zhang, Y.; Zhang, W.; Zheng, W.; Yu, W. W.; Rogach, A. L. Water-Assisted Size and Shape Control of CsPbBr₃ Perovskite Nanocrystals. *Angew. Chem. Int. Ed.* **2018**, *57* (13), 3337–3342. <https://doi.org/10.1002/anie.201710869>.
- (147) Li, Y.; Huang, H.; Xiong, Y.; Richter, A. F.; Kershaw, S. V.; Feldmann, J.; Rogach, A. L. Using Polar Alcohols for the Direct Synthesis of Cesium Lead Halide Perovskite Nanorods with Anisotropic Emission. *ACS Nano* **2019**, *13* (7), 8237–8245. <https://doi.org/10.1021/acs.nano.9b03508>.
- (148) Lou, S.; Xuan, T.; Liang, Q.; Huang, J.; Cao, L.; Yu, C.; Cao, M.; Xia, C.; Wang, J.; Zhang, D.; Li, H. Controllable and Facile Synthesis of CsPbBr₃-Cs₄PbBr₆ Perovskite Composites in Pure Polar Solvent. *Journal of Colloid and Interface Science* **2019**, *537*, 384–388. <https://doi.org/10.1016/j.jcis.2018.11.041>.
- (149) Hamill, J. C.; Romiluyi, O.; Thomas, S. A.; Cetola, J.; Schwartz, J.; Toney, M. F.; Clancy, P.; Loo, Y.-L. Sulfur-Donor Solvents Strongly Coordinate Pb²⁺ in Hybrid Organic–Inorganic Perovskite Precursor Solutions. *J. Phys. Chem. C* **2020**. <https://doi.org/10.1021/acs.jpcc.0c03465>.
- (150) Baranov, D.; Lynch, M. J.; Curtis, A. C.; Carollo, A. R.; Douglass, C. R.; Mateo-Tejada, A. M.; Jonas, D. M. Purification of Oleylamine for Materials Synthesis and Spectroscopic Diagnostics for *Trans* Isomers. *Chem. Mater.* **2019**, *31* (4), 1223–1230. <https://doi.org/10.1021/acs.chemmater.8b04198>.
- (151) Lu, C.; Wright, M. W.; Ma, X.; Li, H.; Itanze, D. S.; Carter, J. A.; Hewitt, C. A.; Donati, G. L.; Carroll, D. L.; Lundin, P. M.; Geyer, S. M. Cesium Oleate Precursor Preparation for Lead Halide Perovskite Nanocrystal Synthesis: The Influence of Excess Oleic Acid on Achieving Solubility, Conversion, and Reproducibility. *Chem. Mater.* **2019**, *31* (1), 62–67. <https://doi.org/10.1021/acs.chemmater.8b04876>.

- (152) De Roo, J.; Ibáñez, M.; Geiregat, P.; Nedelcu, G.; Walravens, W.; Maes, J.; Martins, J. C.; Van Driessche, I.; Kovalenko, M. V.; Hens, Z. Highly Dynamic Ligand Binding and Light Absorption Coefficient of Cesium Lead Bromide Perovskite Nanocrystals. *ACS Nano* **2016**, *10* (2), 2071–2081. <https://doi.org/10.1021/acsnano.5b06295>.
- (153) Stamplecoskie, K. G.; Manser, J. S.; Kamat, P. V. Dual Nature of the Excited State in Organic–Inorganic Lead Halide Perovskites. *Energy Environ. Sci.* **2014**, *8* (1), 208–215. <https://doi.org/10.1039/C4EE02988G>.
- (154) Guo, Y.; Shoyama, K.; Sato, W.; Matsuo, Y.; Inoue, K.; Harano, K.; Liu, C.; Tanaka, H.; Nakamura, E. Chemical Pathways Connecting Lead(II) Iodide and Perovskite via Polymeric Plumbate(II) Fiber. *J. Am. Chem. Soc.* **2015**, *137* (50), 15907–15914. <https://doi.org/10.1021/jacs.5b10599>.
- (155) Rahimnejad, S.; Kovalenko, A.; Forés, S. M.; Aranda, C.; Guerrero, A. Coordination Chemistry Dictates the Structural Defects in Lead Halide Perovskites. *ChemPhysChem* **2016**, *17* (18), 2795–2798. <https://doi.org/10.1002/cphc.201600575>.
- (156) Bohn, B. J.; Tong, Y.; Gramlich, M.; Lai, M. L.; Döblinger, M.; Wang, K.; Hoyer, R. L. Z.; Müller-Buschbaum, P.; Stranks, S. D.; Urban, A. S.; Polavarapu, L.; Feldmann, J. Boosting Tunable Blue Luminescence of Halide Perovskite Nanoplatelets through Postsynthetic Surface Trap Repair. *Nano Lett.* **2018**, *18* (8), 5231–5238. <https://doi.org/10.1021/acs.nanolett.8b02190>.
- (157) Holder, C. F.; Schaak, R. E. Tutorial on Powder X-Ray Diffraction for Characterizing Nanoscale Materials. *ACS Nano* **2019**, *13* (7), 7359–7365. <https://doi.org/10.1021/acsnano.9b05157>.
- (158) Fenton, J. L.; Steimle, B. C.; Schaak, R. E. Tunable Intraparticle Frameworks for Creating Complex Heterostructured Nanoparticle Libraries. **2018**, 6.
- (159) Schaak, R. E.; Steimle, B. C.; Fenton, J. L. Made-to-Order Heterostructured Nanoparticle Libraries. *Acc. Chem. Res.* **2020**, 11.
- (160) Yoon, S. J.; Stamplecoskie, K. G.; Kamat, P. V. How Lead Halide Complex Chemistry Dictates the Composition of Mixed Halide Perovskites. *J. Phys. Chem. Lett.* **2016**, *7* (7), 1368–1373. <https://doi.org/10.1021/acs.jpclett.6b00433>.
- (161) Stamplecoskie, K. G. Dual Nature of the Excited State in Organic–Inorganic Lead Halide Perovskites. *Environmental Science* **2015**, 8.
- (162) Stafford, B. *Top 7 Topics for Materials Science Research in 2020*. Materials Blog - Matmatch. <https://matmatch.com/blog/top-seven-topics-for-materials-science-research-in-2020/> (accessed 2021-10-19).
- (163) Wang, Y.-K.; Ma, D.; Yuan, F.; Singh, K.; Pina, J. M.; Johnston, A.; Dong, Y.; Zhou, C.; Chen, B.; Sun, B.; Ebe, H.; Fan, J.; Sun, M.-J.; Gao, Y.; Lu, Z.-H.; Voznyy, O.; Liao, L.-S.; Sargent, E. H. Chelating-Agent-Assisted Control of CsPbBr₃ Quantum Well Growth Enables Stable Blue Perovskite Emitters. *Nat Commun* **2020**, *11* (1), 3674. <https://doi.org/10.1038/s41467-020-17482-0>.
- (164) Zhang, L.; Lin, S. Dimensional Tailoring of Halide Perovskite: A Case Study on Cs₄PbBr₆/CsPbBr₃ Hybrid with Molecular Halide Perovskite. *Solar Energy Materials and Solar Cells* **2020**, *204*, 110237. <https://doi.org/10.1016/j.solmat.2019.110237>.
- (165) Chen, C.; Zhang, L.; Shi, T.; Liao, G.; Tang, Z. Controllable Synthesis of All Inorganic Lead Halide Perovskite Nanocrystals with Various Appearances in Multiligand Reaction System. *Nanomaterials* **2019**, *9* (12), 1751. <https://doi.org/10.3390/nano9121751>.
- (166) Kostopoulou, A.; Sygletou, M.; Brintakis, K.; Lappas, A.; Stratakis, E. Low-Temperature Benchtop-Synthesis of All-Inorganic Perovskite Nanowires. *Nanoscale* **2017**, *9* (46), 18202–18207. <https://doi.org/10.1039/C7NR06404G>.
- (167) Yang, D.; Li, X.; Li, Y.; Cai, B.; Su, L.; Zhang, S.; Juan, Z.; Meng, C.; Geng, D.; Chen, J.; Xu, F.; Zeng, H. Facet-Induced Coordination Competition for Highly Ordered CsPbBr₃ Nanoplatelets with Strong Polarized Emission. *Nano Res.* **2021**. <https://doi.org/10.1007/s12274-021-3509-6>.

- (168) Fanizza, E.; Cascella, F.; Altamura, D.; Giannini, C.; Panniello, A.; Triggiani, L.; Panzarea, F.; Depalo, N.; Grisorio, R.; Suranna, G. P.; Agostiano, A.; Curri, M. L.; Striccoli, M. Post-Synthesis Phase and Shape Evolution of CsPbBr₃ Colloidal Nanocrystals: The Role of Ligands. *Nano Res.* **2019**, *12* (5), 1155–1166. <https://doi.org/10.1007/s12274-019-2371-2>.
- (169) Gutmann, V. Empirical Parameters for Donor and Acceptor Properties of Solvents. *Electrochimica Acta* **1976**, *21* (9), 661–670. [https://doi.org/10.1016/0013-4686\(76\)85034-7](https://doi.org/10.1016/0013-4686(76)85034-7).
- (170) Liu, W.; Zheng, J.; Cao, S.; Wang, L.; Gao, F.; Chou, K.-C.; Hou, X.; Yang, W. General Strategy for Rapid Production of Low-Dimensional All-Inorganic CsPbBr₃ Perovskite Nanocrystals with Controlled Dimensionalities and Sizes. *Inorg. Chem.* **2018**, *57* (3), 1598–1603. <https://doi.org/10.1021/acs.inorgchem.7b02941>.
- (171) Chikan, V.; McLaurin, E. J. Rapid Nanoparticle Synthesis by Magnetic and Microwave Heating. *Nanomaterials* **2016**, *6* (5), 85. <https://doi.org/10.3390/nano6050085>.
- (172) Dover, M. V.; Hensley, W. A. Properties of 1-Octadecene, n-Octadecane, and Di-m-Tolylethane. *Ind. Eng. Chem.* **1935**, *27* (3), 337–339. <https://doi.org/10.1021/ie50303a023>.
- (173) Wang, Y.; Ding, G.; Mao, J.-Y.; Zhou, Y.; Han, S.-T. Recent Advances in Synthesis and Application of Perovskite Quantum Dot Based Composites for Photonics, Electronics and Sensors. *Science and Technology of Advanced Materials* **2020**, *21* (1), 278–302. <https://doi.org/10.1080/14686996.2020.1752115>.
- (174) Ou, Q.; Bao, X.; Zhang, Y.; Shao, H.; Xing, G.; Li, X.; Shao, L.; Bao, Q. Band Structure Engineering in Metal Halide Perovskite Nanostructures for Optoelectronic Applications. *Nano Materials Science* **2019**, *1* (4), 268–287. <https://doi.org/10.1016/j.nanoms.2019.10.004>.
- (175) Chang, X.; Fang, J.; Fan, Y.; Luo, T.; Su, H.; Zhang, Y.; Lu, J.; Tsetseris, L.; Anthopoulos, T. D.; Liu, S. (Frank); Zhao, K. Printable CsPbI₃ Perovskite Solar Cells with PCE of 19% via an Additive Strategy. *Advanced Materials* **2020**, *32* (40), 2001243. <https://doi.org/10.1002/adma.202001243>.
- (176) Cai, B.; Yang, X.; Yu, Z.; Liang, Y.; Shan, Y.; Hagfeldt, A.; Sun, L. Unveiling the Light Soaking Effects of the CsPbI₃ Perovskite Solar Cells. *Journal of Power Sources* **2020**, *472*, 228506. <https://doi.org/10.1016/j.jpowsour.2020.228506>.
- (177) Chen, Z.; Dong, L.; Tang, H.; Yu, Y.; Ye, L.; Zang, J. Direct Synthesis of Cubic Phase CsPbI₃ Nanowires. *CrystEngComm* **2019**, *21* (9), 1389–1396. <https://doi.org/10.1039/C8CE02111B>.
- (178) Dastidar, S.; Hawley, C. J.; Dillon, A. D.; Gutierrez-Perez, A. D.; Spanier, J. E.; Fafarman, A. T. Quantitative Phase-Change Thermodynamics and Metastability of Perovskite-Phase Cesium Lead Iodide. *J. Phys. Chem. Lett.* **2017**, *8* (6), 1278–1282. <https://doi.org/10.1021/acs.jpcllett.7b00134>.
- (179) Creutz, S. E.; Crites, E. N.; De Siena, M. C.; Gamelin, D. R. Anion Exchange in Cesium Lead Halide Perovskite Nanocrystals and Thin Films Using Trimethylsilyl Halide Reagents. *Chem. Mater.* **2018**, *30* (15), 4887–4891. <https://doi.org/10.1021/acs.chemmater.8b02100>.
- (180) De Roo, J.; Ibáñez, M.; Geiregat, P.; Nedelcu, G.; Walravens, W.; Maes, J.; Martins, J. C.; Van Driessche, I.; Kovalenko, M. V.; Hens, Z. Highly Dynamic Ligand Binding and Light Absorption Coefficient of Cesium Lead Bromide Perovskite Nanocrystals. *ACS Nano* **2016**, *10* (2), 2071–2081. <https://doi.org/10.1021/acs.nano.5b06295>.
- (181) Ravi, V. K.; Swarnkar, A.; Chakraborty, R.; Nag, A. Excellent Green but Less Impressive Blue Luminescence from CsPbBr₃ perovskite Nanocubes and Nanoplatelets. *Nanotechnology* **2016**, *27* (32), 325708. <https://doi.org/10.1088/0957-4484/27/32/325708>.
- (182) Li, Z.; Park, J.-S.; Walsh, A. Evolutionary Exploration of Polytypism in Lead Halide Perovskites. *Chem. Sci.* **2021**, *12* (36), 12165–12173. <https://doi.org/10.1039/D1SC03098A>.

- (183) Pellet, N.; Teuscher, J.; Maier, J.; Grätzel, M. Transforming Hybrid Organic Inorganic Perovskites by Rapid Halide Exchange. *Chem. Mater.* **2015**, 27 (6), 2181–2188. <https://doi.org/10.1021/acs.chemmater.5b00281>.
- (184) Zhihai, W.; Jiao, W.; Yanni, S.; Jun, W.; Yafei, H.; Pan, W.; Nengping, W.; Zhenfu, Z. Air-Stable All-Inorganic Perovskite Quantum Dot Inks for Multicolor Patterns and White LEDs. *J Mater Sci* **2019**, 54 (9), 6917–6929. <https://doi.org/10.1007/s10853-019-03382-2>.
- (185) Zhao, S.; Qin, M.; Xiang, Y.; Wang, H.; Xie, J.; Gong, L.; Chen, J.; Lu, X.; Song, J.; Qu, J.; Xu, J.; Yan, K. Bifunctional Effects of Trichloro(Octyl)Silane Modification on the Performance and Stability of a Perovskite Solar Cell via Microscopic Characterization Techniques. *ACS Appl. Energy Mater.* **2020**, 3 (4), 3302–3309. <https://doi.org/10.1021/acsaem.9b02306>.
- (186) Kim, J. Y.; Kim, B. G.; Kim, M.; Jang, W.; Wang, D. H. One-Step Formation of Core/Shell Structure Based on Hydrophobic Silane Ligands for Enhanced Luminescent Perovskite Quantum Dots. *Journal of Alloys and Compounds* **2021**, 886, 161347. <https://doi.org/10.1016/j.jallcom.2021.161347>.
- (187) Liu, Y.; Tang, S.; Fan, J.; Gracia-Espino, E.; Yang, J.; Liu, X.; Kera, S.; Fahlman, M.; Larsen, C.; Wågberg, T.; Edman, L.; Wang, J. Highly Soluble CsPbBr₃ Perovskite Quantum Dots for Solution-Processed Light-Emission Devices. *ACS Appl. Nano Mater.* **2021**, 4 (2), 1162–1174. <https://doi.org/10.1021/acsanm.0c02797>.
- (188) Samu, G. F.; Scheidt, R. A.; Kamat, P. V.; Janáky, C. Electrochemistry and Spectroelectrochemistry of Lead Halide Perovskite Films: Materials Science Aspects and Boundary Conditions. *Chem. Mater.* **2018**, 30 (3), 561–569. <https://doi.org/10.1021/acs.chemmater.7b04321>.
- (189) Gritzner, G.; Kuta, J. RECOMMENDATIONS ON REPORTING ELECTRODE POTENTIALS IN NONAQUEOUS SOLVENTS. 6.
- (190) Bai, L.; Wang, S.; Zhang, Y.; Zhang, K.; Li, H.; Ou, K.; Yi, L. Investigation on Violet/Blue All-Inorganic Light-Emitting Diodes Based on CsPbCl₃ Films. *Journal of Luminescence* **2020**, 226, 117422. <https://doi.org/10.1016/j.jlumin.2020.117422>.

Chapter 7 – Curriculum Vitae

Hediyeh Zamani

hzamani@syr.edu | 607-379-7246 | 10 Harbor point, Dorchester, MA

www.linkedin.com/in/hediyehzamani

EDUCATION

DOCTOR OF PHILOSOPHY Syracuse University | Syracuse, NY **MAY 2023**

Major: Chemistry | G.P.A: 3.98

BACHELOR OF SCIENCE Sharif University of Technology | Tehran, Iran **MAY 2013**

Major: Chemistry

LABORATORY SKILLS

Semiconductor Nanomaterials Synthesis: Hot-Injection using Schlenk line and High-throughput Microwave synthesizer, Colloidal Stabilization Techniques, Catalytic Reactor Design, UV-VIS Spectroscopy, Fluorescence Spectroscopy, FTIR Spectroscopy, Scanning Electron Microscopy (SEM), Atomic Force Microscopy (AFM), X-Ray Diffraction (XRD) Crystallography, Dynamic Light Scattering (DLS), Thermogravimetric Analysis (TGA), Potentiostat (Cyclic Voltammetry), Computer Skills: MS Office, Origin, ImageJ, Chemdraw

TEACHING SKILLS

Skilled in online teaching tools including Zoom, Google Docs/Sheets/Slides, Kahoot, college teaching platforms like Blackboard and Turnitin for test design, content creation, communication, etc. Skilled in pedagogical techniques to engage students and improve both students' and teachers' performance via frequent two-way evaluation.

RESEARCH EXPERIENCE

SCIENTIST

Metalmark Innovations – Research & Development | Boston, MA **JAN 2022 – PRESENT**

- Designed and assembled high-throughput catalytic reactors and multi-purpose test setup for Volatile Organic Compounds (VOC) adsorption and oxidation
- Identified & characterized emission products and byproducts of VOC catalysis by Pt@Al₂O₃ using gas-FTIR and VOC sensors
- Evaluated & identified best mixed metal oxide catalysts using light-off curve and emission profile in oxidizing VOCs
- Evaluated & identified best VOC adsorbents using capacity and regeneration capability

- Evaluated commercial & prototype air-purifiers in system performance and capacity in removing particulate matters and VOCs

RESEARCH ASSISTANT

JAN 2018 – DEC 2021

Syracuse University – Chemistry Department | Syracuse, NY

- Designed & performed high-temperature air-sensitive reactions using Schlenk line & high-throughput microwave irradiation synthesis with experience in glovebox
- Synthesized 0D & 2D perovskite nanoparticles tailored by solvent and microwave effect
- Characterized 0D and 2D nanoparticles using UV-Vis and fluorescence spectroscopy, XRD, AFM, potentiostat, FTIR, TEM and ¹H-NMR and analyzed the data
- Performed pre/post-synthesis growth mechanism studies & halide exchange reactions in CsPbBr₃ colloidal systems and films
- Ran TGA, AFM and microwave synthesis for collaborators & recorded instrument activity
- Wrote yearly reports & a paper & presented the research in meetings & conferences
- Supervised, trained, and mentored undergraduate students

RESEARCH ASSISTANT

MAY 2016 – MAY 2017

Cornell University – Food Science Department | Ithaca, NY

- Studied several polysaccharides to improve colloidal stability of whey protein for applications in energy drinks
- Identified soybean soluble polysaccharide as the best ligand for colloidal stability of whey protein in pasteurized and acidic products
- Wrote company reports and a first-author paper in the Journal of Food Science
- Ran UV-Vis & fluorescence spectroscopy, DLS & laser diffraction (Size & zeta-potential)

PUBLICATIONS

- Busto, G., Wineh, R., Zamani, H., Shirman, E., ... & Shirman, T. (2022) "Raspberry colloid templated catalysts fabricated using spray drying method" *Catalysts*, 13(1), 60.
- Zamani, H., Chiang, T. H., Klotz, K., Hsu, A., Maye, M. M. (2022) "Tailoring CsPbBr₃ Growth Via Non-Polar Solvent Choice and Heating Methods" *Langmuir*, 38, 30, 9363–9371.
- Zamani, H., Zamani, S., Zhang, Z., & Abbaspourrad, A. (2020). "Exceptional colloidal stability of acidified whey protein beverages stabilized by soybean soluble polysaccharide" *Journal of food science*, 85(4), 989-997.

- Davis, A. H., Hofman, E., Chen, K., Li, Z. J., Khammang, A., Zamani, H., ... & Zheng, W. (2019). "Exciton energy shifts and tunable dopant emission in manganese-doped two-dimensional CdS/ZnS core/shell nanoplatelets" *Chemistry of Materials*, 31(7), 2516-2523.
- Selig, M. J., Mehrad, B., Zamani, H., Kierulf, A., Licker, J., & Abbaspourrad, A. (2018). "Distribution of oil solubilized β -carotene in stabilized locust bean gum powders for the delivery of orange colorant to food products" *Food Hydrocolloids*, 84, 34-37.
- Zamani, H., Maye, M. M. (2021, Feb.) "Fast and safe microwave-assisted synthesis of perovskite semiconductor nanoparticles" [Poster Presentation] 2021 AAAS Annual Meeting
- Zamani, H., Maye, M. M. (2020, Aug.) "Microwave assisted synthesis of cesium lead halide nanoplatelets" [Oral Pitch] Virtual American Chemical Society national meeting and expo
- Zamani, H., Maye, M. M. (2020, Aug.) "Microwave assisted synthesis of cesium lead halide nanoplatelets" [Poster Presentation] Virtual American Chemical Society national meeting and expo
- Zamani, H., Maye, M. M. (2019, May) "Microwave and solvent effects in the preparation of all inorganic CsPbX_3 nanoplatelets" [Poster Presentation] NERM (NorthEastern of ACS)

Teaching Experience

GRADUATE TEACHING ASSISTANT | AUG 2018 – DEC 2020

Syracuse University - College of Arts and Sciences | Syracuse, NY

General Chemistry Lab I (Honors & Majors) – Three fall semesters

General Chemistry Lecture II (Honors & Majors) – Spring semester 2019

Forensic Chemical Analysis Lab (1 Undergrad & 1 Grad level) – Spring semester 2020

- Designed and taught lab sessions,
- Led students in performing a safe and informative experiment
- Evaluated and monitored students' progress
- Designed pre-lab and post-lab questions using Blackboard and Turnitin platforms
- Trained a Teaching Assistant for the Gen Chem lab
- Improved students experience using pedagogical methods, high-level analytical instruments such as XRD and TGA were introduced and thought to freshmen.

COURSE FACILITATOR | OCT 2019 & OCT 2020

Syracuse University - University College | Syracuse, NY

First Year Experience – SEM 100

- Taught a class of eighteen freshman students as a lead facilitator with discussions around multiculturalism, inclusion and self-identity at Syracuse University with the collaboration of an undergraduate cofacilitator.
- Used ice-breakers, videos, and several discussion techniques.
- In the course evaluation, 93% of the students said they were encouraged to participate in conversations and activities in an atmosphere of trust and respect.

Pre-PhD Teaching Experience

TEACHING ASSISTANT | JUNE 2012 TO MAY 2013

KANOON FARHANGI AMOOZESH | TEHRAN, IRAN

Conducted recitation math, physics and chemistry classes to prepare high school students for the Iranian college-entry exam, monitored and filed students' progress, gave exams

TEACHING ASSISTANT | JANUARY 2012 TO JUNE 2012

SHARIF UNIVERSITY OF TECHNOLOGY | TEHRAN, IRAN

Instructed undergraduate students on how to perform experiments efficiently and safely in the Inorganic Chemistry I laboratory as a junior student assisting a grad student.

LEADERSHIP & VOLUNTEER WORK

ORGANIZING COMMITTEE OF ComSciCon-NY 2021 WORKSHOP OCT 2019 - JUN 2021

Cornell University | Whova/Zoom -(ComSciCon-NY 2020 was canceled due to Covid19)

- Designed four panels and three workshops, Invited speakers, Secured funds and logistics including the Whova online platform, Moderated the writing/storytelling panel, Led the workshops: scientific writing and podcast for public audience

VICE-PRESIDENT OF ISA (IRANIAN STUDENT ASSOCIATION) AUG 2018 - AUG 2019

Syracuse University | Syracuse, NY

- Cofounder of ISA, Held four cultural programs for 50-100 people